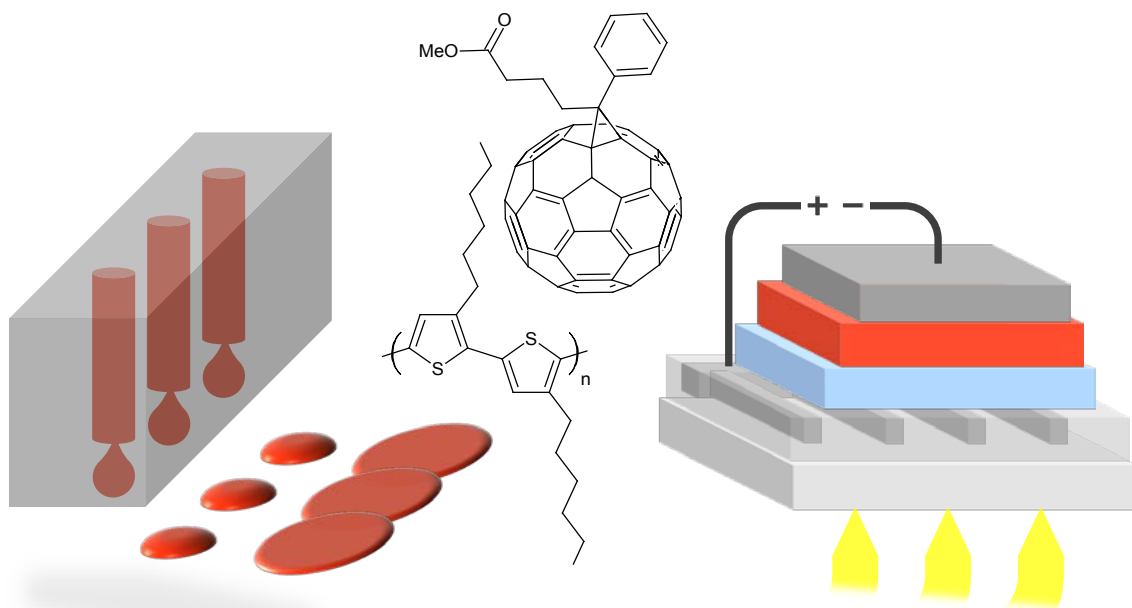# Towards Industrial Viability of Organic Solar Cells:

ITO-free, Green Solvents and Technological Aspects for Upscalability

Ignasi Burgués Ceballos

PhD Thesis

UAB

Universitat Autònoma de Barcelona

Towards Industrial Viability of Organic Solar Cells:
ITO-free, Green Solvents and
Technological Aspects for Upscalability

Ignasi Burgués Ceballos
PhD Thesis

PhD in Chemistry

Supervisors: Dr. Mariano Campoy Quiles and Dr. Paul Lacharmoise

Tutor: Dr. José Antonio Ayllón Esteve

Department of Chemistry

Faculty of Science

2014

Memòria presentada per aspirar al Grau de Doctor per

Ignasi Burgués Ceballos

Vist i plau:

Dr. Mariano Campoy Quiles   **Dr. Paul Lacharmoise**   **Dr. José Antonio Ayllón Esteve**

Co-director   Co-director   Tutor

Bellaterra, 28 d'Abril de 2014

Als meus pares, a l'Anna i a la Marina

"We all want to help one another. Human beings are like that. We want to live by each other's happiness – not by each other's misery. We don't want to hate and despise one another. In this world there is room for everyone. And the good earth is rich and can provide for everyone.

[...] You, the people have the power – the power to create machines. The power to create happiness! You, the people, have the power to make this life free and beautiful, to make this life a wonderful adventure.

Then – in the name of democracy – let us use that power – let us all unite. Let us fight for a new world – a decent world that will give men a chance to work – that will give youth a future and old age a security.

[...]Let us fight for a world of reason, a world where science and progress will lead to all men's happiness"

Charles Chaplin
The Great Dictator (1940)

ABSTRACT

Since its emergence as an alternative for photovoltaic energy conversion, the field of organic solar cells has experienced significant progress, especially in the last 15 years. The high interest in organic photovoltaics (OPV) technology is mostly due to its low-cost potential. Relevant scientific advances have pushed power conversion efficiencies up to 12%, which is encouraging for bringing OPV to market. However, other decisive aspects for their industrialisation have been less attended.

This thesis deals with three key issues that OPV technology has to face in order to achieve a reliable lab-to-fab transfer. First, approaches for large-scale processing and post-processing are needed, ideally with reduced cost. In this work a broad investigation in inkjet printing is presented. A deep understanding on this roll-to-roll compatible technique is necessary to achieve suitable layer morphology. The drying kinetics of the wet film has been found to be especially critical. In relation to this, a new method to determine appropriate printing patterns for active layer deposition has been developed. Moreover, an alternative post-processing treatment called vapour printing is demonstrated for OPV devices. Using this method with suitable solvent vapour, the annealing of the active layer can be achieved in much shorter times as compared to other treatments.

Another aspect that has been poorly attended is related to the solvents used for OPV processing, specifically for active layer deposition. Typically halogenated solvents such as chlorobenzene or o-dichlorobenzene are employed, being some of them banned for industrial applications. Their replacement by green formulations is therefore a major need. In order to find suitable green solvent systems, a method based on solubility has been used. This method, previously demonstrated for polymeric solar cells, is successfully extended in this thesis for small molecule based devices. New insights into the accuracy of the method are also provided.

A major contributor to the cost of an OPV module is the indium-tin-oxide (ITO), commonly used as a transparent conductive electrode. Further reasons to replace this component include its modest flexibility and conductivity, which may limit current extraction in large area devices. One possible alternative are metallic grids combined with a transparent semiconductor layer. Although the conductivity issue is solved, other factors still limit current extraction. The new method used in this work to

prepare such structures overcomes these features. Efficient, ITO-free devices are demonstrated.

RESUM

Des de la seva aparició com a alternativa per la conversió d'energia fotovoltaica, el camp de les cel·les solars orgàniques ha experimentat un progrés significatiu, especialment en els darrers 15 anys. El gran interès en la tecnologia fotovoltaica orgànica (OPV, per les sigles en anglès) es deu principalment al seu potencial baix cost. Rellevants avenços científics han empès les eficiències de conversió energètica fins al 12%, fet que encoratja a acostar les OPV al mercat. Tanmateix, altres aspectes decisius per la seva industrialització han estat menys atesos.

Aquesta tesi tracta tres qüestions clau que la tecnologia OPV ha d'afrontar per tal d'assolir una transferència fiable del laboratori a la industria. En primer lloc, es necessiten estratègies pel processat i post-processat a gran escala, idealment amb un cost reduït. En aquest treball es presenta una amplia investigació en *inkjet printing*. És necessari tenir un profund coneixement d'aquesta tècnica compatible amb *roll-to-roll* per tal d'assolir morfologies de capa adequades. S'ha trobat que la cinètica d'assecat de les capes és especialment crítica. En relació a això, s'ha desenvolupat un nou mètode per determinar patrons d'impressió apropiats per la deposició de la capa activa. A més, s'ha demostrat l'ús d'un tractament alternatiu anomenat *vapour printing* en dispositius OPV. Utilitzant aquest mètode amb vapor de dissolvent adequat, el tractament de la capa activa es pot assolir en temps molt més curts en comparació a altres tècniques.

Un altre aspecte que ha estat poc atès està relacionat amb els dissolvents utilitzats pel processat dels OPV, especialment per la deposició de la capa activa. Típicament s'utilitzen dissolvents halogenats, com el clorbenzè o el diclorbenzè, essent alguns d'ells prohibits per aplicacions industrials. Substituir-los per formulacions verdes és, per tant, una necessitat primordial. Per tal de trobar sistemes aptes de dissolvents verds, s'ha utilitzat un mètode basat en la solubilitat. Aquest mètode, prèviament demostrat per cel·les solars polimèriques, s'estén de manera satisfactòria en aquesta tesi en dispositius basats en petita molècula. També s'aporten nous coneixements sobre la precisió del mètode.

L'oxid d'indi i estany (ITO, per les seves sigles en anglès), freqüentment utilitzat com a elèctrode conductor transparent, contribueix de manera important en el cost d'un

mòdul OPV. Altres raons per reemplaçar aquest component inclouen la seva modesta flexibilitat i conductivitat, el que pot limitar l'extracció de corrent elèctric en dispositius de gran àrea. Una possible alternativa són les xarxes metàl·liques combinades amb una capa transparent semiconductora. Tot i resoldre l'aspecte de la conductivitat, altres factors limiten encara l'extracció de corrent. El nou mètode utilitzat en aquest treball per preparar aquestes estructures venç aquests factors. Es demostren dispositius eficients lliures de ITO.

RESUMEN

Desde su aparición como alternativa para la conversión de energía fotovoltaica, el campo de las células solares orgánicas ha experimentado un progreso significativo, especialmente en los últimos 15 años. El gran interés en la tecnología fotovoltaica orgánica (OPV, por sus siglas en inglés) se debe principalmente a su potencial bajo coste. Relevantes avances científicos han empujado las eficiencias de conversión energética hasta el 12%, lo que alienta el acercamiento de las OPV al mercado. Sin embargo, otros aspectos decisivos para su industrialización han sido menos atendidos.

Esta tesis trata tres cuestiones clave que la tecnología OPV tiene que afrontar para alcanzar una transferencia fiable del laboratorio a la industria. En primer lugar, se necesitan estrategias para el procesado y post-procesado a gran escala, idealmente con un coste reducido. En este trabajo se presenta una amplia investigación en *inkjet printing*. Es necesario tener un profundo conocimiento sobre esta técnica compatible con *roll-to-roll* para obtener morfologías de capa adecuadas. Se ha encontrado que la cinética de secado de la capa es especialmente crítica. En relación a esto, se ha desarrollado un nuevo método para determinar patrones de impresión adecuados para la deposición de la capa activa. Además, se ha demostrado el uso de un tratamiento alternativo llamado *vapour printing* en dispositivos OPV. Utilizando este método con vapores de disolvente aptos, el tratamiento de la capa activa se puede alcanzar en tiempos mucho más cortos en comparación con otras técnicas.

Otro aspecto que ha sido poco atendido está relacionado con los disolventes utilizados en el procesado de las OPV, especialmente en la deposición de la capa activa. Típicamente se emplean disolventes halogenados, como el clorobenceno o diclorobenzeno, estando alguno de ellos prohibidos en aplicaciones industriales. Su substitución por formulaciones verdes es, por tanto, una necesidad primordial. Para encontrar sistemas aptos de disolventes verdes, se ha utilizado un método basado en la

solubilidad. Este método, previamente demostrado para células solares poliméricas, se extiende de manera exitosa en esta tesis para dispositivos basados en pequeña molécula. También se aportan nuevos conocimientos sobre la precisión del método.

El óxido de indio y estaño (ITO, por sus siglas en inglés), frecuentemente utilizado como electrodo conductor transparente, contribuye de manera importante en el coste de un módulo OPV. Otros motivos para substituir este componente incluyen su modesta flexibilidad y conductividad, lo que puede limitar la extracción de corriente eléctrica en dispositivos de gran área. Una posible alternativa son las redes metálicas combinadas con una capa transparente semiconductora. A pesar de que el aspecto de la conductividad queda solucionado, otros factores limitan aún la extracción de corriente. El nuevo método utilizado en este trabajo para preparar estas estructuras vence estos aspectos. Se demuestran dispositivos eficientes libres de ITO.

ACKNOWLEDGEMENTS

Fent balanç global del què m'ha aportat aquesta tesi, només em venen coses bones al cap. Em sento molt afortunat d'haver compartit aquest temps amb tanta bona gent i d'haver après tant i tant. I és gràcies a vosaltres que ara sóc aquí, a les portes d'acabar una etapa molt bonica, durament treballada i amb tots els ingredients que es poden demanar per créixer com a persona. I com que "es de buen nacido ser agradecido", allá que vamos.

Alguien me decía que no era muy buen asunto eso de tener dos directores de tesis. Pues nada más lejos de la realidad. He tenido la inmensa suerte de contar con el total apoyo, confianza y paciencia de dos personas a las que admiro y de las que he aprendido muchísimo. Paul y Mariano, un millón de gracias! Por apostar por mí, por vuestra gran implicación y esfuerzo en esta tesis, por la pasión que pusisteis en el proyecto, por las largas discusiones de resultados, por poner dosis de realismo cuando el optimismo infinito me cegaba, por animarme en los momentos chungos. Y todo esto siempre con el buen rollo por delante! Quiero agradeceros, de todo corazón, todo lo que me habéis dado. Ya no sólo a nivel científico (que no es poco!) sino a todos los niveles. Todo lo que pueda poner aquí se va a quedar corto. Sois un referente para mí. Gracias!!!

De l'ICMAB vull donar les gràcies a tothom, especialment al grup de Nanostructured Optoelectronic Materials. Als que estan i als que van passar: Isabel, Miquel, Ale, Pablo, Christian, Bernhard, Malte, Mahdieh, Lucas, Carmen, Joanna, Xavi, Xabo, Damià, Ferran i José Luis. También aprendí un montón de vosotros. Gracias a todos por el tiempo que compartimos! I gràcies també als companys de despatx!

A Cetemmsa també m'hi he sentit molt a gust i vull agrair-vos també tot el suport que m'heu donat. Del laboratori m'enduc molts records i algun any de vida menys per inhalació de chlorobenzè. Mil gràcies a en Marco, Eugenia, Laia F, Núria, Laia V, Carme, Oscar, Cristina, Xavis, Irene, Maria, Laurent, Alberto i Edu. Ànims i endavant!

I would like to thank Professor Christoph J. Brabec for giving me the opportunity to spend some time in his group. I keep very good memories from my stay at Erlangen. Special thanks to Tayebeh Ameri and Monika Voigt for their supervision and to Florian Machui for his valuable help. Thanks a lot to Luca, Derya and George for all

the nice moments we shared, it was great! And also special thanks to my friend Martin. Vielen Dank!

Aquesta tesi tampoc hauria estat possible sense el suport incondicional de la família i els amics. Aquesta tesi també és vostra. Infinites gràcies, papà, mamá, Anna, Marina i Yago. També especialment a en Pere, Nitu, Jordi, Isa, Gerard i Imma. Gràcies a tots per estimar-me. Jo també us estimo!!!

A totes i tots, GRÀCIES

...i Glòria a les Santes!!!

MOTIVATION AND STRUCTURE OF THE THESIS

Nowadays the negative impact of human activity on climate change is undeniable. Moreover, considering that fossil resources availability is decreasing while human population keeps rising, a secure, sustainable and fair distribution of energy is a huge challenge. Renewable energies have the key for this necessary change of model.

Organic photovoltaics (OPV) are a promising technology with a high potential and have attracted a lot of scientific and industrial interest. Further research is still needed, however, to address three main objectives: high efficiency, long stability and low cost. Reported alternatives for the processing and post-processing of OPV are often applicable only to specific material systems. Other issues such as sustainability of OPV processing are important as well. The aim of this thesis is to provide solutions to assist an easier transfer from lab to large-scale production. The approaches herein presented are intended to the broadest possible range of materials.

The thesis is structured in five chapters as follows:

A comprehensive description of the fundamentals of organic solar cells is given in Chapter 1. Besides the working principles and basic definitions, a summarised state of the art is provided, especially focused in the progress made in active layer materials. The experimental methods and materials used for the development of this work are exposed in Chapter 2.

Chapter 3 shows the results obtained through the complete optimisation process of solar cell devices prepared by inkjet printing. Particularly detailed are the parameters that affect the drying kinetics of the active layer, which in turn determine the film morphology. This processing technique is compared to doctor blade and spin coating. Optimisation of OPV fabrication includes choosing adequate processing methods for layer deposition and studying the suitability of buffer layers. Finally, the use of vapour printing as a fast post-processing treatment for the active layer is demonstrated.

The use of alternative, green formulations for active layer processing is extensively discussed in Chapter 4. The Hansen solubility parameters analysis is presented and used to determine suitable non-toxic solvents for small molecules. To validate the method, OPV devices are fabricated using the proposed green formulations and

compared to reference devices processed from halogenated solvents. The method is later adapted to low band gap polymers.

The fabrication of ITO-free devices based on current collecting Ag grids is described in Chapter 5. The whole process of optimisation is therein presented. The adapted model used to determine suitable grid geometries is discussed. Also, the preparation of the grid structures using different techniques is shown, including the method to embed the grids within the substrate. Finally, the performance of OPV devices using different anode structures and geometries is discussed.

Despite belonging to the same topic and sharing transversal issues such as the use of inkjet printing, the results presented in chapters 3, 4 and 5 refer to quite different aspects of OPV technology. In order to assist an easier reading of the thesis, the conclusions are given at the end of each chapter.

CONTENTS

CHAPTER 1

Introduction

Abstract

Our current energy system, based on fossil fuels, is highly unsustainable, insecure, unfair and pollutant. The challenge of our generation is to move towards a cleaner and sustainable energy model. The change of paradigm is urgent. And it is possible. We only need to believe it and act. Renewable energies will hopefully bring us to a new scenario, where clean energy will be securely accessible for everybody. It is our responsibility, even more as scientists, to seek solutions to achieve sustainable development.

Fortunately, our environment is surrounded by abundant solar energy. Among the different alternatives to convert this into electrical power, photovoltaics represent the most direct way. The development of photovoltaic technology has been intense, addressing key issues such as efficiency and cost. This thesis focuses in one particular, emerging photovoltaic technology: organic solar cells. A detailed review of the fundamentals of this technology is given in this chapter in order to assist an easy reading of this thesis.

1.1. THE NEED FOR ALTERNATIVE, GREEN ENERGY RESOURCES

Energy is a basic need for the development of any society. It is undeniable that the great progress experienced by (sadly, only) some countries since the 19th century has been strongly linked to advances in energy conversion. So far fossil fuels (coal, oil and gas) have been the main energy resource. Now we know enough about the severe problematic issues that our energy system comprises. We need alternatives.

1.1.1. Dark and dirty scenario (or where we are)

Currently, fossil fuels still represent a large proportion of global energy supply. Two main (big) troubles are related to these energy sources. First, they are finite; our rate of fossil extraction and consumption is extremely faster than that of new fossil generation in the Earth. As a result, we will soon (or already did) reach peak oil,[1] the maximum rate of oil extraction. Moreover, the forecasts in human population growth and the irruption of the so-called emerging countries predict a significant increase in energy demand in the next years.[2] This leads to an implacable, progressive rising of oil price. The unbalanced distribution of these resources across the Earth accentuates the problem of limited availability. This is the main cause of geopolitical conflicts around the world.

Secondly, the burning of fossil fuels has a strong, negative impact in climate, as greenhouse gases are emitted, mostly CO_2. Increasing the concentration of these gases in the atmosphere leads to global warming and subsequent climate change. An increase of 2-3 ºC in the Earth's surface would carry dramatic effects.[3] And evidence should not be dismissed: recent data confirm that the majority of global anthropogenic greenhouse gas emissions are derived from fossil fuel consumption.[4]

Under this perspective, development seems to be strongly correlated to increasing energy consumption and growth of gas emissions, with limited availability of resources. Renewable energies may break this correlation, as they can address a sustainable development based on endless and clean resources.

1.1.2. Bright and clean scenario (or where we should go)

Renewable energies (RE) provide us a unique opportunity to rethink our energy model. Huge reduction in gas emissions can be achieved by properly implementing RE technologies. Human impact on environment can be substantially mitigated. The

limitation of availability is also eliminated, as resources are naturally recovered in a human timescale. Furthermore, these resources are extendedly distributed in a more or less equitable manner. Consequently, a secure access to energy is affordable by almost any country, eventually being self-supplying. In a complete distributed energy net, even single persons could act as producers-consumers. This is a definite change in energy paradigm.[5]

This chapter started with the sentence "Energy is a basic need for the development of any society". Now we can go one step further by saying "Renewable energies are fundamental for the sustainable development of any society".

Fortunately, some countries have modified their energy policies to move towards RE with determination. Although this is only the beginning and further efforts are needed, recent results are encouraging. For example, in Spain, wind was the primary energy source of electricity (20.8%) in 2013 for the first time in history. To put it into context, in 2000 the contribution of wind energy corresponded only to the 2.3% of total production.[6] Hopefully these facts will someday convince the sceptics in RE. Indeed the energy mix in the cited country is in clear transition towards a more sustainable model.[7]

Solar energy is the primary energetic source available anywhere on Earth. The annual incoming irradiance from the sun is about 10,000 times greater than our global primary energy demand.[4] Almost all energy supplies are directly or indirectly related to the sun. For instance, wind is a result of Earth's rotation and solar-heated air. Biomass (and even fossils in their day) is created through photosynthesis. Even so, photovoltaics (PV) provide the fastest and most direct conversion of sunlight into electrical power.

However, the still high cost of PV technology is inhibiting it for becoming a primary energy source. Efficient photo-conversion at low cost is a major challenge. Many different approaches have been proposed. Among these, organic solar cells, the focus of the present thesis, offer a promising alternative. The solution processability of potentially low-cost, semiconducting materials that are synthesised is the primary argument for OPV. Continuous roll-to-roll deposition methods can be used to fabricate flexible modules.

1.2. ORGANIC SOLAR CELLS. FUNDAMENTALS

1.2.1. Solar spectrum

Sunlight is composed of a wide range of wavelengths within the electromagnetic spectrum, including ultraviolet, visible and infrared radiation, being the maximum in the visible range (see **Figure 1.1**). After passing through the atmosphere, the shape of the spectrum reaching the Earth's surface is modified and its intensity is attenuated. These changes are due to light filtration and scattering produced by atmospheric molecular components.

As seen in Figure 1.1, a large part of total solar irradiance (almost 70%) is located in the range between 300 nm and 900 nm, which correspond to photon energies of 4.13 eV and 1.38 eV, respectively.
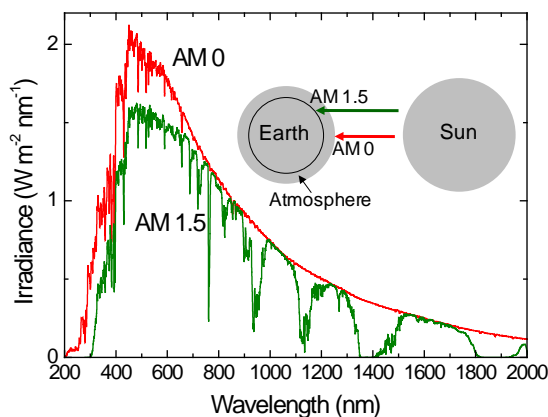
Figure 1.1. Extra-terrestrial (Air Mass 0, red line) and standard terrestrial (Air Mass 1.5, green line) solar spectra. AM 1.5 correspond to a zenith angle of 42º, i.e. at northern latitudes of Europe, as indicated in inset scheme.

The standard terrestrial solar spectrum is defined as the AM 1.5 spectrum with an integrated irradiance of 1000 W·m^{-2}. These conditions are reproduced by solar simulators in order to characterise solar cell devices under the accepted standard.

For effective light harvesting, solar cell materials should show strong light absorption, ideally with the highest possible overlapping with AM 1.5 solar spectrum. This and other important material properties are described in the following two sections.

1.2.2. Third generation photovoltaics

Solar cells can be classified in three categories, depending on the materials and architectures they use. First generation solar cells include large-scale, single-junction devices, usually based on crystalline silicon. The 90% of current photovoltaic production is based on this type of solar cells.[8] Their theoretical limit stands at 30% (the Shockley-Queisser limit),[9] while 25% efficiency has been reported. The high cost of material (silicon wafers) and production is a constraint for this type of devices.

Precisely, the aim of second generation solar cells is to reduce the high cost of their predecessors without losing efficiency. Primarily this has been addressed by reducing the amount of semiconducting materials, resulting in thin-film based devices. Amorphous silicon, $CuIn(Ga)Se_2$ (known as CIGS) and CdTe are the most successful materials used in this category. Although efficiencies slightly surpass 20% and thin-film technologies entail significant cost reduction, the still high price is limiting their expansion. The use of rare and even toxic materials also hinders the establishment of this type of solar cells.

Finally, the third generation of solar cells face the challenge of lowering the cost under a new perspective. Besides using less amount of material, the material itself has to be as cheap as possible. On the other hand, high efficiencies are pursued by stacking multiple solar cells, which contribute to a more efficient light harvesting. This multijunction architecture has raised efficiencies up to 37.9% without light concentration.[10] New concepts and materials have conducted to unconventional devices, such as dye-sensitised solar cells (DSSCs) and organic solar cells, whose current record efficiencies are 11.9% and 12.0% respectively.[11,12] Particularly, organic photovoltaics have experienced a rapid growing, as they generate big expectations as a low-cost technology. The infinite possibilities that synthesis of organic semiconductors offer are a major advantage. A proper material design may address ideal properties for achieving high efficiency, low cost and long stability OPV, including broad and strong absorption, high conductivity and good solubility.

The progress made in the whole photovoltaics research field is regularly updated by NREL laboratories (see **Figure 1.2**).
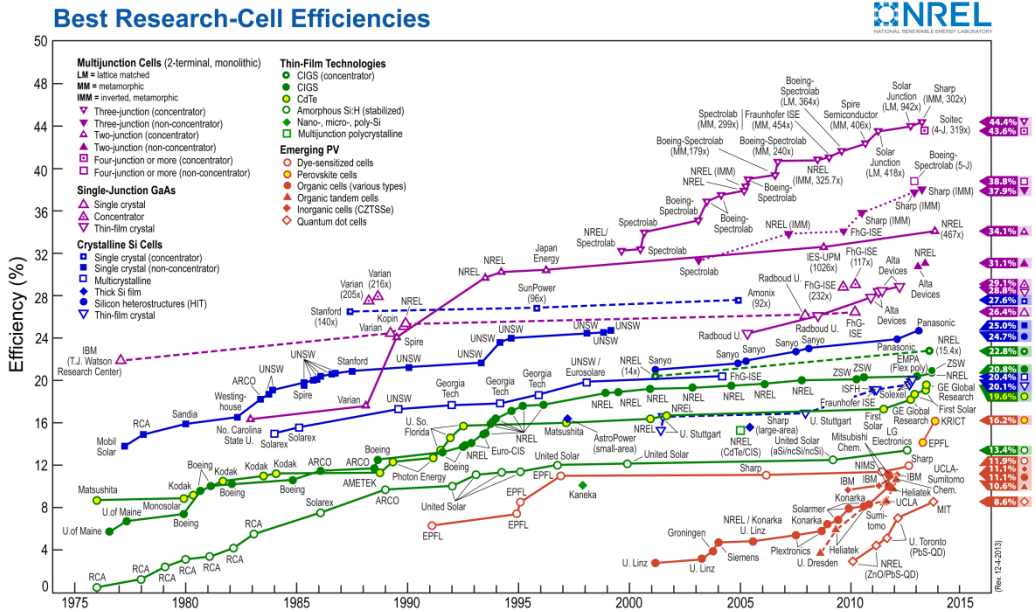
Figure 1.2. Progress in efficiency for different photovoltaic technologies according to the National Renewable Energy Laboratory (NREL); updated on 12/04/2013. Reproduced with permission.

1.2.3. Characteristics of the solar cells. Definitions

Before addressing the singularities of organic solar cells, general characteristics of solar cells are presented in this section.

The simplest equivalent circuit proposed for solar cells is depicted in **Figure 1.3**. It consists of 1) a source that provides (photo)current I_{ph}, under illumination, 2) a diode that gives saturation current I_0 (dark current at reverse bias), with an ideality factor n, 3) parallel (or shunt) resistance R_p, which considers current leakage and 4) series resistance R_s, that takes into account the resistivity of the semiconductors and electrodes as well as the resistance at interfaces. An ideal solar cell has infinite parallel resistance and zero series resistance.
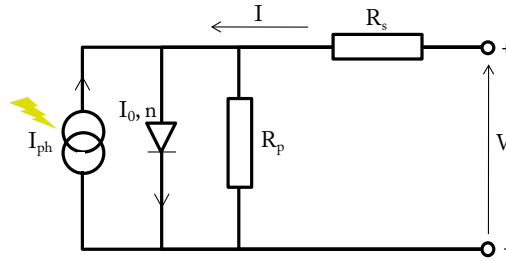
Figure 1.3. Equivalent circuit of a solar cell device.

1.2.3.1. Photocurrent and open circuit voltage

The amount of photocurrent generated in a solar cell is proportional to the intensity of incident light. One of the characteristics of a solar cell is the current obtained at short circuit conditions, I_{sc} (that is, when there is no potential difference between the two electrodes). As the current is proportional to the illuminated area, a more representative parameter is the *short circuit current density*, J_{sc}.

On the other hand, the available maximum potential difference between the contacts is the *open circuit voltage*, V_{oc}, where there is no current flow. V_{oc} is also subordinated to light intensity, showing a logarithmic dependence.[13]

At open circuit voltage (I = 0 A) as well as in short circuit conditions (V = 0 V), electrical power cannot be extracted. The optimum operational point for a photovoltaic device is called *maximum power point*. The product of voltage and current is at that point maximised.

1.2.3.2. I-V characteristics

In dark conditions solar cells behave like a diode. A typical rectifying behaviour is observed, i.e. much more current flow is allowed under forward bias (V > 0) than under reverse bias (V < 0). The rectification is maintained under illumination, but in this case a photocurrent is generated, which is then delivered to the external circuit.

The typical current-voltage characteristic of a solar cell is shown in **Figure 1.4**. The key performance parameters are therein included: short circuit current density J_{sc}, open circuit voltage V_{oc}, the maximum power point MPP and the corresponding voltage and current density at that point V_{mpp} and J_{mpp}. The fill factor FF, which defines the *squareness* of the J-V curve, is defined as the relation between the power extracted at the

maximum power point (yellow area in Figure 1.4a) and the maximum theoretical power extractable (grey area in Figure 1.4a):

$$FF = \frac{J_{mpp}\,V_{mpp}}{J_{sc}\,V_{oc}} \qquad [1.1]$$

The fill factor represents how efficient is the solar cell in collecting photogenerated charges. High rectification in the J-V characteristics is seen when the device is able to selectively transport and collect charges (electrons and holes) towards the corresponding electrodes.
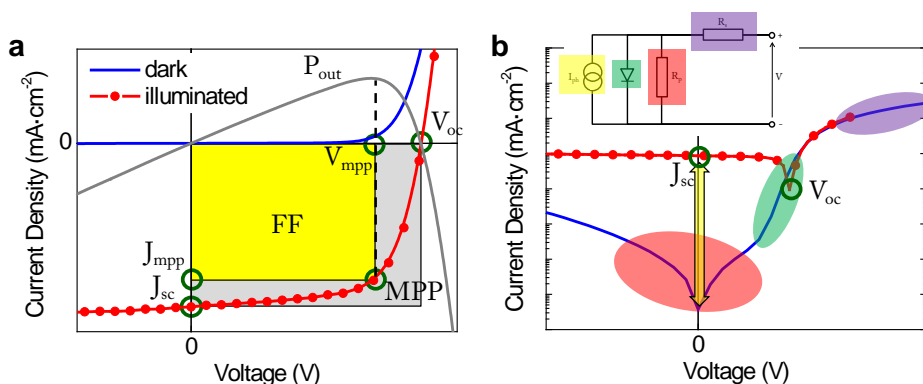

Figure 1.4. Typical current-voltage characteristics in a) linear and b) logarithmic scale and under dark and illuminated conditions. Some of the important parameters are indicated. Inset in b represents the simplified equivalent circuit of a solar cell, highlighting the regions of influence of each component in the I-V curve.

Ideally, the J-V curve under illumination is the superposition of the dark curve and the photogenerated current. At voltages above the V_{oc} both curves should converge; this is seen more clearly in Figure 1.4b. The typical rectifying behaviour is observable in both linear and logarithmic plots. More in detail, the dark curve in logarithmic scale is especially useful to identify different features affecting the device performance (see Figure 1.4b). In real solar cells, the current flow may be limited at low voltages (red area) by parallel resistance, while series resistances dominate at high voltages (violet area). In between, the opening of the diode is the governing factor (green area).

1.2.3.3. Power conversion efficiency

This is the main parameter that describes the performance of a solar cell. The power conversion efficiency (PCE) is a measure of the electric power delivered at operating

point (P_{out}) as a fraction of the power of incident light on the cell (P_{in}), and is related to J_{sc} and V_{oc} as follows:

$$PCE = \eta = \frac{P_{out}}{P_{in}} = \frac{J_{mpp}\,V_{mpp}}{P_{in}} = FF\frac{J_{sc}\,V_{oc}}{P_{in}} \qquad [1.2]$$

For standard characterisation, the power of incident light P_{in} has to match the spectrum irradiance of sunlight 1.5 AM at 1000 W·m^{-2}, as described in section 1.2.1.

1.2.3.4. The effect of parasitic resistances

As explained above, the efficiency of solar cells may be limited in real devices due to the presence of current leakage and resistances. The former occurs in poorly rectifying devices, where current flows through alternative, low resistive paths and is consequently lost. On the other hand, power can also be dissipated through resistances in series, which include the resistivity of the cell materials and contact interfaces, as stated previously. The negative effect of series resistance is more marked at high current densities.

Both parallel and series resistances hinder the fill factor, as shown in **Figure 1.5**. In extreme cases, they can even limit J_{sc} and V_{oc}.
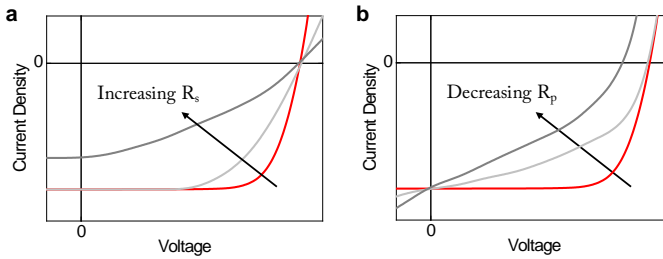

Figure 1.5. Negative effect of a) increasing series resistance and b) decreasing parallel resistance in the J-V characteristics.

1.2.3.5. Quantum efficiency

The quantum efficiency (QE) of a cell is the probability that an incident photon of certain energy will deliver one electron to the external circuit. QE equals 1 when every incident photon results in one collected charge. It is, therefore, a quantitative measurement of the energy conversion. The external quantum efficiency (EQE) is the ratio between the number of collected charges and the number of all incident photons on the solar cell at a given wavelength:

$$EQE = \frac{n_{electrons}}{n_{photons}} = \frac{E_{photon}I_{ph}}{P_{in}} \qquad [1.3]$$

If the energy of the photon (E_{photon}) is expressed as a function of wavelength (λ) using the conversion E (eV) $\cong$ 1240/λ (nm), then EQE can be determined by

$$EQE = 1240\,\frac{J_{sc}}{\lambda\,P_{in}} \qquad [1.4]$$

EQE is alternatively called IPCE, which stands for Incident Photon-to-electron Conversion Efficiency. As it is a function of incident photons, EQE spectra typically resemble the absorption spectra of the semiconductor material(s) of the solar cell.

On the other hand, the internal quantum efficiency (IQE) is the ratio between the number of collected charges and the number of all absorbed photons by the solar cell at a given wavelength. In this case, losses due to unabsorbed and reflected light are excluded (P_{in} equals the total incident light minus reflected, scattered and transmitted light).

1.2.4. Electronic structure of organic semiconductors. Conjugation

The presence of delocalised electrons in a material is a basic requirement for electrical conductivity, which is, in turn, essential in electronic devices. In organic molecules this delocalisation is much less marked than in crystalline semiconductors, and conductivity is consequently lower. The electronic structure of a molecule determines such delocalisation. In particular, π-orbitals provide this certain degree of freedom to electrons for moving. Large delocalisation is associated to conjugated systems, where single and double bonds are alternated.

In single atoms, electrons are organised in shells around the core. Each shell contains orbitals, spatial regions with high probability of finding a maximum of two electrons with different spins. For example, the electronic configuration of carbon, the cornerstone of organic chemistry, is $1s^2 2s^2 2p^2$. Therein, the symmetric s-orbitals of the first and second shell are fully occupied. In contrast, the two remaining electrons are located in two of the three degenerate p-orbitals ($2p_x$, $2p_y$ and $2p_z$). Up to six electrons can be hosted in these lobed-shaped orbitals, which means that four more electrons are needed to reach the electronic configuration of a noble gas (neon, in this case), having eight valence electrons. For the formation of a bond between two atoms, the

distribution of electrons is rearranged and new orbitals are constituted. This effect is called hybridisation. Single, double and triple bonds are created through sp^3, sp^2 and sp hybridisation, respectively.

In sp^3 hybridisation, an electron is transferred from 2s orbital to the empty 2p orbital, resulting in four sp^3 orbitals with one electron each. The overlap between these hybrid orbitals and either 1s or sp^3 orbitals of neighbouring atoms yields four σ bonds. In sp^2 hybridisation the 2s orbital is mixed with only two of the three available 2p orbitals. Three σ bonds are formed from the resulting sp^2 hybrid orbitals, while the unchanged p-orbital (2p) forms a π bond when overlapped with another 2p. Finally, sp hybridisation occurs when the 2s orbital mixes with only one of the three 2p orbitals. Therefore, two σ bonds and two π bonds are formed. When two p orbitals of similar phase overlap side-by-side, a π bonding molecular orbital results. When two p orbitals of opposite phase overlap side-by-side, a π* antibonding orbital results (see **Figure 1.6a**).

Table 1.1. Electronic configuration of C atom in ground, excited and hybridised states.

Ground state configuration	Excited state	sp^3	sp^2	sp
↑↓ ↑↓ ↑ ↑	↑↓ ↑ ↑ ↑ ↑	↑↓ ↑ ↑ ↑ ↑	↑↓ ↑ ↑ ↑ ↑	↑↓ ↑ ↑ ↑ ↑
1s 2s 2p$_x$ 2p$_y$ 2p$_z$	1s 2s 2p$_x$ 2p$_y$ 2p$_z$	1s sp^3 sp^3 sp^3 sp^3	1s sp^2 sp^2 sp^2 2p	1s sp sp 2p 2p

Benzene ring is an example of sp^2 hybridisation, with alternating single and double bonds. The unchanged p-orbital of each C atom is perpendicular to the plane of the ring. In the ground state, the six electrons are located in the 3 bonding (π) orbitals, while the 3 anti-bonding (π*) orbitals, with higher energy, remain empty (see Figure 1.6).
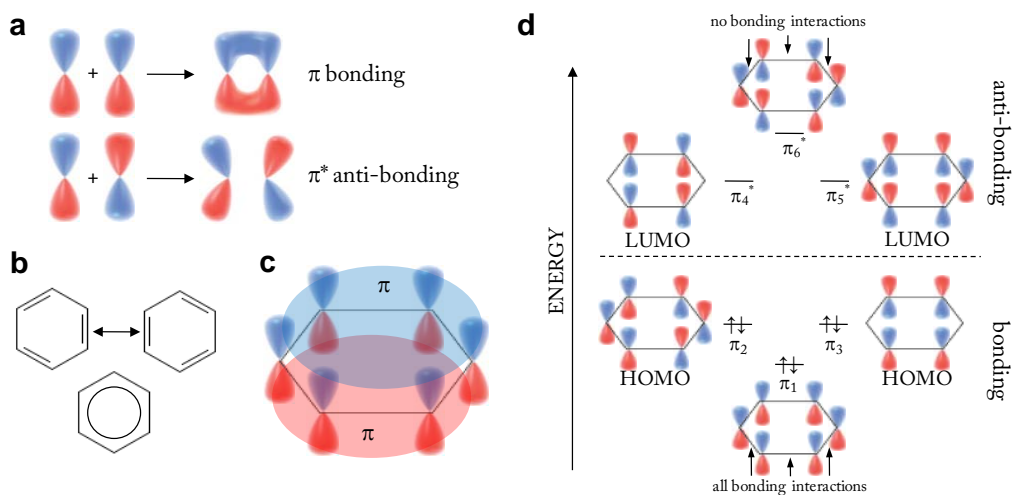
Figure 1.6. a) Formation of π bonding (π^* anti-bonding) orbitals through the overlap of p-orbitals with the same (opposite) phase. b) Resonant isomeric structures of benzene ring. c) Visualisation of π-orbital formation with all bonding interactions, which correspond to the lowest energy level. d) Position of the possible six energy levels as a result of the overlap of the six p-orbitals.

An extension of the π-system of a molecule by enlarging its conjugation results in i) further delocalisation, which entails higher conductivity, and ii) splitting of the energy levels, which decreases the energy band gap (see **Figure 1.7**).
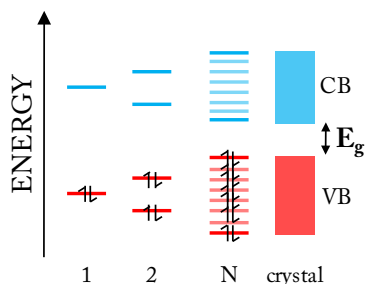

Figure 1.7. Schematic energy level diagram of atomic orbitals in inorganic semiconductors or insulators. When neighbouring levels are close in energy, effective bands (solid bars) are formed. The valence band (VB) is the highest occupied band while the conduction band (CB) is the lowest empty band. In organic semiconductors the HOMO and LUMO levels are their equivalents, respectively. Similarly, the band gap (E_g) is the considered as the difference between the two levels.

Compared to inorganic semiconductors, the highest occupied molecular orbital (HOMO) in the π-orbital is equivalent to the valence band, whereas the lowest unoccupied molecular orbital (LUMO) in the anti-bonding π^*-orbital correspond to

the conduction band. Consequently, the difference between HOMO and LUMO levels of a given molecule is considered the band gap.

1.2.5. Working principle of organic solar cells

As explained above, free charges are created upon excitation of electrons from valence to conduction band in inorganic materials. In contrast, photoexcitation does not lead to the formation of free charge carriers in organic semiconductors. Instead, bound neutral states, called *excitons*, are generated.[14] This electron-hole pair is coulombically attracted and needs to be dissociated into free charges in order to extract current. Exciton dissociation entails charge separation, the second necessary mechanism in PV process.

In single junction devices, defects or impurities were found to be responsible for exciton dissociation in the first OPV devices.[15] As this process is highly inefficient, other approaches were proposed to promote charge separation. An important advance was the introduction of the bilayer heterojunction concept,[16] where a p-type and n-type based layers are stacked together. The energy offset in the molecular orbitals between donor and acceptor materials makes possible to split the exciton into free charge carriers. In heterojunctions this splitting is preceded by charge transfer, as the excited electron is transferred from donor to acceptor. What is important to remark is that this mechanism takes place in the interface between the two materials. On the other hand, it is known that the diffusion length of a formed exciton is in the order of 10 nm for most organic semiconductors.[17] Therefore, all excitons generated in planar heterojunctions at larger distances from the *p-n* interface decay before reaching that interface and are lost.[18] At the same time, thicknesses of about 100 nm are usually needed to absorb a high proportion of the incident light; hence the limitation of the bilayer approach arises. The main breakthrough in organic solar cells was the so-called bulk heterojunction (BHJ) system, in which the active layer is formed with an intimate mixing of the donor and the acceptor materials.[19] This resulted in a significant increase in the effective interface area and thus, in charge separation efficiency. A suitable morphology of the blend is therefore essential for obtaining high efficient devices. Moreover, after charge transfer occurs, free charges need to find percolating pathways to the relevant electrodes to be extracted, which is also facilitated by adequate layer morphology. Considering these aspects, the ideal BHJ morphology was proposed as a bicontinuous interdigitated network between donor and acceptor, being the size of

nanodomains in the order of the exciton diffusion length.[20] All these approaches and mechanisms are summarised in **Figure 1.8**.
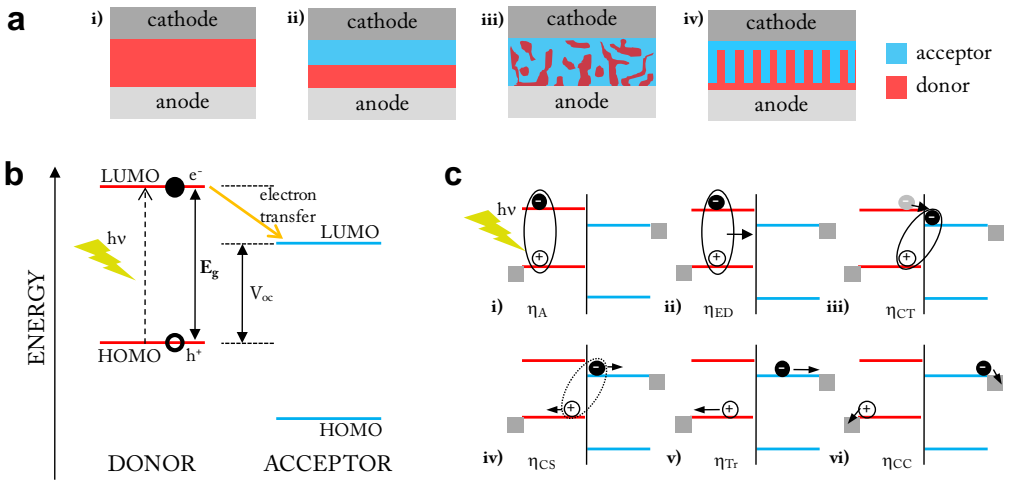

Figure 1.8. a) Possible realisations for the active layer: i) single layer, ii) planar bilayer heterojunction, iii) bulk heterojunction, iv) ideal, interdigitated blend. b) Energy level diagram of a donor:acceptor system. c) Charge generation and extraction in organic solar cells: i) absorption of light results in exciton formation, ii) exciton diffusion towards the donor:acceptor interface, iii) charge transfer from the donor to the acceptor, iv) dissociation of the electron-hole pair into free charges (charge separation), v) charge transport of free carriers towards the electrodes, vi) charge collection. Possible loss mechanisms that compete with each process are i) not absorbed photons, ii-iv) non-radiative (thermal) decay or radiative (monomolecular or geminate) recombination of the exciton, v) recombination of free charges with other opposite charges (bimolecular recombination) or falling into traps.

The external quantum efficiency of organic solar cells is limited by the efficiency of each step in charge generation and extraction:

$$\eta_{EQE} = \eta_A\eta_{IQE} = \eta_A\eta_{ED}\eta_{CT}\eta_{CS}\eta_{Tr}\eta_{CC}$$

[1.5]

The first two mechanisms, absorption and exciton diffusion, are determined by the nature of the semiconductor material, especially by its electronic configuration and conjugation. On the other hand, the morphology of the blend film rules the rest of mechanisms. As explained above, suitable layer morphology assists an efficient charge transfer and separation at donor-acceptor interface, while free charges will be efficiently transported and collected to appropriate electrodes if adequate percolating pathways are present in the film structure. In contrast, unsuitable morphology results in losses in charge extraction because recombination mechanisms become predominant. We talk

about geminate or monomolecular recombination when an exciton decays to the ground state, either non-radiatively (thermalisation) or radiatively (photoluminescence), before splitting into separate charges. Bimolecular recombination occurs when two opposite free charges, originally generated from different excitons, find each other and recombine. These losses in charge extraction can be deduced from J-V characteristics when poor rectifying curves are obtained.[21]

1.2.6. OPV device architecture

The basic organic solar cell structure consists of two electrodes of different work function, at least one of them being transparent, and an active layer in between, where the photovoltaic effect takes place. Different approaches for the active layer have been discussed in previous section. In this geometry, the resulting electric field between the two contacts when a voltage is applied is not enough for complete selective charge separation and transport to appropriate electrodes. This limits the fill factor of the device. For that reason it is usual to include interface layers that a) block holes or electrons or b) enhance transport of only one type of charge. As a result, the typical organic solar cell architecture is a multilayer stack, as shown in **Figure 1.9**.
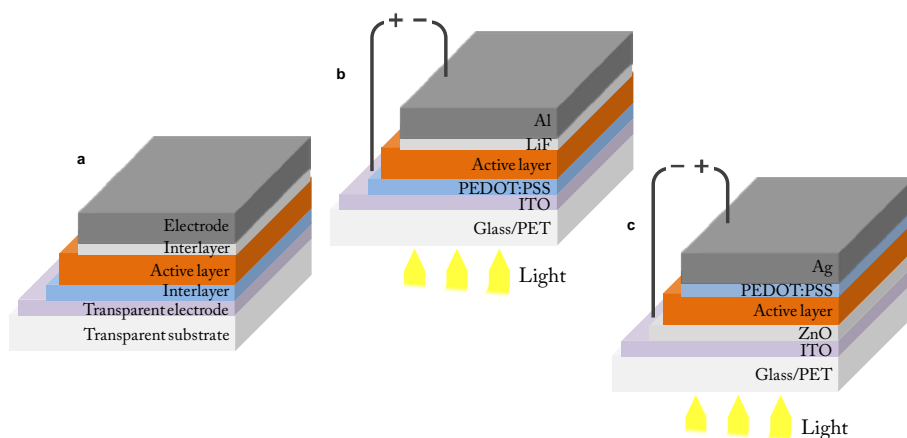

Figure 1.9. a) Typical architecture of an organic solar cell. Two examples of b) normal and c) inverted geometries.

The energetic levels of the materials used in the structure determine the current flow direction. Standard or normal configuration corresponds to that in which electrons are collected at the top metallic electrode, which acts as the cathode. Current flows in the opposite direction in inverted configuration, where the metallic electrode acts as the

anode. Examples of each structure are depicted in Figure 1.9. The main advantage of inverted structure is its higher stability. First, the frequently used ITO/PEDOT:PSS interface, which is chemically unstable,[22] is avoided. Second, unstable buffer layers such as LiF or Ca are not necessary with Ag being the top electrode. Ag is more stable than Al, and is eventually solution-processable. Normal structured devices are, therefore, usually encapsulated to prevent degradation due to moisture or oxygen.

Besides the use as buffers, interface layers can sometimes provide further advantages, including reduction of traps due to better contact between layers or enhancement of light harvesting by optimising the optical properties of the multilayer structure.[23] Still, the core of the solar cell is the active layer and, consequently, it has attracted most of the research in the field. Next section is dedicated to the materials employed in this layer.

1.2.7. Active layer materials

The great advances in BHJ solar cells since the beginning of this technology have been largely driven by the development of conjugated polymers, used as electron-donating materials. It is nevertheless worthwhile to remark the huge importance of fullerene derivatives as electron acceptors in OPVs, especially [6,6]-phenyl-C_{61}-butyric acid methyl ester ($PC_{60}BM$) and [6,6]-phenyl-C_{71}-butyric acid methyl ester ($PC_{70}BM$) (see structures in **Figure 1.10**).
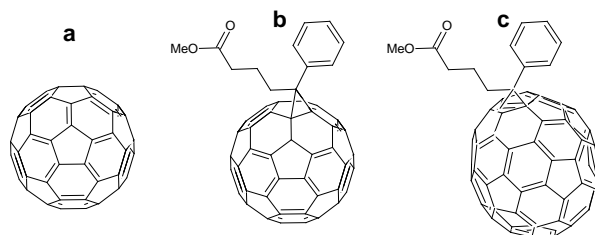

Figure 1.10. Chemical structures of a) C_{60} buckminsterfullerene, b) $PC_{60}BM$ and c) $PC_{70}BM$

They show superior properties, including high electron mobility, solubility in many solvents or adequate shape for percolating (polymer) donor networks, among others. So important they are in OPV research that they are still the most widely used acceptors after more than 15 years of research.[24] On the other hand, the research in donor materials has been by far more successful. A brief review of the progress done is provided next.

As explained in section 1.2.4, the band gap (E_g) of an organic semiconductor is defined as the difference between its lower unoccupied molecular orbital (LUMO) and highest occupied molecular orbital (HOMO) energy levels (Figure 1.8b). Therefore, an electron can be excited (i.e. taken from HOMO to LUMO) only when a photon with an energy equal or higher than E_g is absorbed. On the other hand, it is more or less accepted that the V_{oc} of a solar cell is governed by the difference between the LUMO level of the acceptor and the HOMO level of the donor, provided ohmic contacts.[25]

The energy difference between the LUMOs of the donor and acceptor represents the energetic driving force for a forward electron transfer from the donor to the acceptor. It has been found that an energy difference of ~0.3 eV is needed to produce the exciton splitting and charge dissociation.[26] Consequently, when the LUMO-LUMO offset is larger, part of the absorbed energy is lost. **Figure 1.11** shows how energy level engineering can be used to reduce these losses.
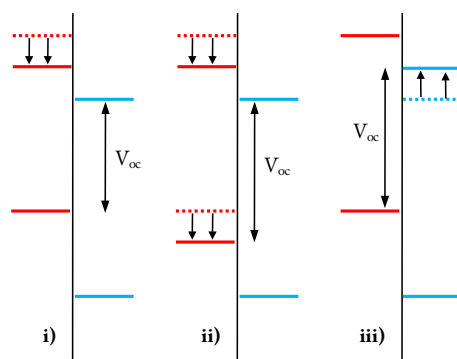

Figure 1.11. Energy losses during electron transfer can be minimized through different strategies: i) lowering the LUMO of the donor, ii) lowering the LUMO and HOMO of the donor or iii) raising the LUMO of the acceptor.[27] The last two options provide an enhancement in V_{oc}.

The LUMO-LUMO offset can be diminished by lowering the LUMO of the donor or increasing the LUMO of the acceptor. The latter provides further increase in V_{oc}. There is, however, a more important reason that pushes the researchers to tune the energy levels and, in particular, to lower the energy band gap of the donor.

Assuming that solar cells convert photons into electrons in a 1:1 ratio maximum (which is essentially true, besides unusual phenomena such as two-photon absorption), the available energy of the photons provided from the sun needs to be known for a proper choice or design of absorbing materials. In this sense, the representation of the

solar spectrum in photon flux as a function of wavelength gives an accurate input.[28] As it can be seen in **Figure 1.12**, the maximum of this spectrum is located at approximately 700 nm (1.8 eV). Ideally, the absorption spectra of the donor material should overlap as much as possible with that spectrum to maximise exciton generation.
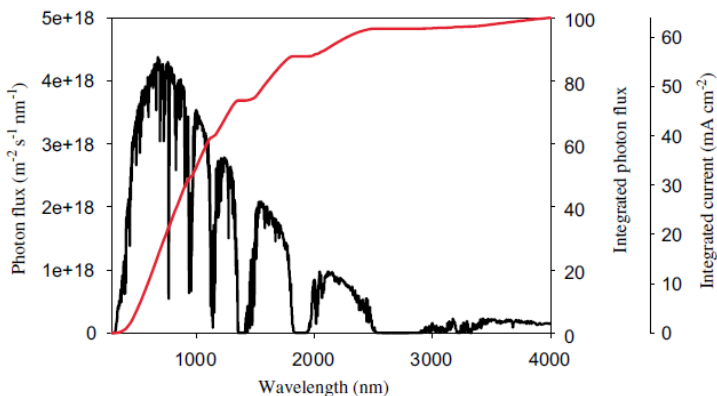

Figure 1.12. Photon flux from the sun (AM 1.5G) as a function of wavelength. On the right axis the integral of the curve (red line) is shown as the percentage of the total number of photons and as obtainable current density. Reproduced with permission from reference [28]. Copyright 2007, Elsevier B.V.

Moreover, the obtainable current density (red line in Figure 1.12) also indicates that harvesting photons at longer wavelengths (this is with lower band gap) would lead to higher current extraction. However, the energy of the charge carriers at longer wavelengths is lower, and thus the delivered voltage of the device would decrease. Therefore, this compromise between the number of harvested photons and their energy leads to the conclusion that there is an optimum band gap that drives to highest efficiency. Scharber and co-workers estimated the ideal band gap to be near 1.45 eV.[29,30]

The first family of conjugated polymers that were used successfully as donor materials were based on poly(phenylenevinylene)s (PPV), reaching efficiencies up to 3.3%.[31] A representative example is the poly[2-methoxy-5-(3′,7′-dimethyloctyloxy)-1,4-phenylenevinylene] (MDMO-PPV) (**Figure 1.13**). Later, regioregular poly(3-hexylthiophene-2,5-diyl) (P3HT) emerged as a more efficient material, showing superior charge mobility and efficiencies reaching 5%.[32] The main disadvantage of these two polymers is the poor matching of their photon absorbance with the photon flux solar spectrum. The bandgap of MDMO-PPV (E_g = 2.2 eV) as well as of P3HT

(E_g = 1.9 eV) are above the 1.8 eV maximum, and far from the ideal 1.45 eV. This limited absorption impedes a more effective photon harvesting.[33]
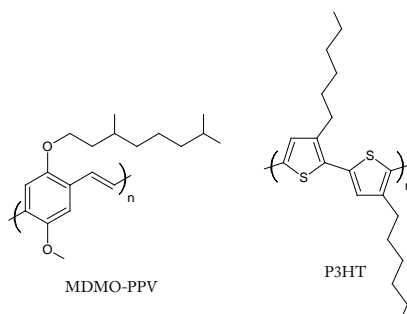

Figure 1.13. Chemical structures of poly[2-methoxy-5-(3′,7′-dimethyloctyloxy)-1,4-phenylenevinylene] (MDMO-PPV) and poly(3-hexylthiophene-2,5-diyl) (P3HT).

Further development was afterwards focused on lowering the band gap of the polymers, owing to the reasons explained above. Special attention was set on alternating copolymers. The incorporation of alternating donor-acceptor units in the polymer backbone as well as conjugated bridging units has been used to modulate the properties of the polymers, including, of course, their energy band gap. Moreover, the nature of side chains and substituents can tune these further, as well as other important properties like solubility. Currently, many different units with electron-donating or electron-accepting character have been identified. Some examples are shown in **Figure 1.14** (donor character) and **Figure 1.15** (acceptor character).
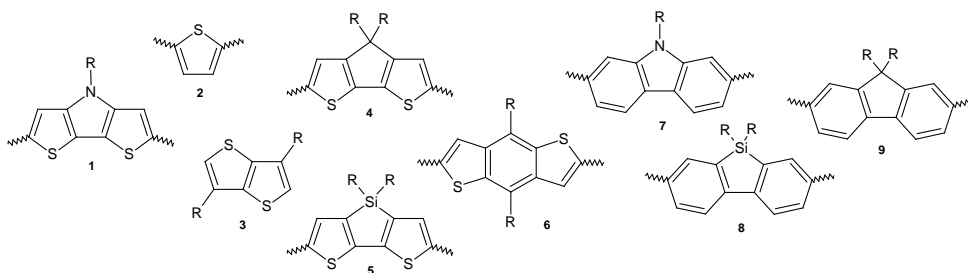

Figure 1.14. A selection of commonly used electron donor units, sorted by donating capability (empirically, from ref. [34]). 1) dithienopyrrole, 2) thiophene, 3) thienothiophene, 4) cyclopentadithiophene, 5) silol bithiophene, 6) benzodithiophene, 7) carbazole, 8) silafluorene, 9) fluorene.
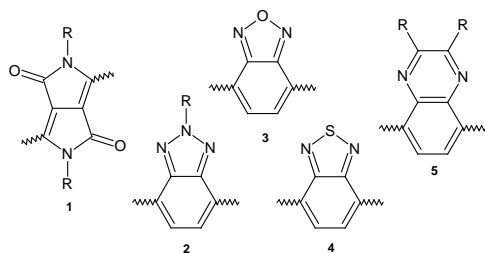
19

Figure 1.15. Some commonly used electron acceptor units. 1) dioxopyrrolopyrrole, 2) triazole, 3) benzoxadiazole, 4) benzodiathiazole, 5) quinoxaline.

As said before, a common tendency in the design of low band gap polymers is to combine electron donating and accepting units in the polymer main chain. Some examples (see **Figure 1.16**) include poly[(9,9-dioctylfluorenyl-2,7-diyl)-alt-5,5-(40,70-di-2-thienyl-20,10,30-benzothiadiazole)] (APFO3), poly[N-9′-heptadecanyl-2,7-carbazole-alt-5,5-(4′,7′-di-2-thienyl-2′,1′,3′-benzothiadiazole)] (PCDTBT), poly[2,6-(4,4-bis-(2-ethylhexyl)-4*H*-cyclopenta[2,1-b;3,4-b′]-dithiophene)-*alt*-4,7-(2,1,3-benzothiadiazole)] (PCPDTBT), thieno[3,4-b]thiophene/benzodithiophene (PTB7) and poly[{2,5-bis(2-hexyldecyl)-2,3,5,6-tetrahydro-3,6-dioxopyrrolo[3,4-c]pyrrole-1,4-diyl} -alt-{[2,2′-(1,4-phenylene)bisthiophene]-5,5′-diyl}] (PDPPTPT).
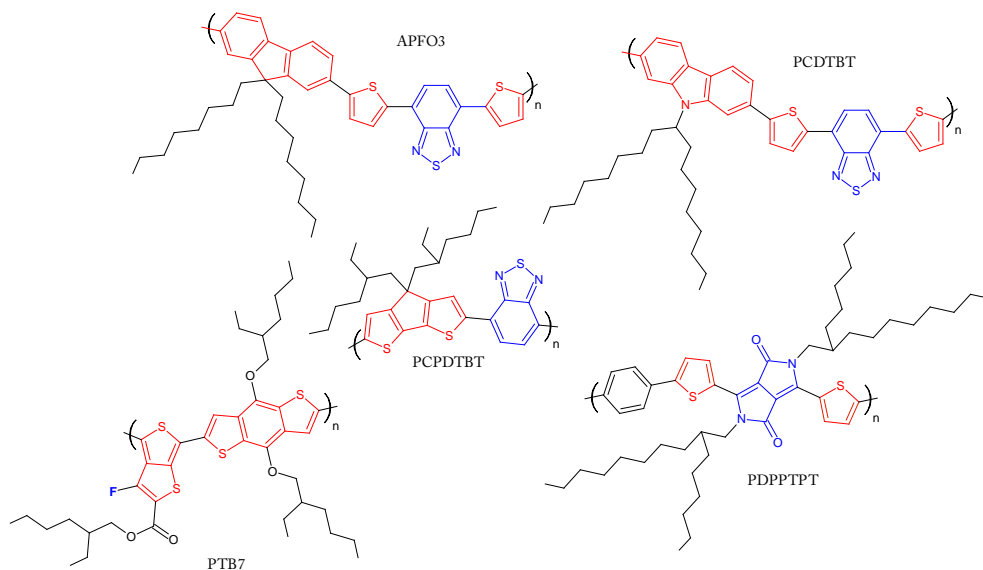

Figure 1.16. Representative selection of low band gap polymers containing electron donor (red) and electron withdrawing (blue) units in their backbone.

A summary of the energetic levels of this selection of conjugated polymers is shown in **Table 1.2**, together with their representative OPV performance parameters.

Table 1.2. Energetic levels of some conjugated polymers and reported photovoltaic performance parameters of devices using these donor materials.

DONOR Polymer	HOMO (eV)	LUMO (eV)	E_g^{opt} (eV)	V_{oc} (V)	J_{sc} (mA·cm^{-2})	FF (%)	PCE (%)	ref
ideal[a]	-5.4	-3.9	1.45	-	-	-	11-15	[29,30]
MDMO-PPV	-5.33	-2.97	2.2	0.82	5.25	61	2.5	[35]
P3HT	-4.8	-2.9	1.9	0.63	9.5	68	5	[32]
APFO3	-5.7	-3.4	1.9	1.04	5.76	58	3.46	[36,37]
PCPDTBT	-5.3	-3.57	1.38	0.62	16.2	55	5.5	[38,39]
PCDTBT	-5.5	-3.6	1.88	0.88	11.32	69	6.9	[40,41]
PDPPTPT	-5.35	-3.53	1.50	0.80	14.0	67	7.4	[42]
PTB7	-5.15	-3.31	1.68	0.76	15.7	70	8.4	[43,44]

[a] Considering PCBM as the acceptor

Table 1.2 shows a significant improvement in PCE when the band gap drops below 1.9 eV. Thanks to engineering of the energy levels, high V_{oc} can be achieved while keeping high short circuit current densities. This balance is essential for obtaining high PCE. It is not the case, for instance, of APFO3 and PCPDTBT, which show impressive V_{oc} and J_{sc}, respectively, but the corresponding low J_{sc} and V_{oc} respectively limit the performance of the device. However, considering that these two polymers show also lower FF, other factors besides the energetic levels may be restricting the cell response. The responsible for this may be the difficulty to process these materials to obtain optimal polymer:acceptor blend morphology. An optimum morphology has to promote charge separation and favoured transport of photogenerated charges.

CHAPTER 2

General methods and materials

Abstract

The materials, processing methods and characterisation techniques used throughout the results presented in this thesis are described in this chapter. Among the methods used, special emphasis has been put on three solution processing techniques: spin coating, doctor blade coating and inkjet printing. Detailed recipes developed for common materials are given. In the section dedicated to characterisation, it may be worth saying that the setups for electrical characterisation of OPV devices, including J-V and EQE measurements, were built at the beginning of this thesis.

2.1. MATERIALS

The materials used during this thesis are listed below, following the sequential order of the standard arquitecture of the OPV devices: anode/electron blocking layer/active layer/hole blocking layer/cathode

Anode

Patterned 25 x 25 mm ITO-coated glass slides were purchased from PsiOTec Ltd. The pattern consisted in a central pad (19 x 25 mm), as shown in **Figure 2.1**.
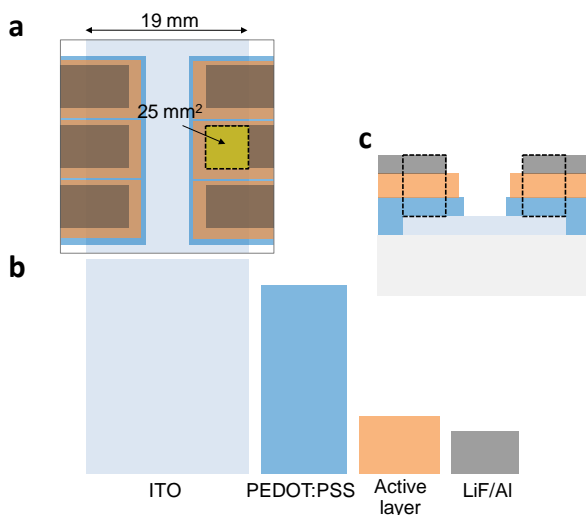
Figure 2.1. Scheme of the device geometry. a) Front view, b) decomposition of a standard configuration device in single layers (being PEDOT:PSS and active layer inkjet printed and LiF/Al thermally evaporated), and c) cross section view. The intersection (dashed line) between ITO pattern and evaporated metal cathode defines the active area of the 6 solar cells contained in each substrate.

Two thicknesses of the ITO layer were employed. At the beginning, low sheet resistance (ρ = 5 Ω/sq) ITO was pursued, which required a 420 nm thick layer. However, the step at the edge of the pattern was too high and often resulted in current leakage. Therefore, the thickness of the ITO was reduced to 230 nm, which led to a sheet resistance of 10 Ω/sq. On the other hand, some tests with flexible substrates were performed as well, although the results are not presented in this thesis.

For the ITO-free samples (chapter 5), the Ag grids were fabricated by a) thermal evaporation through UV lithographic mask (99.99% Ag pellets from Kurt J. Lesker) or

b) inkjet printing, using a nanoparticle-based Ag ink (SunTronic EMD 5603 from SunChemical).

Electron blocking/hole transport layer

A transparent semiconductor PEDOT:PSS layer was coated on top of the anode in all the cases. The vast majority of the experiments were done with IJ-1005 PEDOT:PSS ink from Agfa-Orgacon. Other inks were used in concrete works, such as Pjet HC (from Heraeus) for the vapour printing experiments (chapter 3, section 3.3) or Clevios P VP Al4083 (from Heraeus) 1:3 diluted in isopropanol for the work done at i-MEET (chapter 4, section 4.2).

Active layer

Bulk heterojunction systems were built for all the studies. 96% regioregular P3HT (from Rieke Metals), PCDTBT (from 1-Material), PTB7 (from 1-Material) and a D-π-A star-shaped material, $N(Ph-2T-DCN-Et)_3$ (supplied by Heraeus) were used as donor materials. On the other hand, only two acceptor materials were employed: >99% purity $PC_{60}BM$ and $PC_{70}BM$, both purchased from Solenne BV. Almost all the solvents and additives used in this thesis were used as delivered from Sigma-Aldrich. These include: chlorobenzene, o-dichlorobenzene, mesitylene, 1,2,3,4-tetrahydronaphthalene, tetrahydrofuran, benzaldehyde, cyclohexane, dimethyl sulfoxide, propylene carbonate, p-bromoanisole and 1,8-diiodooctane. Common solvents such as acetone, 2-propanol, ethanol or methanol were purchased from Panreac.

Hole blocking layer

Typically two materials were thermally evaporated: LiF powder or Ca pellets (from Sigma-Aldrich).

Cathode

Finally, Al or Ag pellets (99.99% purity, from Kurt J. Lesker) were used as cathode materials in the final evaporation step.

Encapsulation

When the samples were encapsulated, a ultra-violet curing epoxy resin (Loctite 358 or 350) was used to ensemble them with 20 x 20 x 0.2 mm covering glass slides.

2.2. PROCESSING TECHNIQUES

This section describes the main fabrication techniques used for the development of this thesis.

2.2.1. Substrate preparation

Both ITO-coated glass and only-glass substrates were cleaned with soap water and successively ultrasonicated in acetone (15 min) and isopropanol (15 min). After nitrogen drying, the ITO substrates were treated with UV-O$_3$ for 10 min. Instead of this, an alternative 10 min O$_2$-plasma treatment was performed in some cases, especially for the ITO-free substrates (chapter 5).

2.2.2. Deposition of solution processable electrodes, transparent semiconductor and photoactive materials

Mainly three different processing methods were used in the studies reported in this thesis to deposit up to three layers of the standard OPV device configuration: metallic grid electrodes were fabricated by inkjet printing while PEDOT:PSS and the active layer were processed by spin coating, doctor blade and inkjet printing. In this section these three techniques are briefly described and general fabrication recipes are detailed. Nevertheless, a deeper comparison of these three processing methods is given in chapters 3 and 5.

2.2.2.1. Spin coating

Without any doubt, this is the most widely used technique for researchers in OPV manufacturing. It is straightforward, and high homogeneous layers with controlled thickness are easily obtained. The process consists in disposing the solution on top of the substrate, which is immediately rotated to spread the material and the film is progressively dried (see **Figure 2.2**).
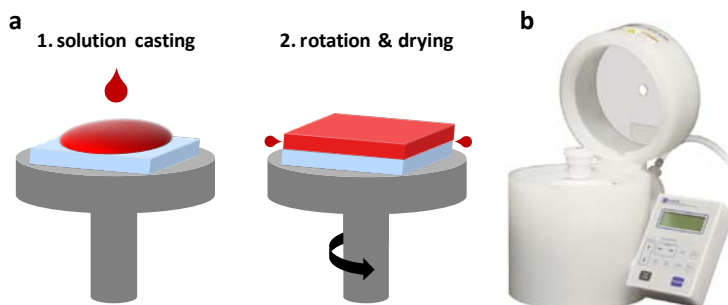
Figure 2.2. Spin coating a) process and b) equipment, from Laurell Technologies.

Besides solution concentration and viscosity, and the interaction between the ink and the substrate, the parameters that determine the final thickness of the layer are, in order of importance: the angular velocity, the time of spinning and solvent drying kinetics.[45] As an example, **Figure 2.3** shows the correlation between angular velocity and layer thickness for PEDOT:PSS (Pjet HC) coated on top of glass. This relation is known as spin curve. Intuitively, the slower is the rotation, the thicker the layer is, and vice versa.
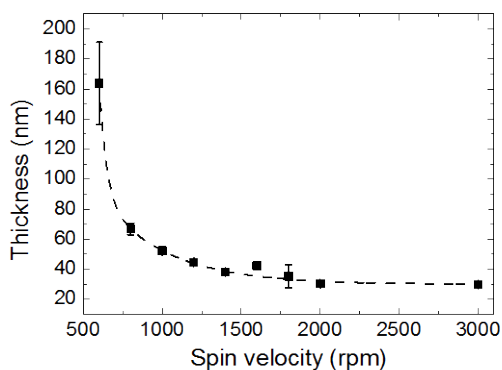
Figure 2.3. Spin curve of PEDOT:PSS coated on glass.**Table 2.1** shows two general recipes followed in this work for the deposition of PEDOT:PSS and P3HT:PCBM active layers. Typically, an initial spinning step of 500 rpm for 2s was performed in order to achieve a complete and homogeneous spreading on the substrate.

Table 2.1. General recipes for spin coating PEDOT:PSS and P3HT:PCBM layers.

Ink	PEDOT:PSS		P3HT:PCBM (1:1)
	Pjet HC	IJ1005	50 mg/mL in CB
Filtering	0.2 μm PVDF	-	-
Speed (rpm)	1500	1500	2000
Time (s)	90	90	90
Final thickness (nm)	50	45	160

2.2.2.2. Doctor blade

This technique is also easy to handle and permits depositing larger areas than spin coating. Moreover, because of its working principle, it can be closely compared to slot die coating, a method typically used in roll-to-roll lines. It is thus an interesting process, considering that minor changes are needed to make the transfer from lab to large scale fabrication. Layers from 20 nm to several hundreds of microns thickness can be obtained by doctor blading.

In this process, a controlled amount of ink is disposed in between the blade applicator and the substrate, which are separated by a determined distance. Because of this gap, a meniscus is formed (see **Figure 2.4**). Then, the blade is moved under controlled velocity and the resulting wet film is dried. The drying kinetics can be altered by adjusting the substrate temperature.
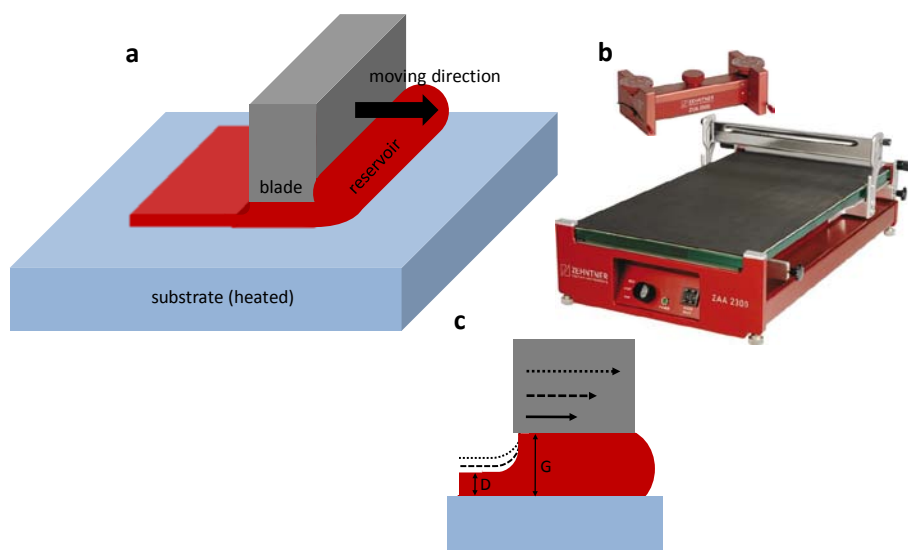
Figure 2.4. Doctor Blade a) process and b) Zehntner ZAA 2300 equipment (bottom) together with ZUA 2000 universal applicator (top) used in this thesis. c) Meniscus formation and influence of blade speed. The maximum wet thickness (D) obtainable is about 50% of the gap distance (G).

In a similar manner as in spin coating, the final thickness of the film depends on i) ink properties, including solid content, ink rheology and solvent drying rate, and on ii) coating parameters: the blade speed, the gap between blade and substrate, the amount of ink and temperature control. Among these, the blade speed is the parameter with bigger impact on the film thickness. As Figure 2.4c shows, the faster is the blade, the thicker the film is. The latter may seem counter intuitive. The responsible for this is the meniscus formation: with high speeds the meniscus is less pronounced due to the shorter time of interaction between the ink and the blade. On the other hand, a higher height of the gap results in thicker layer, although the maximum thickness achievable is approximately 50% of the gap.[46]

Typically higher layer homogeneity is achieved by lowering the gap and blade speed. In turn, temperature adjustment is essential to address suitable drying for good layer morphology, which is particularly important in bulk heterojunction layers. Common recipes followed in this work are summarized in **Table 2.2**.

Table 2.2. General recipes for Doctor blade coating PEDOT:PSS and P3HT:PCBM layers.

Ink	PEDOT:PSS[a]	P3HT:PCBM (1:1) 20 mg/mL in CB
Volume (µL)	60	65
Gap (µm)	400	400
Blade speed (mm/s)	10	15
Temperature (ºC)	50	65
Final thickness (nm)	50	160

[a] Two successive layers were coated, with an intermediate annealing step (5 min at 90 ºC). Valid for Orgacon IJ1005 and Clevios P VP Al4083 inks.

2.2.2.3. Inkjet printing

Besides traditional graphical applications, inkjet printing (IJP) has also been used in the last few years as a fabrication tool in advanced areas of technology. Many different devices have been demonstrated with this technique, including thin film transistors, light emitting diodes, memory devices, organic solar cells, conductive structures, sensors and biological applications.[47]

By using inkjet printing, it is possible to deposit thin films (from tens of nanometers to tens of microns) from dissolved or dispersed materials on any planar surface, including flexible substrates, in a reproducible manner. The accurate positional location of individual, picoliter droplets that are ejected from a piezoelectric-controlled nozzle represents a big advantage, since digital patterning leads to efficient material-saving and prevents from the need of expensive masks. Moreover, contamination is minimized because inkjet printing is a non-contact deposition method. A typical resolution in the micrometer scale can be achieved by using lab-scale printers. The processing speed depends on the number of printing jets. Currently, commercially available tools can simultaneously use up to 1024 jets, which enable printing at speeds of 500 mm/s.[48] Furthermore, the compatibility of inkjet printing with R2R processes makes it industrially relevant. The working principle consists in 3 steps: 1) droplet formation and ejection, 2) positioning, spreading and coalescence of droplets on a surface and 3) solvent evaporation and other mechanisms that result in a dried, solid

film (see **Figure 2.5**). For a deeper description of the printing mechanism the reader is referred to extensive reviews.[49,50]
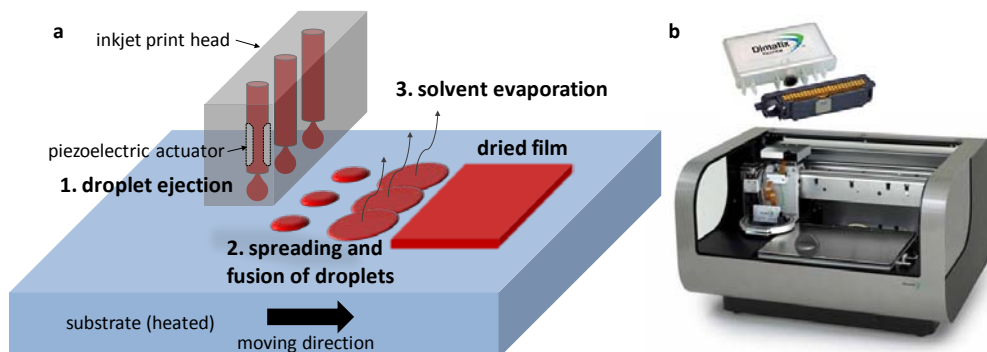

Figure 2.5. Inkjet printing a) process and b) Fujifilm Dimatix DMP-2831 equipment used in this thesis.

On the other hand, inkjet printing is considered as a slow drying technique, in contrast to faster drying processes such as spin coating. This, together with the difficulty to control all the processing parameters, has been a constraint for a widely spreading of this processing tool in the field of OPV. A deep understanding of the technique itself as well as of the parameters affecting the drying behaviour is mandatory to achieve homogeneous layers, even more when specific layer morphology is intended, as it is in the active layer of organic solar cells. Unlike other, more robust coating methods, inkjet printing needs specific ink requirements to be fulfilled. Both the rheology and formulation determine whether the ink is printable. Depending on the technical specifications of the printing tool, these requisites will be more or less strict. Of special importance are the viscosity and surface tension of the solution. Additionally, the modification of the ink properties will affect the drying behaviour and film formation. For instance, a typical trouble related to inkjet printing is the so called coffee stain effect, a migration of the deposited material to the edges of casted drops during film formation, especially with long drying times. This is explained in more detail in chapter 3. Also, nozzle clogging can occur if solid precipitates within the jet, provided that the nozzle orifice is open to the atmosphere. Therefore, it is recommended to use high boiling point solvents, as their lower vapour pressure delay this phenomenon. More in detail, solvent mixtures containing high boiling point solvents are usually employed to prevent nozzle clogging and coffee ring effect (see chpter 3, section 3.1.2).

Since printing parameters have a big influence on all these aspects, they can be carefully used to adapt or compensate ink characteristics, in order to reach the desired dried film. In the particular case of the DMP-2831 printing tool used in this thesis, some of these strategies include i) raising cartridge temperature (up to 70 ℃) to reduce ink viscosity and increase droplet ejection speed, ii) raising substrate plate temperature (up to 60 ℃) to modify the drying behaviour of the wet film, iii) adjusting the drop spacing in order to obtain proper droplet coalescence, drying kinetics and the desired film thickness, and iv) optimising the waveform of the piezoelectric print head to achieve reliable jetting.

In terms of ink jettability, an appropriate driving waveform is particularly important. So influent it is that some inks would not be otherwise printable. Moreover, fine tuning might result in high-quality droplet formation, i.e. round droplets without satellites or tails. **Figure 2.6** shows the typical operation of a piezoelectric actuator as a function of the waveform along the whole droplet ejection cycle. The parameters that mostly determine the droplet formation quality are the duration of segments 1 and 2 and the slope at segment 2. When testing a new ink, this optimisation step is essential.
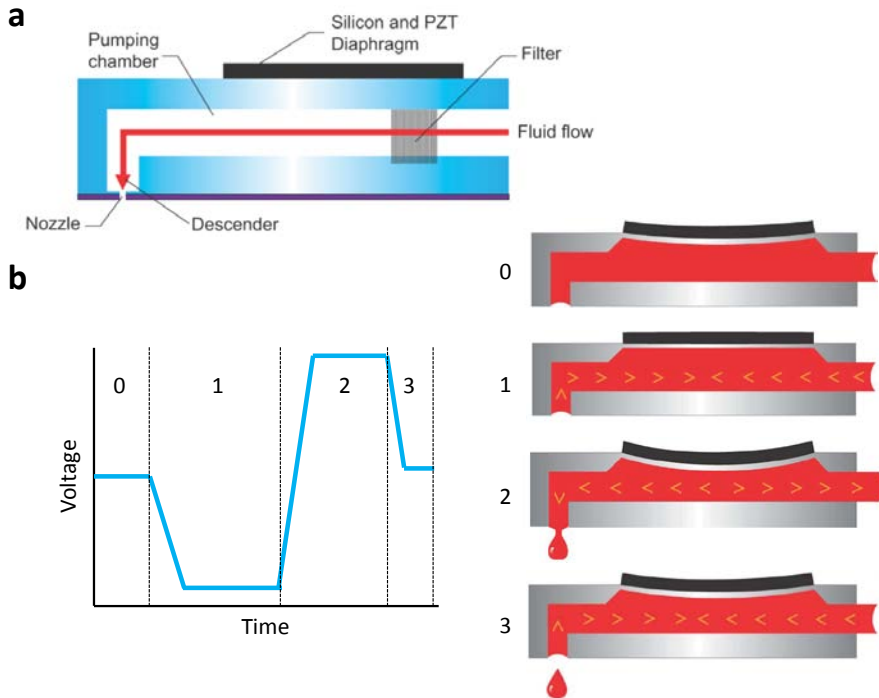
Figure 2.6. a) Cross section of a micro-electro-mechanical jet. b) Basic waveform (left) and the correspondence to the piezoelectric (PZT) actions (right). The PZT is slightly deflected by a bias voltage in standby mode (0). When the voltage is decreased to zero (1), the PZT is moved upwards, pulling fluid from the reservoir. At this point the chamber is at its maximum volume. An increase in voltage (2) deflects the PZT and the chamber compression initiates droplet formation. Finally, a controlled recovery to standby position (3) results in drop release. Figures reproduced with permission from Fujifilm Dimatix, Inc.

The higher complexity of inkjet printing in comparison to the previous two methods requires further efforts for testing new materials and inks. **Table 2.3** shows the general inkjet printing recipes used in this thesis.

Table 2.3. General recipes for inkjet printing Ag, PEDOT:PSS and P3HT:PCBM based inks.

Ink	**Ag** SunTronic EMD 5603	**PEDOT:PSS** Orgacon IJ-1005	**P3HT:PCBM** (1:1) 20mg/mL in DCB/mesitylene (68:32)
Cartridge			
Type	Standard	Standard	LCP (liquid cryst.)
Volume (pL)	10	10	10
Temperature (ºC)	RT	RT	50-60
Voltage (V)	29	24-25	25
Drop speed (m/s)	13	14	6-8
Number of jets	1-5	3-5	2
Waveform			

PlateTemp. (ºC)	RT	RT	40
Drop spacing (μm)	40-50	30-35	30
Final thickness (nm)	130-250	40	160

Typically the samples were transferred to a nitrogen filled glovebox after the coating of the active layer. Depending on the active materials, an annealing step was performed

prior to cathode evaporation. In the case of P3HT:PCBM based samples, for example, this step consisted in heating at 140 °C for 10 min. For PEDOT:PSS the typical annealing step, prior to active layer deposition, consisted of heating at 90 °C for 15 min in a fume cabinet.

2.2.3. Deposition of hole blocking layer and top metal electrode by thermal evaporation

The final step in the fabrication of OPV devices with standard configuration consisted in evaporating top metal electrodes through a shadow mask at high vacuum ($\leq 3 \cdot 10^{-6}$ mbar). A thermal evaporation system (from Kurt J. Lesker) attached to a glovebox was used for this step process (see **Figure 2.7**). The thickness of deposited layers as well as the rate of evaporation was carefully monitored by using an oscillating quartz crystal. The active area was set to 25 mm^2, defined as the geometrical overlap between the ITO pattern and the evaporated cathode, as shown in Figure 2.1.

Figure 2.7. Back (left), lateral (middle) and front (right) views of the evaporation chamber attached to a glovebox.

An intermediate hole blocking layer was usually evaporated between active and electrode layers, in order to increase charge collection selectivity.[31] Typically 0.6-1 nm of LiF was evaporated at low rates (0.1 Å/s) prior to 100 nm Al. The latter was evaporated in two steps: the first 15 nm were deposited at 0.5 Å/s and then the evaporation rate was increased to 1-2 Å/s. The thickness of LiF may have a big influence in OPV performance, thus it was consequently optimised depending on both active layer materials and roughness. For instance, P3HT:PCBM based solar cells required 0.8-1 nm of LiF while 0.6-0.8 nm were used for PCDTBT:PC$_{70}$BM and

PTB7:PC$_{70}$BM based devices. On the other hand, 15 nm of Ca were evaporated at 0.5 Å/s when Ag was chosen as the top electrode (85 nm at 1-3 Å/s). Some tests without hole blocking layer evaporation were also performed, as explained in chapter 3. In such cases, further thermal annealing was required after cathode evaporation to improve interface contact by Al diffusion into the blend layer.[32] Alternatively, high Al evaporation rate (≥ 3 Å/s) can be used to obtain a similar morphology.[51] In all cases a high substrate rotation speed (20 rpm) was set in order to minimize border shadowing effects.

2.2.4. Encapsulation

Some of the samples were encapsulated with a glass cap (20 x 20 x 0.2 mm) using an ultraviolet curing epoxy resin (Loctite 350 or 358). The 15 s exposure to the UV radiation (90 mW·cm^{-2}) was performed from the metal side to avoid photodegradation of the organic layers across the active region. Ideally this procedure should be performed in inert atmosphere immediately after cathode evaporation.

2.3. CHARACTERISATION TECHNIQUES

This section describes the primary characterisation techniques used in this thesis, including characterisation of inks, layers and complete OPV devices. The latter include a description of the built set-up for optoelectronic measurements.

2.3.1. Characterisation of inks

Considering that one of the objectives for lowering the cost of OPV technology is to achieve reliable solution processability, it is mandatory to address suitable ink formulation. Appropriate ink properties permit high-quality coating of layers in a reproducible manner. Those properties must fit the requirements of the corresponding deposition technique and result in an adequate film morphology formation.

2.3.1.1. Rheology

The first thing that an ink has to accomplish in order to be processable is to fulfill some rheological requisites, which will depend on the employed coating method. These ink properties can be classified as a) intrinsic, including viscosity and surface tension and b) related to the substrate surface, this is, contact angle. The normal procedure used during this thesis when testing new formulations consisted in

measuring these properties in order to see if they fitted the corresponding, suitable range. Suitable viscosity ranges are 1-40 mPa·s, 1-10,000 mPa·s and 1-40 mPa·s for spin coating, doctor blading and inkjet printing, respectively.[52] On the other hand, the optimal surface tension range for reliable ejection in inkjet printing is 28-36 dynes/cm.[53]

A HAAKE RheoStress 6000 universal rheometer (from Thermo Scientific) was used for measuring viscosities, using double cone geometry. The determination of both surface tension of liquids and contact angle of inks on top of substrates was carried out with a Drop Shape Analysis System DSA100 (from Krüss). This system makes an image analysis to calculate those properties. Pendant drop type and Laplace-Young calculation method were used for surface tension measurements. On the other hand, sessile drop type was set for contact angle determination, while the calculation used Laplace-Young, tangent or circle method for low, medium and high contact angle, respectively.

2.3.1.2. Spectroscopy

Valuable information about the quality of dissolved materials in solution can be obtained by UV-Vis spectroscopy. The interaction of solvents with (semiconductor) solutes[54] and features such as aggregation,[55] deficient solubility[56] or gelation[57] of dissolved polymers along time are detectable by this optic, non-invasive technique. Moreover, absolute solubility of dissolved materials can be determined, as it is shown in chapter 4.

For this characterisation, a Perkin-Elmer Lambda 950 UV-Vis spectrophotometer was used in transmission mode.

2.3.2. Characterisation of layers

Once the film is formed, further characterisation may give insights into important physical properties of layers that might influence OPV device performance. As explained in the first chapter, the morphology of the layers governs critical properties such as exciton dissociation and charge transport and collection.

2.3.2.1. Microscopy

The very first analysis one can do after film formation is a macroscopic visual inspection. Many times this is enough to detect inhomogeneities, including coffee stain

and the presence of big aggregates, and qualitatively perceive inadequate film thickness (or variations in thickness across the film through variations in colouration).

Smaller aggregates, holes and even lateral phase segregation (in films made of blends) are observable by optical microscopy. In this thesis a Nikon Eclipse LV100D microscope was used for these analyses.

2.3.2.2. Spectroscopy

Several spectroscopic measurements were performed in the work presented in this thesis to characterise different aspects of the fabricated films.

In a similar manner as in the characterisation of solutions, UV-Vis spectroscopy was measured, with the same equipment, also after film formation. Therein, other relevant features such as the degree of polymer crystallisation[58] and exciton bandwith[59] can be determined.

Alternatively, Raman and photoluminescence (PL) spectra provide valuable information that may help to deduce film morphology. Changes in Raman modes may indicate, for instance, differences in polymer ordering or crystallisation.[60] In turn, PL signal is a signature of radiative recombination, thus it gives information about how efficient charge transfer is;[61] the latter is related to domain size and the degree of donor-acceptor intermixing. These features were characterised with a LabRam HR800 spectrometer (Jobin Yvon) excited with a 488-nm UV diode laser coupled through an Olympus microscope into an argon-filled sample chamber. The laser spot focused on the samples was less than 5 μm in diameter.

On the other hand, variable angle spectroscopic ellipsometry (VASE) gives insights into relevant optical properties of materials, molecular ordering and vertical phase separation in blend films.[62] A GESP 5 SOPRALAB rotating polarizer ellipsometer with built-in CCD detection was used for this characterisation. A confocal objective was used for focusing the incident light beam into a spot about 250 μm wide (in the short direction of the elliptical projection). The model used to analyze the VASE data was carefully adapted to the nature of the (blend) materials.

2.3.2.3. Morphology

Atomic force microscopy (AFM) characterisation was performed using an Agilent 5100 microscope in tapping mode. This type of surface scan gives information about the topology and roughness of the layer as well as about eventual lateral domains in the sub-micrometer scale.

Besides the information about surface topology that AFM measurements provide, faster characterisation of dried films was performed with a Veeco Dektak 150 Profilometer to determine film thickness.

2.3.3. Electrical characterisation of OPV devices

2.3.3.1. J-V characterisation

The current–voltage characteristics of the solar cells were measured under AM 1.5G (Air Mass 1.5 Global) illumination, 100 mW·cm^{-2}. In the first stages of this thesis, an Oriel Research Arc Lamp Source (150 W Xe lamp) and a Keithley 2400 Sourcemeter were used for the measurements, under ambient conditions. In this set-up the power density of the incident light was calibrated *in situ* with a Newport thermopile sensor and a power meter with a beam splitter (see **Figure 2.8a**). Later, we had access to an Atlas SolarTest 1200 solar simulator (class BAA, area 0.4 m^2). The light power density was therein calibrated by using a pyranometer. For the data collection we developed a software tool using LabVIEW graphical language platform.
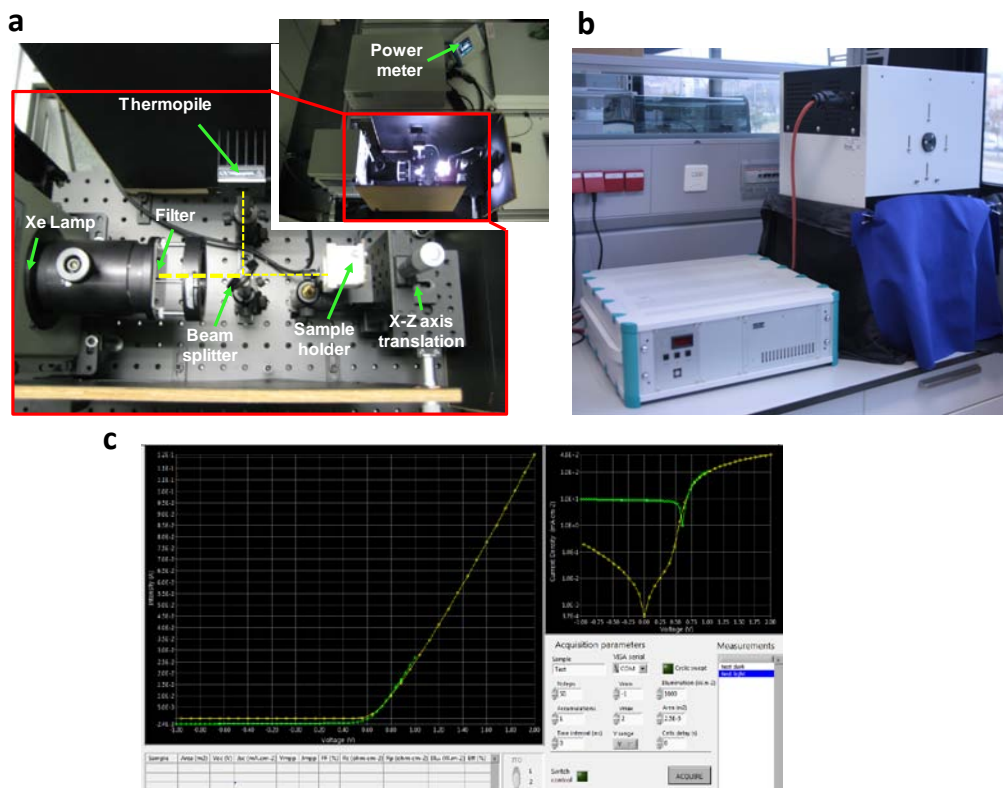
Figure 2.8. a) Solar simulator based on the Oriel Research Arc Lamp Source, b) Atlas SolarTest 1200 commercial solar simulator, c) snapshot taken from the software developed for measurements.

2.3.3.2. External Quantum Efficiency

The external quantum efficiency (EQE) was determined with the setup shown in **Figure 2.9**. The light emitted by a 75 W Xe lamp is focused inside a monochromator; the outgoing, monochromated light is driven and focused on top of the sample. Similarly as in the setup for J-V characterisation, the light beam is splitted to measure in real time the power density of light at each wavelength, using a calibrated photodiode and a power meter. The short circuit current is measured at each wavelength with a Keithley 2400 Sourcemeter. Another software tool was developed with LabVIEW in order to control all of these components. This software included an option for sequential EQE measurements at different positions, controlled by a motorized translation stage. This option was used for doing some measurements shown in chapter 3.
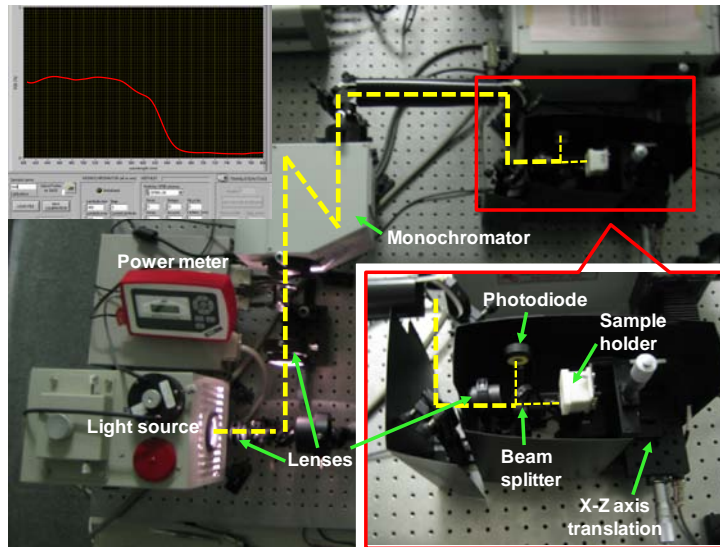
Figure 2.9. EQE setup and developed software caption (top left).

It has to be said that this setup has two limitations for a complete quantitative characterisation. First, due to the lack of a chopper with a lock-in amplifier we could not get rid of residual base noise. The latter was especially marked at wavelengths with low power density of light (in this case, below 400 nm), where the signal to noise ratio is no longer negligible. This is precisely the second limitation: too low power density of light in the UV range inhibits EQE data collection therein.

For the calibration of the beam splitter response, a simple software tool was created. The power density of light at each wavelength is measured with the photodiode at 1) sample holder location and 2) photodiode location. The resulting correlation is then used by the primary software to calculate the real power density of light in real time.

CHAPTER 3

Inkjet and vapour printing of P3HT:PCBM based solar cells

Abstract

Current research in new materials and architectures for organic photovoltaic devices has pushed up record cell efficiencies over 10%. Still, the P3HT:PCBM bulk heterojunction blend is a workhorse material system, mostly because of price, performance and reproducibility, and so it is often chosen to demonstrate new concepts. Even so, some questions remain unsolved. For example, it is yet not fully understood how processing (and post-processing) conditions rule the nanomorphology of the active layer. On the other hand, spin coating and doctor blading are still widely used for solar cells fabrication despite being the former not compatibile with roll-to-roll processing. The study of large-scale compatible technologies like inkjet printing is therefore essential.

In this chapter the optimisation of the processing and post-processing conditions of organic solar cells with PEDOT:PSS and P3HT:PCBM functional layers deposited by inkjet printing is discussed. It is shown that several interconnected parameters govern the drying process of the film, which in turn determines the morphology of the layer. Further optimisation lead to overall efficiencies above 3% using different coating techniques. A crossed comparison between spin coating, doctor blading and inkjet printing is presented, contrasting their benefits and drawbacks. Finally, the use of vapour printing as an alternative, faster post-processing method of the active layer is demonstrated. The influence of vapour printing time as well as the solvent vapour pressure on the morphology of the P3HT:PCBM layer is investigated.

3.1. OPTIMISATION OF INKJET PRINTED DEVICES

3.1.1. State of the art of organic solar cells made by inkjet printing

Relevant improvements have been achieved in the last 6-7 years in OPVs processed by inkjet printing. Interestingly, examples of individual inkjet printed layers in normal structured OPVs can be found in literature. For instance, the formulation of an ink containing ITO nanoparticles has been reported.[63] Alternatively, relevant results in ITO-free devices based on inkjet printed current collecting grids based on silver inks have also been published.[64,65] Galagan and co-workers inkjet printed both silver grids and PEDOT:PSS layers and obtained 1.54% efficient devices with 4 cm² area.[66] Other works focused on PEDOT:PSS layers include a comparative study between spin coating, spray coating and inkjet printing[67] and the optimisation of the PEDOT:PSS ink formulation.[68] Using solvent additives, higher homogeneity and conductivity as well as lower roughness were achieved. However, the main research interest has been focused on the active layer, mostly in the workhorse P3HT:PCBM material system. Most of the reports have studied the effect of individual parameters in the performance of OPVs. The effect of the blend concentration was related to surface roughness by Aernouts et al.[69] It was found that higher blend concentrations tend to give rougher layers. Moreover, an interesting approach consisting in mixing high and low boiling point solvents in inkjet printing was presented by Hoth and co-workers.[70] More than a twofold increase in PCE was obtained with an o-dichlorobenze/mesitylene solvent mixture in comparison to pristine tetralin. Therefore, the solvent composition has a big influence in the drying process and the morphology of the film. The same group showed how inks based on high boiling point solvents give higher roughness in inkjet printed layers (RMS of 26.0 nm and 7.4 nm for THN and DCB/mesitylene, respectively).[71] A special emphasis was placed on the regioregularity of the P3HT polymer.[71,72] Another multiparametric study in inkjet printed active layers allowed to identify some of the critical parameters and their crossed relationships: viscosity, temperature of the substrate, drop spacing and the height between nozzle and substrate.[73] The best OPV performance reported up to now with inkjet printed P3HT:PCBM layers was achieved by Eom et al. with the addition of 1,8-octanedithiol as a high boiling point additive (PCE = 3.71%).[74] The latter as well as the work reported by Lange et al.[75] have the extra merit of including inkjet printed PEDOT:PSS and active layers. It is concluded in many works that a careful study of ink formulation and printing conditions is essential to obtain homogeneous films with adequate

morphology for best OPV performance. Also, some physical properties such as contact angle between the solution and the substrate need to be studied to be sure that an optimal wetting is achieved. Another relevant approach used inkjet printing for combinatorial screening of polymer:fullerene blends with low material investment.[76] Finally, top electrodes have been printed as well using metallic nanoparticle inks.[77] **Table 3.1** summarizes these recent advances in inkjet printed OPV devices.

Table 3.1. Performance of OPV based on P3HT:PCBM with at least one layer processed by inkjet printing.

Device structure[a]	Solvent[b]	V_{oc} (V)	J_{sc} (mA·cm⁻²)	FF (%)	PCE(%)	Area (cm²)	Ref.
glass/**ITO/PEDOT:PSS**/P3HT:PCBM/Ca/Al	EtOH	0.47	8.3	47.5	1.8	0.0625	63
glass/Ag/HC–PEDOT/P3HT:PCBM/LiF/Al		0.54	5.30	53.4	1.52	4	64
glass/Ag/HC–PEDOT/P3HT:PCBM/Al		0.51	10.35	36.8	1.96	0.09	65
glass/**Ag/HC–PEDOT**/P3HT:PCBM/LiF/Al		0.50	6.37	48	1.54	4	66
glass/ITO/**PEDOT:PSS**/P3HT:PCBM/Ca/Al		0.62	9.78	52.9	3.31	NA	67
glass/ITO/**PEDOT:PSS**/P3HT:PCBM/LiF/Al	+glycerol+EGBE	0.60	9.59	55.3	3.16	0.09	68
glass/ITO/PEDOT:PSS/**P3HT:PCBM**/Al	CB:THN (1:1)	0.66	4.67	46	1.4	0.03	69
glass/ITO/PEDOT:PSS/**P3HT:PCBM**/Ca/Ag	DCB:mesitylene (68:32)	0.54	8.4	64	2.9	0.2-1	70
glass/ITO/PEDOT:PSS/**P3HT:PCBM**/Ca/Ag	THN	0.45	4.73	63	1.29	0.2-1	70
glass/ITO/PEDOT:PSS/**P3HT:PCBM**/Ca/Ag	DCB:mesitylene (68:32)	0.54	10.05	64	3.47	0.2-1	71
glass/ITO/PEDOT:PSS/**P3HT:PCBM**/Al	CB:TCB (55:45)	0.57	9.34	45	2.40	0.16	75
glass/ITO/PEDOT:PSS/**P3HT:PCBM**/Ca/Ag	DCB	0.53	12.12	63.2	3.07	0.09	73
glass/ITO/**PEDOT:PSS/P3HT:PCBM**/Al	CB:TCB (55:45)	0.51	8.94	34	1.54	0.16	75
glass/ITO/**PEDOT:PSS/P3HT:PCBM**/LiF/Al	CB:ODT (10:0.5)	0.63	10.68	55.3	3.71	0.09	74
glass/ITO/ZnO/P3HT:PCBM/PEDOT:PSS/**Ag**		0.51	8.39	45.5	1.96	1	77

[a] The layers processed by inkjet printing are marked in bold

[b] used in the inkjet printing step. Commercial inks when not specified

We considered the lessons learned in these works and our own experience to create a table which may give a general overview of the interplay of the main parameters involved in the inkjet printing process (see **Table 3.2**). The processing parameters are classified as ink, substrate or inkjet printer dependent, and correlated to different aspects of the processing steps. We tried to discern between strong and weak interactions. For example, the concentration of a solution (solid content in the table) is directly related to the thickness of the dried film, while the effect of firing voltage is less evident; a higher voltage results in larger drop volume and faster ejection, which in turn result in film thickening.

Table 3.2. Crossed interactions between processing parameters (rows) and the effects within the printing process (columns). The strength of the dependence is represented by the size of the spot (red coloured when critical).

		Ejection					Spreading		Drying	Film formation				
		nozzle clogging	jetability	drop shape	volume	speed	drop diameter	coalescence	time	resolution	thickness	roughness	depth composition	lateral homogeneity
Ink	solid content	•	•	•							•	•		
	solvent mix	•	•				•	•	•	•			•(red)	•
	viscosity		•(red)	•		•	•	•						•
	surface tension		•(red)	•		•	•	•		•				•
	vapour pressure	•(red)	•						•(red)			•		
Substrate	surface properties						•	•		•			•(red)	•
	temperature						•	•	•(red)	•			•	•(red)
IJP parameters	nozzle diameter	•	•		•		•	•		•				
	cartridge temperature	•	•	•		•	•	•						
	piezo waveform		•	•(red)	•	•	•	•			•	•		
	firing voltage		•		•	•	•	•		•	•	•		
	printhead height						•	•		•				
	number of jets								•		•		•	•
	drop spacing							•	•			•(red)	•	•

The results obtained so far are encouraging despite this multi-parametric puzzle evidencing that a deep control of inkjet printing process is not trivial. Moreover, according to all these reports, there is no fundamental limitation to implement inkjet

printing for processing all the layers to construct OPV devices. Indeed, a six-layer stack, ITO-free solar cell fully made by inkjet printing has been recently announced by the Solliance consortium.[78] The authors claim that all six layers were produced at R2R compatible speeds. In line with this, a remarkable inkjet printing integration into a roll-to-roll equipment was used by Angmo et al. to produce silver grids as electrodes for ITO-free devices.[79] It is thus clear that inkjet printing is attracting more and more interest as an OPV production tool.

In the following sections two issues related to the slow drying of inkjet printed films are addressed. Firstly, coffee stain effect is mitigated by using adequate mixtures of solvents. Secondly, different aspects affecting the drying kinetics are discussed. Once suitable layer morphology is obtained, other aspects limiting OPV performance are studied. Specifically, different approaches for improving interface contact are implemented. The latter results in better diode rectification, thus in higher fill factor.

3.1.2. Mixing two solvents to avoid coffee stain

As said in chapter 2, an undesired coffee ring feature can appear after film formation in slow drying processes like inkjet printing. This accumulation of the dissolved material(s) at the edges after drying is due to a combination of contact line pinning of the droplet and faster solvent drying at the edges,[80] which creates a gradient of concentration, thus a subsequent liquid flow appears (see **Figure 3.1**). Normally it has a bigger influence with longer drying times.[81] This feature can be suppressed, for example, through an adequate design of solvent mixtures, as proposed by de Gans et al. They showed how a mixture of high boiling point, low surface tension solvent with a low boiling point, high surface tension solvent led to a more homogenous layer. A Marangoni flow due to a new gradient of surface tension appeared in the opposite direction of the former gradient, thus the migration of the material was mitigated.[82]

Figure 3.1. Schematic representation of the drying process of a wet film (cross section view) with (a-c) one solvent and (d-f) a mixture of a high boiling point, low surface tension solvent and a low boiling point, high surface tension solvent. When the process starts (a) and (d) the liquid evaporates faster at the edges due to the higher surface to volume ratio (green arrows). This provokes an increase of the local concentration of the solution at the edges. To compensate this gradient of concentration the solvent migrates to the edges (blue arrows in b and e), lugging the dissolved material with him. With one solvent this leads to the coffee ring (c). With the described mixture of solvents, the faster evaporation of liquid at the edges leads also to a gradient of surface tension due to the different evaporation rates of the two solvents. To compensate this new gradient, the low surface tension solvent flows from the edges to the centre of the drop (red arrows in e), resulting in uniform thickness of the dried film (f).

Additionally, it is important to remember that low boiling point, pristine solvents may not be suitable for inkjet printing. To inkjet print a solution of a P3HT:PCBM blend in our inkjet printer machine it is mandatory to avoid the use of volatile solvents such as chlorobenzene to prevent nozzle clogging.[70] As a consequence of this, the drying time of the printed films gets longer. Hence inhomogeneities and larger phase separation of components are more likely to happen in inkjet printing as compared to faster coating techniques such as spin coating or doctor blading.

A simple study, herein presented, was performed to detect coffee ring formation in films processed from a) pristine or b) a mixture of solvents. P3HT:PCBM layers were printed from one (o-dichlorobenzene) or two (o-dichlorobenzene:mesitylene 68:32) solvents on top of spin coated and later annealed PEDOT:PSS layers. This solvent mixture is the same used in reference 70. Different drop spacing were used in order to see the effect of drying time. The results are shown in **Figure 3.2**.
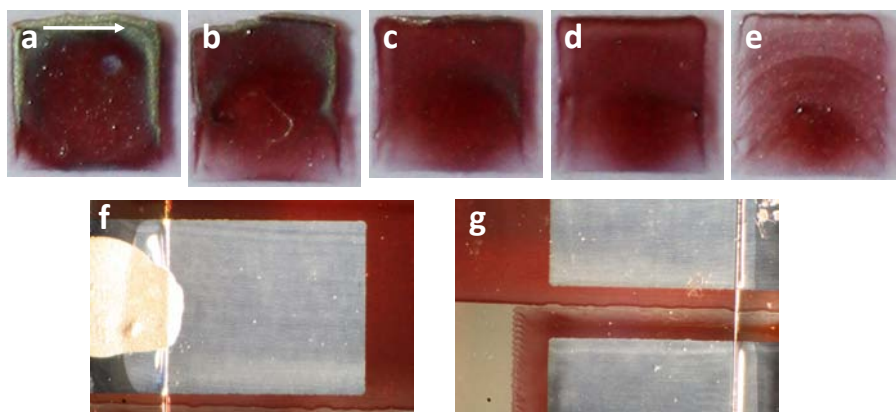
Figure 3.2. P3HT:PCBM layers (2.5 x 2.5 mm) inkjet printed from a DCB solution at a) 20 µm, b) 25 µm, c) 30 µm, d) 35 µm and e) 40 µm of drop spacing. The coffee ring is present in all the layers, being more visible when lower drop spacing (longer drying time) is used. (f-g) In contrast, this effect is notably diminished in samples made with the DCB:mesitylene (68:32) at 30 µm of drop space (red coloured layers). Images f-g are taken from real OPV devices. White arrow in a) indicates printing direction.

The effect of drying time is evident: the longer it is, the more marked is the coffee stain effect, when using only one solvent. On the other hand, a clear improvement in the homogeneity of the layers is seen in the samples made from solutions containing the mixture of solvents. These results support related previous works presented in literature.[69–71] Most of the OPV devices made by inkjet printed presented in this thesis have been fabricated from solutions based on mixture of solvents. Further results obtained with mixtures of non-halogenated solvents are shown in chapter 4.

3.1.3. Study of the drying kinetics

The nanomorphology of the active layer in bulk heterojunction devices determines the photocurrent of the solar cell.[83] In turn, nanomorphology depends itself markedly on the drying kinetics[84,85] in solution-based processes.

There are several specific parameters in inkjet printing that can affect the drying kinetics of the printed layers, being the temperature of the substrate, the drop spacing, the number of jets and the printed pattern the most determinant. This section shows the effect of each individual parameter on the drying kinetics and the final morphology of the P3HT:PCBM based active layer.

Temperature of the substrate

The evaporation rate of a wet film is directly proportional to the vapour pressure of the solvent(s), which in turn is related to the temperature. Thus, the higher is the temperature of the substrate, the faster the drying of the film is.

P3HT:PCBM (1:1) 2% wt. solutions in THN:mesitylene (9:1) were inkjet printed on top of spin coated and later annealed PEDOT:PSS layers. In this solvent combination, THN acts as the carrier solvent while mesitylene assists ink spreading. The substrate temperature was varied from room temperature to 60 ºC to print different layers. The drop spacing was set at 30 μm and the printing was performed with 5 consecutive jets. The rest of inkjet printing parameters were kept as usually for the P3HT:PCBM system, described in general methods (chapter 2). Microscopic images as well as the macroscopic visual aspect of the resulting layers are shown in **Figure 3.3**.
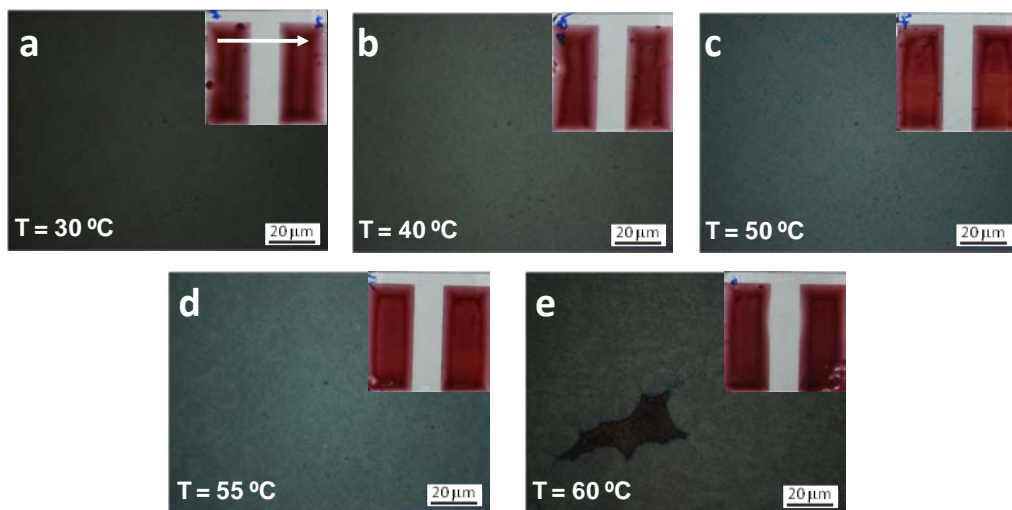
Figure 3.3. Optical microscopy images of P3HT:PCBM layers inkjet printed at different substrate temperatures. Macroscopic images are depicted in the insets. White arrow indicates inkjet printing direction.

From the insets in Figure 3.3 it can be deduced that lower coffee ring effect is obtained with increasing temperature. This is in accordance to the description of this phenomenon.[80] Faster drying may reduce the migration of material to the edges of the layer. However, coffee ring is still present. Therefore, the chosen solvent mixture would not be suitable for OPV processing. On the other hand, PCBM aggregates are observed in the layer printed at 60 ºC (Figure 3.3e), suggesting that such high temperature does not lead to suitable blend morphology in this case study. Thus, the

optimal temperature for this system seems to be located between 50 ºC and 55 ºC. AFM measurements were performed on these two samples in order to analyse which printing temperature leads to smoother topology (**Figure 3.4**).
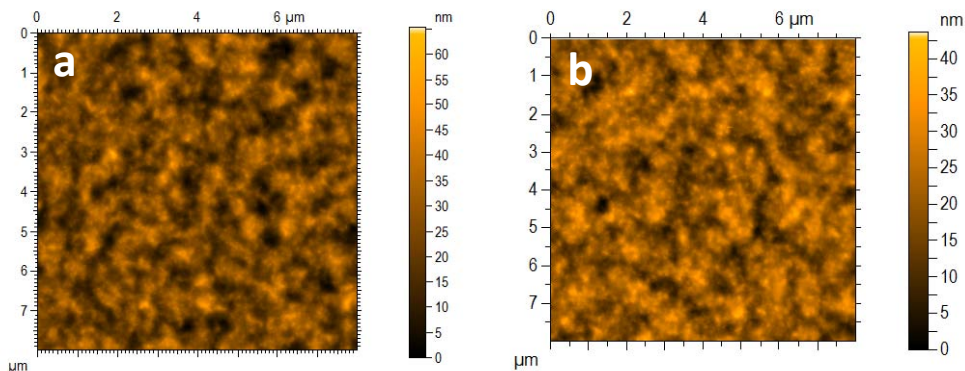
Figure 3.4. Tapping mode AFM surface scans (8 x 8 μm) of P3HT:PCBM inkjet printed layers with the substrate temperature set at a) 50 ºC (RMS = 8.1 nm) and b) 55 ºC (RMS = 5.6 nm).

The results reveal lower roughness for the layer printed at 55 ºC. Despite leading to acceptable layer roughness for OPV fabrication, the solvent mixture used (THN:mesitylene, 9:1) results in a deficient macroscopic homogeneity (there is still coffee ring). The low vapour pressure of THN is responsible for too long drying, even at high temperatures. For this reason, the proportion of the more volatile solvent, mesitylene, was increased for the following experiment.

Drop spacing

The spacing between the neighbouring drops is one of the key parameters to modify the thickness of the printed layer.[86] Intuitively, this also determines how long the drying of the layer will take. The lower the drop spacing is, the higher is the density of drops, thus the thicker is the resulting wet film and the longer will take the complete drying of the film (this was seen also in previous section).

For the study of this parameter, 4 different layers were fabricated at 25 μm, 30 μm, 35 μm and 40 μm drop space. In this case, only 1 jet was used to print the P3HT:PCBM (1:1) 2% wt. blended in THN:mesitylene (7:3) on top of PEDOT:PSS layers. The temperature of the substrate was kept constant at 50 ºC. The standard recipe was followed for the rest of parameters (see chapter 2). The results of this set of samples are depicted in **Figure 3.5**.
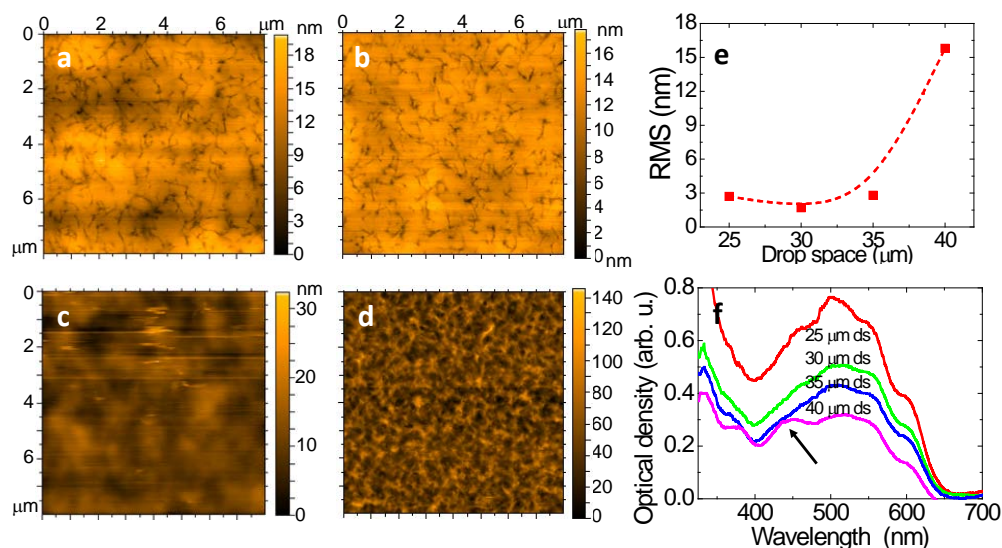
Figure 3.5. Tapping mode AFM surface scans (8 x 8 μm) of P3HT:PCBM inkjet printed layers with a drop spacing of a) 25 μm (RMS = 2.7 nm), b) 30 μm (RMS = 1.7 nm), c) 35 μm (RMS = 2.8 nm) and d) 40 μm (RMS = 15.8 nm). e) Correlation between RMS and drop space resulting from measurements a-d. f) Absorption spectra of these 4 layers. The black arrow indicates the signal of amorphous P3HT.

It is clearly visible how big the impact of the drop spacing can be in the roughness of the layers. While smooth surfaces are obtained at 25, 30 and 35 μm of drop space, the roughness is increased by a factor of 7 at 40 μm of drop space. Additionally, absorption measurements were performed to detect possible changes in the blend films as a consequence of different drying times (Figure 3.5f). The spectra reveal two important characteristics. First, the signal gets weaker with higher drop spacing. According to Beer-Lambert law, lower absorption is related to shorter optical path (in this case, thinner film). As mentioned above, these changes in the thickness of the layers are a consequence of the variation in the density of drops due to different drop spacing. Secondly, the absorption spectrum at 40 μm of drop spacing reveals the appearance of a new feature at around 450 nm. According to the literature, this new peak is believed to correspond to amorphous P3HT.[87] The explanation for this drives us back to the drying kinetics in the following sense. With larger drop spacing the wet film dries much faster and the P3HT chains may not have enough time to reorganise to form crystals, hence bigger domains of amorphous P3HT are expected (i.e. higher signal at the 450 nm peak).

Number of jets

The number of jets used during the printing can also play an important role. Although the desired scenario for a fast, high throughput coating would involve as many jets as possible, some precautions have to be taken into account to prevent undesired effects such as coffee ring and inhomogeneities on the layer.

Depending mainly on the ink formulation, the coffee stain effect can be avoided by reducing the number of printing jets, especially when printing small patterns. This is demonstrated in the following case. Two different layers were printed with 1 and 5 simultaneous jets, respectively. The same ink as in the previous section was used in this case, as well as the same recipe except from the substrate temperature (40 ºC) and the drop spacing (35 μm). Notable differences between both layers are visible in **Figure 3.6**.
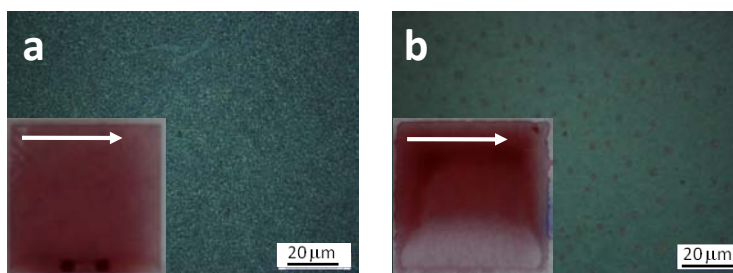
Figure 3.6. Optical microscopy images of P3HT:PCBM layers (2 x 2 mm) inkjet printed with a) 1 jet b) 5 jets. Macroscopic images are depicted in the insets. White arrows indicate the printing direction.

Almost no coffee stain is observed when printing with 1 jet and higher homogeneity is also obtained. In this case, the use of 1 jet in such small pattern prevents the creation of a big drop due to lower accumulation of the printed lines during the coating process. On the contrary, a big accumulation of liquid occurs with 5 jets: the first 5 printed lines are still wet when the print head returns back to the left part of the pattern to print the following 5 lines. As a consequence of this liquid accumulation, a big coffee stain is observed in this layer. Moreover, different lateral phase separation is observed as well: larger aggregates or clusters are visible in Figure 3.6b. The too long drying time in the second case may promote such segregation between P3HT and PCBM.

Pattern

Finally, a fine tuning to optimize the morphology of a printed layer can be performed by an adequate design of the printing pattern. Of special importance are the size and shape of the printed pattern.[88] In the case of active layers, an adequate patterning can also help to enhance the photovoltaic charge extraction due to optimal morphology resulting from a proper drying. On the other hand, a suitable pattern should assist the formation of homogeneous films.

Here, an approach for pattern optimisation is proposed. In the first step, a specific pattern was printed. The pattern consists of a 20 x 20 mm square connected to a straight line that starts 200 mm far from the square at the same height and ends to the right down corner of the square (**Figure 3.7**). At the beginning, the print head is obliged to move a long distance far from the printed line before coming back to print the second line. At that moment the first line is already dried (i.e. short drying time). Progressively, this distance is reduced and thus accumulation of liquid may occur at some point (i.e. longer drying time). As a result, a sort of gradient of drying time is obtained.
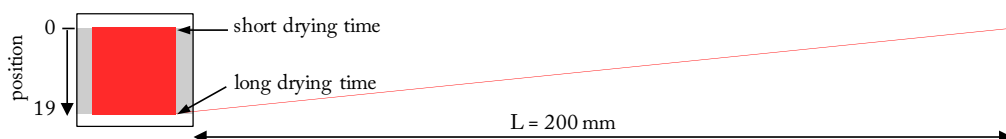
Figure 3.7. Pattern (red coloured) used in this study. The grey area corresponds to the ITO patterned layer of the device. The PEDOT:PSS layer between the ITO and the active layer is not shown.

The active layer was deposited on top of spin coated PEDOT:PSS by printing a P3HT:PCBM (1:1) 20 mg/mL solution in DCB:mesitylene (68:32) using 1 jet, with the standard recipe for inkjet printing this material system. The OPV device was completed by evaporating long top contacts on the 90º shifted sample. The latter was done in order to overlap the gradient with the long side of the contacts (**Figure 3.8**). It is important to note that no thermal annealing was performed to the active layer in order to better study the effect of the drying time.
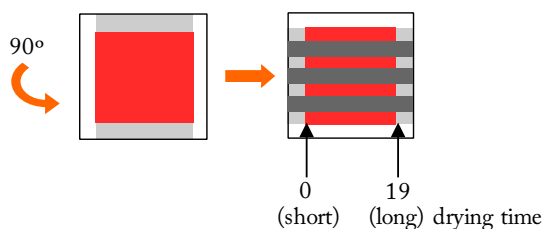
Figure 3.8. Once printed, the sample is shifted 90° and the long Al cathodes (darker rectangles) are thermally evaporated on top of the organic layer.

The second step consisted of measuring the EQE spectra at different positions along the contact (this is, at different positions along the gradient). Using this data, the correlation between drying time and charge extraction efficiency can be analysed. More in detail, EQE spectra were collected at 20 equidistant points from 0 position to 19 mm (as indicated in Figure 3.8). The whole data collection was performed sequentially by using a motorised translation stage and a home-made software tool.

The results shown in **Figure 3.9** suggest that P3HT crystals, identified through the characteristic shoulder at 600 nm in the EQE spectra, are present since the beginning of the printing process (position 0-1) and grow until they reach a maximum EQE value slightly above 40% at position 3 mm. From there onwards no further crystallisation is observed, as it is deduced from Figure 3.9b. However, further information about morphology evolution upon increasing drying time can be extracted from the data presented in Figure 3.9c. The crystalline contribution of P3HT (600 nm / 375 nm ratio) grows rapidly with the lateral position, that is with increasing drying time. On the other hand, the amorphous contribution of P3HT (related to the signal at 460 nm) is reduced with increasing drying time, as seen in both (460 nm / 545 nm and 460 / 600 nm ratios). The latter means that P3HT chains achieve a higher organisation at longer drying times.
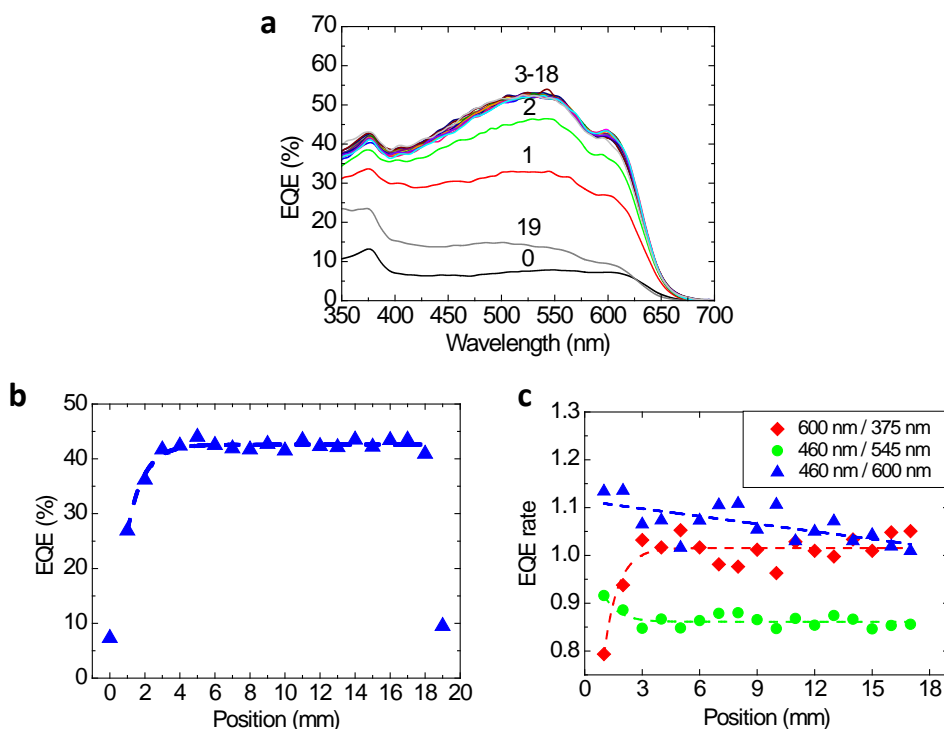
Figure 3.9. a) EQE spectra collected with the light spot located at different points from position 0 to 19, according to Figure 3.8. b) EQE at 600 nm correlated to the position. c) Rates between EQE at significant wavelengths: 600 nm (crystalline P3HT), 545 nm (maximum P3HT absorption), 460 nm (amorphous P3HT) and 375 nm (PCBM main peak). The exponential fits depicted as dashed lines evidence the rise of the crystalline (600 nm) or ordered (545 nm) P3HT contribution. Extreme points 0 and 19 were not considered in the fitting.

According to the results, suitable blend morphology is achieved from position 3 to 18. However, macroscopic inhomogeneities may appear when there is high liquid accumulation during printing, which happened in this case at positions above 12 mm. Therefore, the optimum pattern for this system should achieve a compromise between enough drying time to enable good morphology formation and short drying time to obtain homogeneous films. According to these results, the printing pattern for P3HT:PCBM layers included a vertical line separated 40 mm away from the sample (see **Figure 3.10**) in order to accomplish the proper drying time.
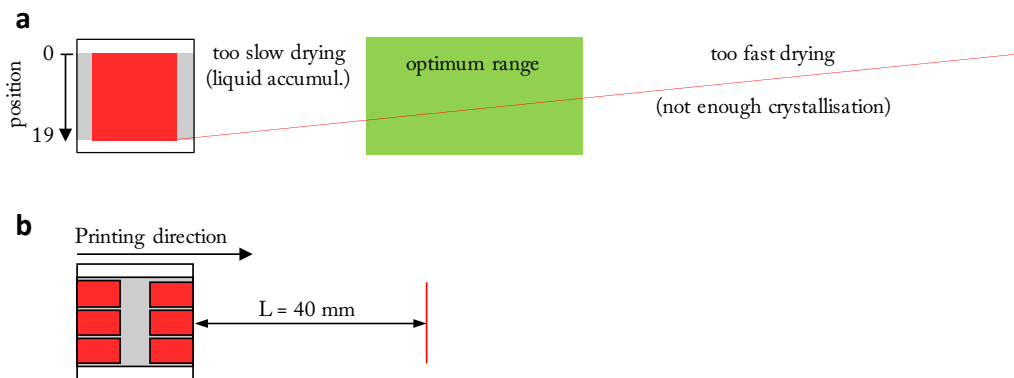
Figure 3.10. a) The three different regimes identified in the printed pattern in relation to the drying time. b) Optimised inkjet printing pattern (red coloured) for P3HT:PCBM based OPV devices.

3.1.4. Overcoming S-shape: LiF vs. thermal annealing

The current-voltage characteristic of organic bulk heterojunction solar cells may reveal an S-shaped deformation. The occurrence of a new counter diode gives as a result an inflexion point in the J-V curve.[89–91] The origin of this second diode is still a matter of discussion.[92] Some of the explanations include a decrease in charge transfer rate over the interface,[89] surface recombination[90,91] or interface dipoles as responsible for a decrease in V_{oc} and leading to double diodes.[93] Nevertheless, all the theories agree that the interface between the cathode and the active layer may be the origin of this limiting factor for efficiency and fill factor of OPV devices. A good quality of that interface is therefore essential.[94]

Reported solutions to prevent or revert this negative feature encompass thermal annealing,[95] photo-annealing,[96] the incorporation of buffer layers like LiF[25,31] or bathocuproine[97] and faster evaporation rate of Al.[51] In this section we present the comparison between the effects of post-thermal annealing and the incorporation of LiF in the performance of our OPVs.

Thermal annealing after Al evaporation

The standard procedure described in chapter 2 (active layer processed by inkjet printing) was followed to fabricate OPV devices except from the thermal evaporation step, which did not include LiF in this case. The presence of the S-shape is clearly visible in the J-V characteristics presented in **Figure 3.11**. In accordance to literature, this effect is only visible under illumination.
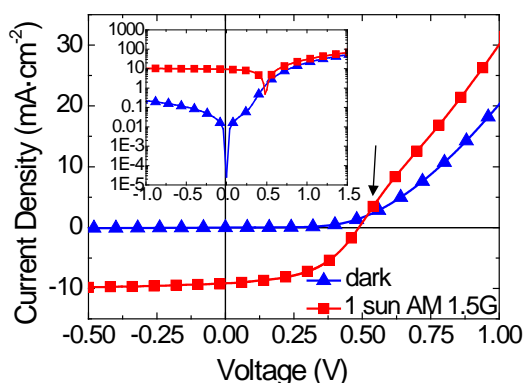
Figure 3.11. J-V characteristics of an OPV device without LiF and with no post-processing treatment. The appearance of the S-shape (black arrow points the kink) is evident under illumination and leads to a mismatch with the dark current above the V_{oc}.

After the J-V characterization, a second thermal annealing step was performed (10 min at 140 ºC). The latter led to a simultaneous increase of V_{oc} (from 0.48 to 0.59 V), FF (from 50 to 51%) and PCE (from 2.20% to 2.65%), while J_{sc} decreased from 9.14 mA·cm^{-2} to 8.80 mA·cm^{-2} (see **Figure 3.12** and **Table 3.3**). According to literature, the responsible for this improvement in the overall efficiency is supposed to be the better quality of the cathode-organic layer interface, induced by Al percolation into the active layer as a result of the thermal annealing.[95] Moreover, this enhancement of the contact between these two layers also reduces the number of traps, which are responsible for a change in the electric field distribution inside the device and screening the electric field at the interface,[95] thus resulting on the observed S-shape.
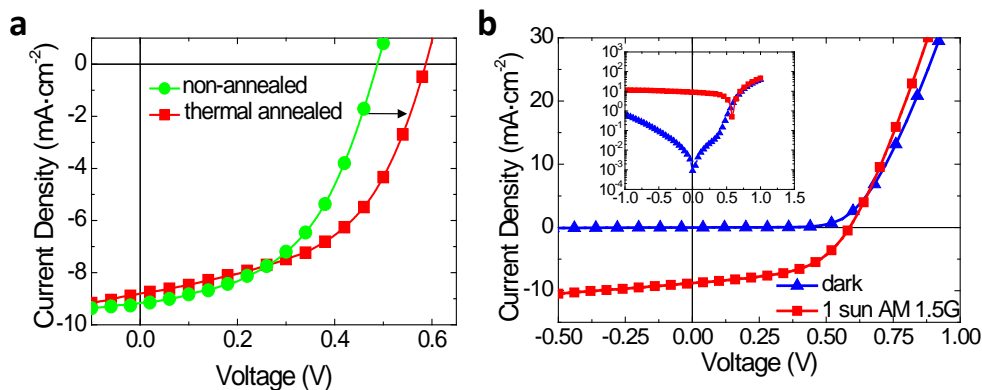
Figure 3.12. a) The improvement of photovoltaic performance between non-annealed and thermal annealed samples after Al evaporation is demonstrated. b) J-V characteristics in dark conditions and under AM 1.5G illumination, 100 mW·cm^{-2} of the post-annealed sample.

A better rectification of the J-V curve is observed in post-annealed samples, especially under dark conditions, where a more defined diode shape is seen in the logarithmic plot (Figure 3.12b). Additionally, the mismatch between dark and light J-V curves at voltages above the V_{oc} is dramatically reduced.

LiF as a cathode interlayer

OPV devices including a 1 nm LiF interlayer were fabricated following the standard recipe detailed in chapter 2. For a better study of the independent effect of the presence of LiF, some samples were fabricated by inkjet printing both PEDOT:PSS and P3HT:PCBM layers whereas some extra samples were done by spin coating the PEDOT:PSS and inkjet printing the active layer. The results are shown in **Figure 3.13** and Table 3.3.
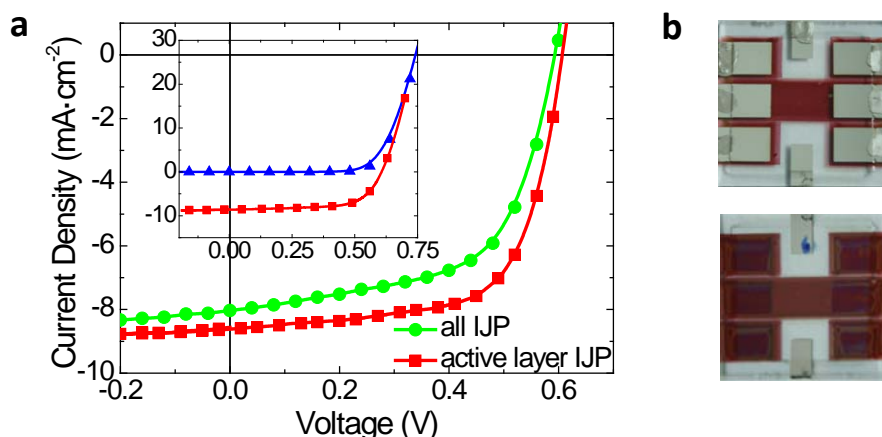
Figure 3.13. a) J-V characteristics of devices with LiF as a cathode interlayer. The plot compares one device with the active layer made by inkjet printing against another one with both PEDOT:PSS and active layer inkjet printed. The inset shows the good rectification of the former device in dark (blue triangles) and light (red squares) conditions. b) photographs of the all inkjet printed device from front (top) and back (down) view. Each single solar cell has an active area of 25 mm^2.

In both devices a higher PCE (2.85% and 3.54% for all inkjet printed and spin coated + inkjet printed samples, respectively) is obtained in comparison to post-annealed samples (2.65%). As seen in Table 3.3, the main improvement lies in FF and the concomitant better rectification in the J-V curves. The latter is also evident in the lower series and higher parallel resistances. Therefore, it can be deduced that the LiF interlayer enables a more selective charge collection due to its hole blocking function.

Table 3.3. Comparative OPV results of samples with different solutions to overcome S-shape. In all cases the P3HT:PCBM active layer was deposited by inkjet printing.

	V_{oc} (V)	J_{sc} (mA·cm^{-2})	FF (%)	R_s (Ω·cm^{-2})	R_p (Ω·cm^{-2})	PCE (%)
without LiF						
no further annealing	0.48	9.14	50	16	345	2.20
thermal annealing after Al	0.59	8.80	51	15	311	2.65
with LiF						
PEDOT:PSS by IJP	0.59	8.04	60	10	465	2.85
PEDOT:PSS by SC	0.61	8.62	67	8	1105	3.54

Similarly, as a hole-transporting layer, the PEDOT:PSS also affects the FF. Given that the same PEDOT:PSS ink was used and that the thickness of that layer was

kept constant in all the cases, the variations in FF observed between the two samples containing LiF can be attributed to a different morphology of the PEDOT:PSS layer. As it is shown below, PEDOT:PSS layers resulted to be slightly smoother when processed by spin coating. Still, the 2.85% efficiency of the all inkjet printed device as well as the 3.54% of the inkjet printed active layer device are comparable to the state of the art values.[71,75]

A deeper analysis of the dark J-V curve may give further insights into the origin of the lowering of the FF in the fully inkjet printed device. **Figure 3.14** shows a semilogarithmic plot of the dark current density-voltage of the solar cell devices under study for the opening of the diode voltage range (that is, where the current flow is increased at forward bias).
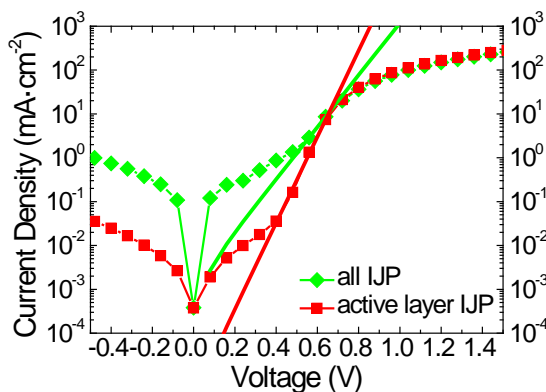
Figure 3.14. Dark J-V characteristics of the devices shown in Figure 3.13. The thicker lines correspond to the linear fits of the diode governing region.

The slope of the log-linear dark J-V curve between 0.4 V and 0.7 V represents the diode behaviour of the solar cells as governed by the diode ideality factor (n) and saturation current (J_0).[98] J_0 corresponds to the intercept of the slope at 0 V and the ideality factor can be deduced, in a simplified model, from

$$J = J_0 \left(e^{-\frac{qV}{nkT}} - 1 \right)$$ [3.1]

The low parallel resistance of the all inkjet printed device (465 $\Omega \cdot cm^{-2}$) is limiting the opening of the diode at low voltages. As a consequence of this, a high saturation current (1.4$\cdot$10^{-3} mA$\cdot$cm^{-2}) and a misleading ideality factor (2.74) are obtained.

According to literature, n values larger than 2 indicate complex carrier recombination mechanisms.[98]

In contrast, the device with only the active layer made by inkjet printing shows a lower saturation current ($3.9 \cdot 10^{-6}$ mA·cm^{-2}) and an ideality factor of 1.72, which is in the optimal range for best photovoltaic performance. It has been shown that for bulk heterojunction solar cells, the ideality factor correlates with the number of distributed interfaces within the blend, while the saturation current is related with the quality of the interfaces.[98] As said above, considering that the processing of the bulk heterojunction layer was identical, the differences in saturation current and ideality factor between both samples have to be related to the PEDOT:PSS layer or the effect of differences in this layer on the active layer. The better rectification of the J-V curve (i.e. higher FF, R_p and lower R_s) is the result of an improved selectivity of charge collection. The smoother and more homogeneous surface of the PEDOT:PSS layer obtained by spin coating is responsible for that (see **Figure 3.15**).
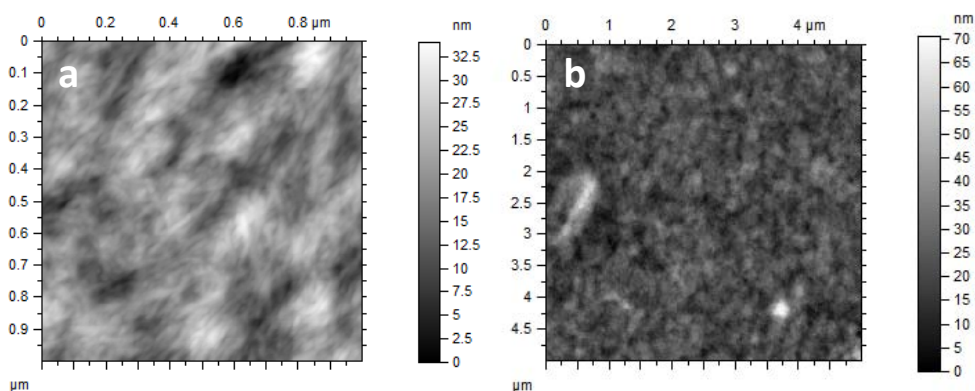
Figure 3.15. AFM images of PEDOT:PSS layers processed by a) spin coating (RMS = 4.7 nm) and b) inkjet printing (RMS = 6.4 nm).

As deduced from AFM images, the interface between PEDOT:PSS and the blend layer is better when the former is processed by spin coating, thus leading to a higher performance of the OPV device. On the other hand, the small defects observed in inkjet printed PEDOT:PSS layers may be limiting the hole mobility and/or increasing the probability of surface recombination in the fully inkjet printed device. This could partially explain the losses in J_{sc} and FF, respectively.

3.2. SPIN COATING, DOCTOR BLADING AND INKJET PRINTING. COMPARISON BETWEEN COATING TECHNIQUES

Mainly three different deposition techniques have been used for the processing of both PEDOT:PSS and active layers throughout this thesis: spin coating (SC), doctor blading (DB) and inkjet printing (IJP). Although these three lab scale methods are suitable for fundamental studies, especially the first two are more frequently reported in the current literature.

The aim of this section is to present a qualitative comparison between each one, based on the personal experience acquired along this PhD thesis, and then present evidence in a real case scenario.

3.2.1. A step by step comparison

In order to give a general overview of the strengths and weaknesses for each coating tool, relevant parameters and properties common to all of them are compared below.

Speed and drying time

Fast and high throughput coating processes are not mandatory for lab scale research. However, speed may be appreciated especially when time-consuming experiments such as optimisation of the coating process or combinatorial studies are intended.

Related to the speed, another important parameter is the drying time of the wet film. The latter can be modified in both DB and IJP by increasing the temperature of the substrate, whereas this can't be done in SC without changing the solvent (higher volatility reduces the drying time) or the spinning speed (which will affect the film thickness). The spreading of the ink on the substrate is faster in SC (less than 2 seconds) but the complete process (i.e. including drying time) is faster for DB (10-20 seconds). The spinning time in SC is normally extended from 1 to 3 min to obtain a good drying. On the other hand, IJP process (both coating and drying) is much slower in lab scale machineries. For instance, more than 5 min were normally needed to inkjet print the P3HT:PCBM layer for a 6 pin OPV device with the Dimatix 2831 (the area of the pattern shown in Figure 3.10b is about 500 mm^2).

Material saving

This is a crucial factor for low-cost processes, even at lab scale, taking into account the high prices of semiconductor materials. In this context, the most efficient technique is IJP due to its drop-on-demand character. On the contrary, larger amount of material is wasted in DB (remaining ink on the blade after coating) and more markedly in SC (>90% of the ink is ejected during substrate rotation).

Patterning

In alignment to the waste of material, another valued feature in coating processes is the possibility of patterning the material. No doubt about it, IJP is in clear advantage against the other two, since software controlled patterning is enabled. Neither DB nor SC has the possibility to pattern during coating.

Film thickness optimisation

A good control of the film thickness is required for the optimisation of OPVs. One independent way to tune the final thickness of the film is to adjust the solid content of the ink. Nonetheless, the preparation of multiple inks for optimisation purposes can be a tedious work. Thus, an easy and fast tuning of the thickness through the coating technique itself facilitates the optimisation process. In this sense, both SC and DB permit to easily obtain almost differential variations in film thickness by changing the spinning and blade speeds, respectively. Meanwhile, the parameters that determine the film thickness in IJP, mainly the drop spacing, require more efforts to maintain other important characteristics unvaried like film homogeneity.

Handling and ease of optimisation

Both SC and DB are easy tools to deposit layers from solutions, since only few coating parameters have to be set. In contrast, there are a lot of parameters to be adjusted in IJP. This complexity can be interesting to perform a fine tuning in the optimisation process, but it is a clear disadvantage when new materials or inks want to be tested.

Reproducibility

Similarly, the ease of handling has a direct impact in the reproducibility. The latter is crucial for an efficient research in the wide OPV scientific community. It is for this reason that SC and DB are the most commonly used tools in lab scale research. To

reproduce reported results in IJP greater efforts are usually required, mainly due to the lack of detailed description of coating conditions.

Ink limitations

Appropriate rheological properties of the coating solutions are vital for a good wetting, which results in a good film formation. In particular, the surface tension of the ink and the surface free energy of the substrate (and thus the contact angle when the liquid is deposited on top of the substrate) are the parameters that rule the wetting behaviour. This requirement is common to any coating process. Besides this, further ink limitations are related to IJP, like viscosity and vapour pressure of the solvents, which have to be taken into account in order to prevent nozzle clogging. Both SC and DB are more robust in this sense.

Area

Another key point in the research of OPVs is the active area of the devices. Although the three deposition techniques in study are used as testing workbench for lab scale, DB and IJP offer the possibility to move a step further into a mid-scale step. Moreover, the use of high throughput inkjet printing machineries has been recently demonstrated in the field of OPVs.[79]

R2R compatibility

Definitely this is a hot spot in the assessment of the possibilities to transfer the knowledge from lab scale to large-scale roll-to-roll processes. SC is in clear disadvantage in this context, since there is no chance to make this process with continuous substrates. On the other hand, the R2R *brother* of DB is the knife coater, thus virtually a direct transfer can be done. The working principle of more extendedly used slot die coating is similar too. Better yet, IJP can be directly attached to R2R machinery.

Cost

Finally, an unavoidable parameter to fairly compare any coating machinery is the price. Basic spin coaters and doctor blade equipments are in the same order of magnitude, while the cost for an inkjet printer may be 5 times higher.

In order to better compare in a visual way all the features described above, a summary is presented in **Figure 3.16**. Note that this is only a qualitative comparison.
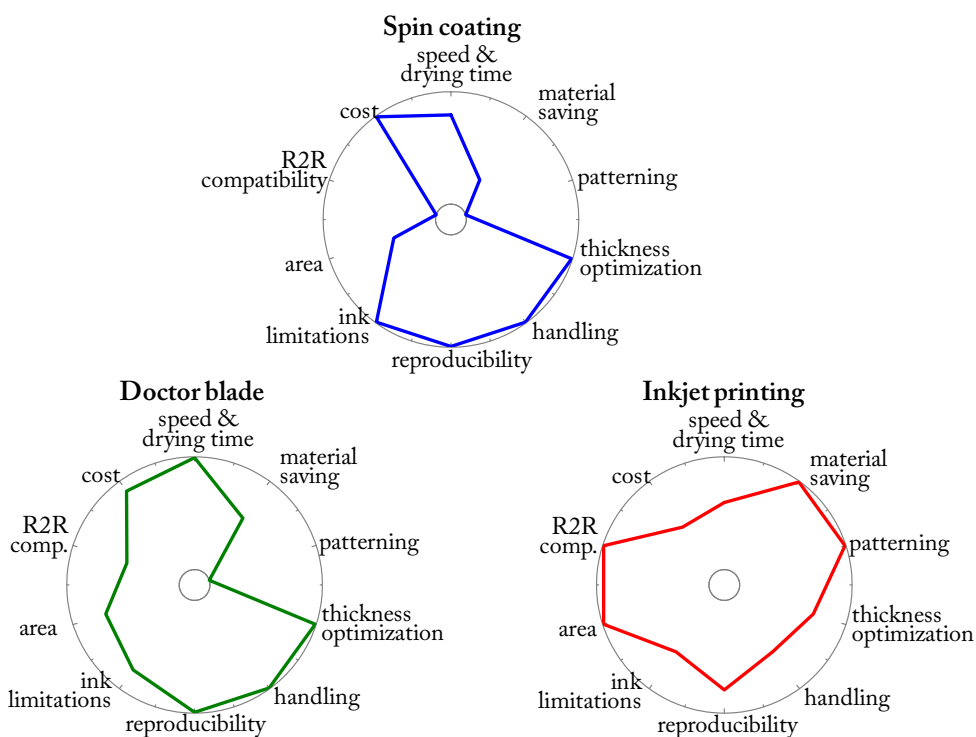
Figure 3.16. Qualitative comparison of the most relevant features between spin coating, doctor blading and inkjet printing, relative to each other. The outer (inner) grey circles mark the relative maxima (minima).

According to these plots, it could be well said that none of these techniques is definitely better than the others. Every single coating process has its particular advantages. It is therefore not surprising that all of them are still in use in the fabrication process of OPVs.

3.2.2. A real comparison: P3HT:PCBM based solar cells

Finally, to conclude this section, the results obtained with optimised processing of the P3HT:PCBM layers made by spin coating, doctor blading and inkjet printing, according to the recipes described in the second chapter, are presented. More in detail, a comparison of the J-V characteristics and the performing parameters of the corresponding optimised OPV devices are shown in **Figure 3.17** and **Table 3.4**, respectively.
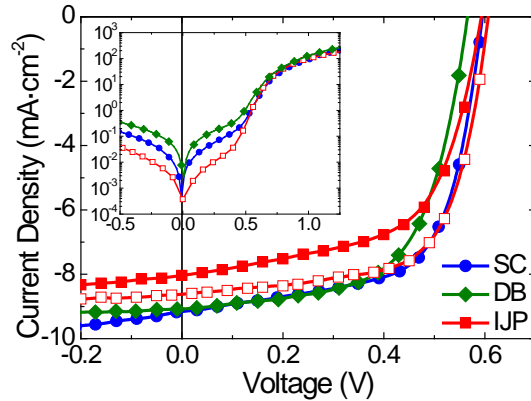
Figure 3.17. J-V electrical characterization of OPV devices under AM 1.5G illumination, 100 mW·cm⁻², with both PEDOT:PSS and P3HT:PCBM layers (filled symbols) or only the active layer (empty symbols) processed by spin coating (SC, circles), doctor blading (DB, diamonds) and inkjet printing (IJP, squares). The inset shows the response in dark conditions in logarithmic scale.

Table 3.4. OPV parameters of the best performing devices based on P3HT:PCBM active layer.

processing technique		V_{oc}	J_{sc}	FF	R_s	R_p	PCE
PEDOT:PSS	P3HT:PCBM*	(V)	(mA·cm⁻²)	(%)	(Ω·cm⁻²)	(Ω·cm⁻²)	(%)
SC	SC [a]	0.59	9.17	65	7	502	3.52
DB	DB [b]	0.57	9.08	62	9	1283	3.21
IJP	IJP [c]	0.59	8.04	60	10	465	2.85
SC	IJP [c]	0.61	8.62	67	8	1105	3.54

*Processed from solutions based on [a] CB, [b] DCB, [c] DCB:mesitylene (68:32)

The J-V curves of the devices prepared by inkjet printing after the optimisation process described in section 3.1.4 are overlapped with fully doctor bladed and fully spin coated devices (referring to PEDOT:PSS and P3HT:PCBM layers). A clear decrease tendency is observed in the PCE when moving from spin coating (3.52%) to doctor blade (3.21%) and to inkjet printing (2.85%). This decrease is due to the worsening of the fill factor and series resistance. A noticeable drop in J_{sc} is visible as well from doctor bladed to inkjet printed devices. One could ascribe this to a worse active layer morphology, due to the slower drying time linked to inkjet printing. The results of the combined spin coated PEDOT:PSS and inkjet printed active layer device suggest, however, a different explanation for this. All the performance parameters are significantly enhanced, resulting in a PCE of 3.54%, which is moreover in the same order as the fully spin coated device. As demonstrated in section 3.1.4, this

improvement in PCE is due to a better morphology of the PEDOT:PSS layer obtained by spin coating in contrast to inkjet printing, rather than to changes in the active layer.

In summary, it can be concluded that a careful optimisation process is needed for every single layer and that, even so, using one unique coating method for processing all the layers might not be the best choice. Instead, a suitable combination of techniques may be advantageous.

3.3. VAPOUR PRINTING AS AN ALTERNATIVE POST-PROCESSING TREATMENT

In order to achieve an optimal nanomorphology of the blend in the active layer for maximum OPV performance, different processing and post-processing treatments have been developed in recent years. These include thermal annealing,[99] slow drying,[100,101] solvent annealing[102] and the use of additives.[39] Most of these techniques are time-dependent, usually taking several minutes of annealing to reach the optimal morphology. A faster annealing treatment would thus be of interest.

Our group has recently reported an alternative process that we called vapour printing,[103] which may offer a solution for high throughput annealing of polymer solar cell active layers. It presents some advantages when compared to conventional annealing techniques, such as easy processing and reduced cost and solvent-consumption. Commercially relevant devices such as those based on flexible substrates and multilayered structures may suffer from thermal stresses during thermal annealing, which may result in delamination or loss of registration during the fabrication process. These features are minimized with this technique. Vapour printing also allows working under ambient conditions and offers a straightforward, spatial resolved patterning. This last property is of special interest in thin film based optoelectronic devices. In the case of organic photovoltaics it might be beneficial for a better module operation by reducing crosstalk between cells. Selective patterning of the individual cells would create well defined areas with high charge mobility under each cell surrounded by low transport film between cells. Photogenerated charges would then be confined within them, thus avoiding undesirable charge transport pathways between neighbouring cells.

The emphasis here was put on extending this novel annealing treatment into the field of OPVs. P3HT and PCBM based OPVs are treated at different vapour printing annealing times. The relationship between annealing time and optoelectronic performance of these devices is presented and discussed in terms of vapour induced morphological evolution. Additionally, solvents with different vapour pressure were employed. The results herein presented support the use of this alternative post-processing technique, also with appropriate, non-chlorinated solvents.

3.3.1. Description of the method

Vapour printing was performed on top of the organic layers as follows. A nitrogen flux (1 L·min^{-1} at 1 bar) was injected into a solvent filled gas washing bottle and the bubbling was left during 30 s to reach gas solvent saturation. The solvent carrier gas was delivered through a nozzle on top of the active layer (1-2 mm separated), which was located on top of an X-Y translation stage for patterning purposes. By modifying the speed of the motorized-translation stage, the organic layer was annealed during different times, ranging from 0 – as cast– to 40 s. The working principle of the vapour annealing apparatus is shown in **Figure 3.18**.
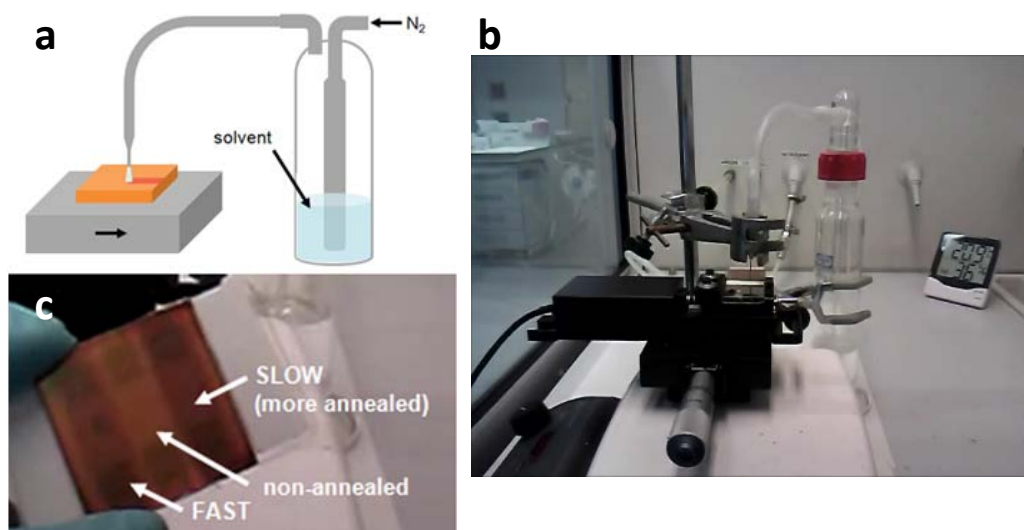
Figure 3.18. a) Schematic representation and b) picture of the vapour printing apparatus used in this work. The nitrogen flux bubbles into the solvent and solvent vapour is delivered through a needle on top of the moving sample. c) Image of the resulting sample after faster (left) and slower (right) annealing. The change in coloration is evident with respect to the middle, non-annealed region.

3.3.2. Proof of concept

In order to study the direct effect of vapour printing on the OPV performance, solar cell devices were prepared by spin coating as described in chapter 2. After spin coating the P3HT:PCBM active layer and instead of thermal annealing, vapour printing was performed in air conditions before evaporation of Al electrodes.

Figure 3.19 displays current density-voltage curves of as cast, the best performing CB vapour printed and a thermally annealed OPV device under 1 sun illumination. The main device parameters are summarized in **Table 3.5**. To better distinguish the vapour annealing contribution, no further annealing was performed after top-electrode evaporation. The latter is known to be beneficial to improve the performance of solar cell, especially the fill factor, as it is demonstrated in section 3.1.4. This partially explains the low power conversion efficiencies of our devices compared to other works using equivalent materials and structure.
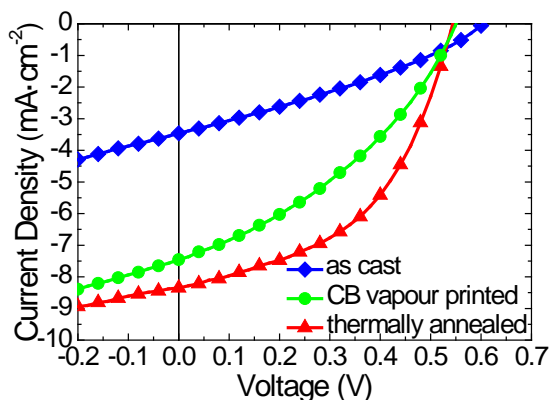
Figure 3.19. J-V characteristics of the as cast, vapour printed using chlorobenzene solvent and thermally annealed solar cells based on P3HT:PCBM active layers.

Table 3.5. Photovoltaic performance of the devices with different annealing treatments

Annealing treatment	V_{oc} (V)	J_{sc} (mA·cm^{-2})	FF (%)	R_s (Ω·cm^{-2})	R_p (Ω·cm^{-2})	PCE (%)
As cast	0.60	3.46	32	75	235	0.67
CB vapour printing	0.56	7.45	36	26	197	1.52
Thermal annealing	0.54	8.36	49	17	405	2.21

Figure 3.19 and Table 3.5 clearly show that vapour printing improves the performance of solar cell with respect to the as cast sample. In particular the short-circuit current (J_{sc}) is increased by a factor greater than 2, suggesting that free charge generation, transport and/or collection are improved. This is due to an enhancement of the P3HT crystallisation,[100] leading to a slight phase separation of the P3HT:PCBM blend[104] (see below). On the other hand, the V_{oc} is slightly reduced for vapour printed devices compared to those as cast. This typically happens when P3HT crystallises and its HOMO level is increased, thus reducing the energy gap with the LUMO level of the PCBM.[105]

3.3.3. Induced P3HT crystallisation

To study the changes in blend morphology, the devices were characterized by means of different spectroscopic techniques. UV-Vis spectrophotometry, photoluminescence (PL) and Raman scattering were measured in samples annealed at different vapour printing times (**Figure 3.20**). In the UV-Vis spectra a red shift is observed for the vapour printed sample with respect to the as-cast around the P3HT absorption range.

Furthermore, the shoulder at 600 nm, a signature of crystallised P3HT,[58] is markedly more pronounced in the vapour printed sample. In agreement with this hypothesis, PL quenching is reduced by a factor of 9 as the film is vapour printed, as it can be seen in Figure 3.20b. In the as cast sample, P3HT and PCBM are highly intermixed, and hence, the photogenerated excitons in P3HT domains easily find an interface with PCBM, where the charge transfer (CT) may take place, leading to the CT state and quenching the polymer PL. With bigger P3HT crystals, the probability that photogenerated excitons recombine radiatively before reaching the PCBM interface increases. This is also observed upon thermal annealing.[106]
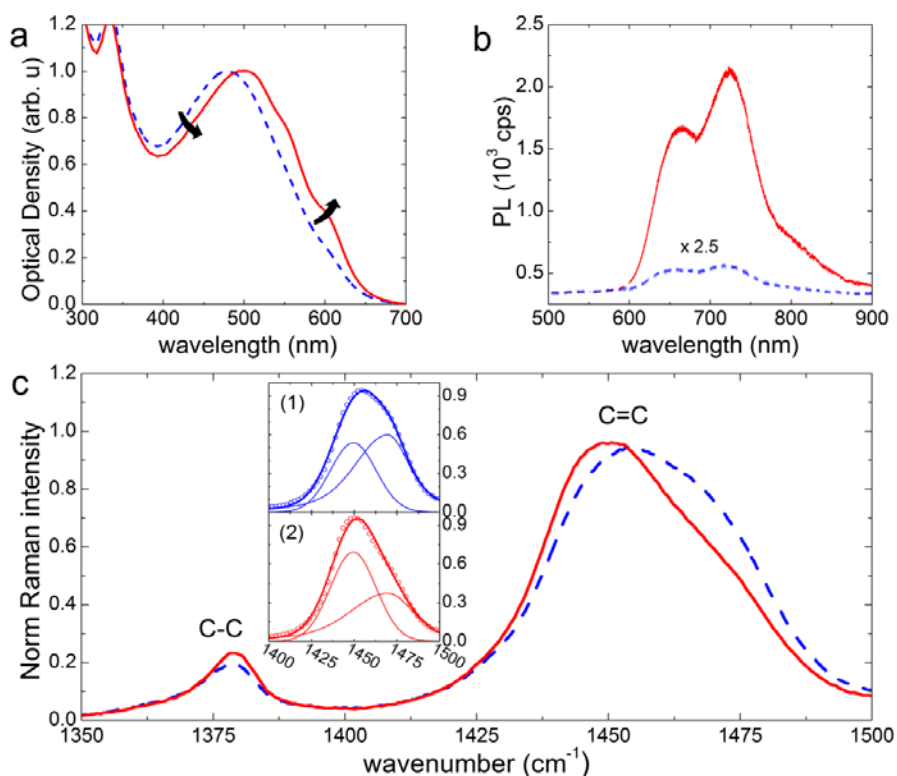
Figure 3.20. a) UV-Vis spectrophotometry, b) photoluminescence and c) Raman spectra of the as cast device (blue dashed line) and the CB vapour printed (red solid line). The black arrows in a) indicate the decrease in amorphous P3HT amount and concomitant increase in crystallinity at 600 nm. The PL spectra of the as cast sample is multiplied by a factor of 2.5 to make it more visible. The inset in c) shows the Raman experimental data (empty symbols) overlapped with the fit (thick lines) resulting from the contribution peaks (thinner lines) corresponding to ordered (~1449 cm^{-1}) and disordered P3HT (~1470 cm^{-1}) for 1) as cast and 2) vapour printed samples.

Raman spectra measured under resonant conditions (488 nm excitation) are also in accordance to the already described features. As Figure 3.20c shows, three significant

changes can be observed in the main in-plane ring skeleton Raman modes characteristics upon annealing: (a) a large shift to lower wavenumber in the C=C mode peak position (~1449 cm^{-1}); (b) a narrowing of the C=C mode, and (c) a larger intensity of the C-C mode with respect to the C=C mode (~1380 cm^{-1}). Tsoi *et al.* observed the same behaviour of the Raman modes in thermal annealed P3HT:PCBM layers, which was attributed to a higher degree of P3HT crystallinity upon annealing.[60] The experimental data of regioregular and regiorandom P3HT therein described is used in the present work to fit the contribution peaks of the more ordered (~1449 cm^{-1}) and disordered (~1470 cm^{-1}) P3HT domains, respectively (Figure 3.20c inset). Reassuringly, a higher degree of molecular order of the P3HT chains is observed upon vapour printing. Compared with thermal annealed samples, a higher contribution of the disordered P3HT is, however still observed at long vapour printing times. This suggests a different upper limit in polymer crystallinity for CB-based vapour printing compared to thermal annealing, which may partially explain the lower FF observed in the vapour printed samples compared to those thermally annealed.

3.3.4. Changes in the morphology of P3HT:PCBM layer with exposed time to vapour printing[A]

All the results above suggest that vapour printing promotes polymer crystallisation. To understand in more detail the effect of vapour printing on the organic layer and thus on the performance of the device, parameters of solar cell, PL, optical density (OD), and Raman spectra were monitored for devices exposed during different vapour-printing times. The ratio between P3HT 0-0 and 0-1 transition energy in UV–Vis spectra (i.e., OD) gives information about the degree of P3HT crystallisation.[59] Similarly, the ratio between ordered and disordered P3HT signatures in the Raman spectra also provides insights into crystallisation. A summary of the most relevant results are depicted in **Figure 3.21**, where well-defined tendencies are observed. The process of vapour printing starts by producing fast and drastic changes in all measured properties in a short time-scale. After that, a plateau is observed, followed by a final step where some properties remain almost constant (OD, PL, and Raman), whereas others change in the opposite direction and less pronouncedly compared with the initial step (efficiency, J_{sc}, and R_s). From now onward, these three regimes will be denoted as A, ranging from 0 (as-cast) to 4 s of exposure time; B, from 4 s to 15 s; and C, from 15 s onward.

[A] The experiments and analysis of ellipsometry data were performed by Dr. Mariano Campoy-Quiles.
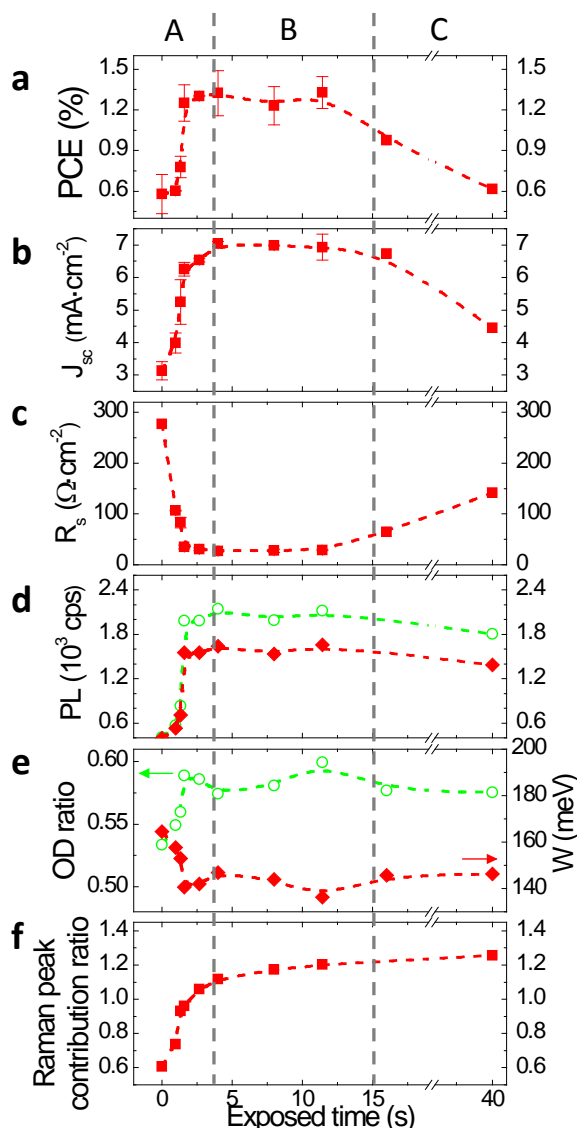
Figure 3.21. Dependency on time of vapour printing of a) power conversion efficiency, b) J_{sc} measured at 100 mW·cm^{-2} AM 1.5G, c) series resistance of the devices, d) photoluminescence vibronic features at 724 nm (empty circles) and 662 nm (solid diamonds), e) optical density ratio of 2.09/2.27 eV (left axis, empty circles) and free exciton bandwidth W of P3HT aggregates (right axis, solid diamonds), calculated with eq 1 from ref. [59], and f) Raman peak contribution ratio between ordered and disordered P3HT, as defined in Figure 3.20. The gray, dashed vertical lines define regimes A, B and C. Dotted lines are guides to the eye.

The V_{oc} (not shown) is slightly reduced in regime A and then remains almost constant. As mentioned before, this is likely due to the vapour-induced crystallisation of P3HT, as strongly suggested by the rapid growth in PL intensity (Figure 3.21d) and both 0-

0/0-1 transition energy absorbance peaks (Figure 3.21e) and the ordered/disordered P3HT ratios signatures in Raman experiments (Figure 3.21f). J_{sc} rapidly increases in regime A, reaching a maximum of 7.45 mA·cm^{-2} in regime B in just 4 s of exposure and, then, slowly decays in regime C. This behaviour is similar to that described by Agostinelli et al., where they distinguish two different time windows involving the evolution of microstructure during thermal annealing: a first one wherein crystallisation of the polymer correlates with a major increase of photocurrent; and a second window during which aggregation of PCBM molecules continues.[107] Compared to this work, regime A would be equivalent to the first time window, whereas the second window would correspond to both regimes B and C, being B the first step where the phase segregation is optimal for OPV performance. Despite the fact that higher PL emission is observed in regime B, and thus, there is more monomolecular recombination, the overall morphology of the layer is improved in the sense that it enhances charge transport, leading to a large J_{sc} increment. This will be discussed in more detail below. A more dispersive tendency in the efficiency is found compared to J_{sc}, as seen in Figure 3.21 (a,b), which is attributed to more scattered FF values. Even then, the variations in J_{sc} are the dominant factor: a maximum of efficiency is also obtained in regime B. The evolution of the series resistance is also in accordance to the already described features. The reorganisation of P3HT chains during regime A would lead to a better morphology (R_s is reduced), while at longer exposure times, in regime C, the increasing aggregation of PCBM clusters would worsen again the morphology of the layer (R_s arises), possibly reducing carrier mobility.[107] The inverted tendency of R_s with respect to J_{sc} evidences that vapour printing is changing the morphology of the organic layer and possibly its interfaces.

Note that the time-scale of each regime is only valid for this specific system, with CB as the solvent and P3HT:PCBM as the blend, with the already described working conditions. The thickness of the blend layer (160 nm) is in the optimal range for OPV best performance.[108] Extra layers with lower (130 nm) and higher (270 nm) thicknesses were prepared and characterized. UV-Vis spectra (**Figure 3.22**) reveal very similar P3HT crystallisation time-scales upon vapour printing annealing in all samples.
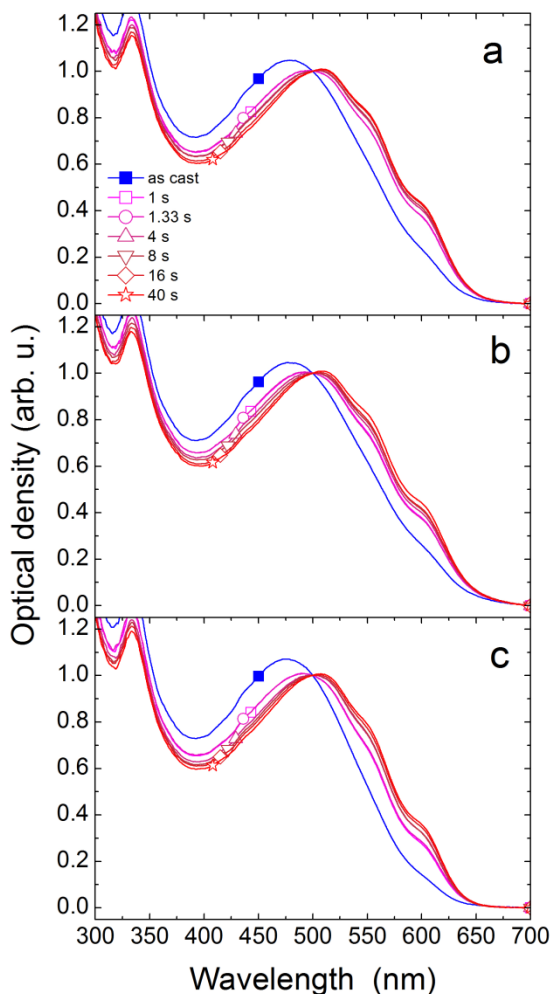
Figure 3.22. UV-Vis spectra of glass/P3HT:PCBM samples vapour annealed at different printing times. The data shown correspond to a) 130 nm, b) 160 nm and c) 270 nm of blend layer thicknesses. All the spectra were normalized by their absorption value at 500 nm.

As described by Clark et al., the ratio of the 0-0 and the 0-1 regioregular P3HT peak absorbance, located at 2.09 and 2.27 eV, respectively, is related to the free exciton bandwidth (W) of the aggregates (i.e. crystalline, ordered P3HT). As it can be seen in Figure 3.20c, the C=C symmetric stretch at ~1449 cm^{-1} dominates the coupling to the electronic transition. Thus, W can be estimated by using this ratio.[59] W is related to the conjugation length and intrachain order, assuming similar interchain order in the films. A decrease in W will be an irrefutable signature of an increase in conjugation length and order. This behaviour is observed in Figure 3.21e. In detail, W is decreased in regime A and then remains almost constant in both regimes B and C, which is in

good agreement with other features suggesting the rapid increase in P3HT ordering, such as PL quenching (Figure 3.21d) and Raman plot (Figure 3.21f). Similarly, the decrease of W upon thermal annealing has been previously described by Turner et al., where two temperature regions are observed. W is decreased in the first range of temperatures until a certain temperature, above which W remains nearly constant.[109]

Furthermore, as **Figure 3.23** shows, the biggest changes in P3HT crystallisation take place in a very fast time-scale (1 s) regardless of blend thickness, suggesting that solvent diffusion into the whole layer (i.e. swelling time) occurs almost instantaneously when using the vapour printing technique (see also below).
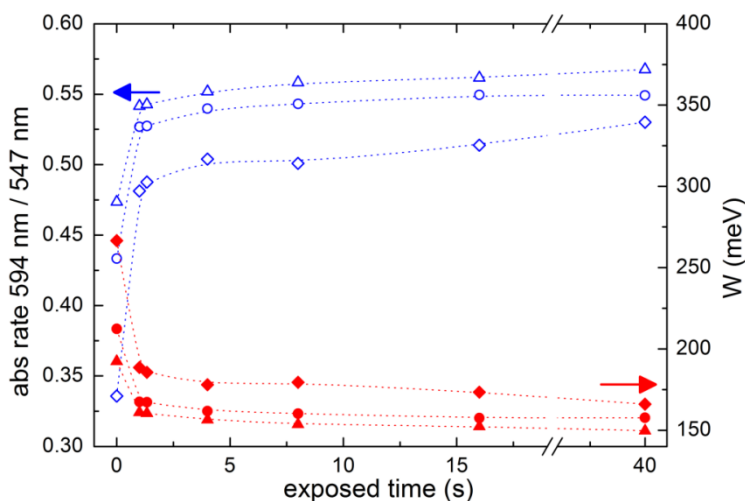
Figure 3.23. Dependency on time of vapour printing of the optical density ratio of 2.09/2.27 eV (left, empty symbols) and free exciton bandwith W of P3HT aggregates (right, filled symbols). The plot shows the comparison between three different blend layer thicknesses: 160 nm (circles), 190 nm (triangles) and 270 nm (diamonds). All of them show the same time-scale behaviour.

However, while P3HT ordering is not changing anymore, some other features worsen in the mentioned regime C (e.g. J_{sc} and R_s). At this point, it is important to notice that UV–Vis and Raman measurements here exposed only focus on the evolution of P3HT ordering. This supports the hypothesis that other mechanisms regardless of P3HT degree of crystallinity such as PCBM aggregation and too large phase segregation may damage the cell performance at longer exposure times. A large phase segregation, leaving isolated PCBM domains within non-crystallised P3HT regions and poorer transport,[107] would explain the lowering of J_{sc}. In this context, the almost constant PL

observed in regime C may be understood considering that a small amount of (trapped) PCBM molecules is enough to efficiently quench the PL.[61]

To investigate whether PCBM molecules still diffuse upon vapour printing once the polymer is not crystallising any further, we have carried out variable angle spectroscopic ellipsometry (VASE) experiments on samples of the three different P3HT:PCBM layer thicknesses mentioned above and vapour printed during seven different times. VASE has been proven very sensitive to monitor crystallisation and molecular diffusion in organic photovoltaic blends.[104] For the analysis of the data, we have used a model consisting of a bilayer-like structure with different compositions on the top and the bottom of the film. To asses both process directly, that is, crystallinity and diffusion, we have separated the contribution of the polymer in the crystalline and amorphous part, using as references the regioregular P3HT and regiorandom P3HT optical constants (similarly to the Raman analysis above). In this approach, a blend film with 100% effective crystallinity would be a blend film that has the same degree of crystallinity than a pure regioregular P3HT film. The diffusion can be investigated by the variations in PCBM percentage across the film thickness, that is, in our model, the different concentrations between the top and bottom sublayers. A single parameter to evaluate this is the effective slope of the gradient in PCBM concentration across the film, which is shown in **Figure 3.24**.
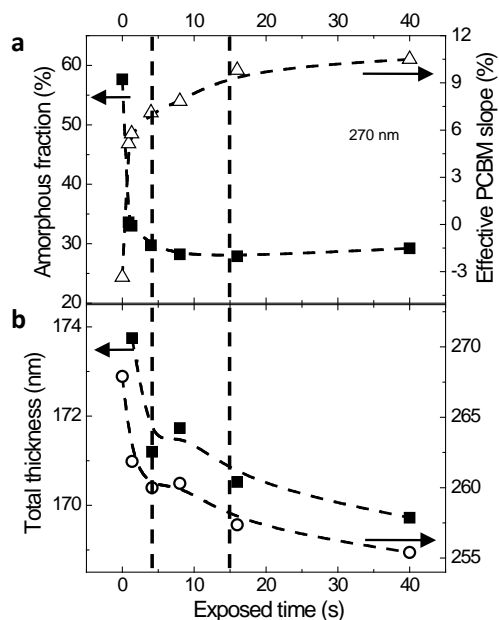
Figure 3.24. Ellipsometrically deduced structural parameters for P3HT:PCBM blends vapour annealed during different times. a) shows the volume fraction of amorphous P3HT (solid squares, left axis) and the effective slope in the vertical segregation of PCBM (open triangles, right axis). The variation of the film thickness with vapour printing time is shown in b) for a thin (solid squares, left axis) and a thick (open circles, right axis) samples. These data were experimentally measured and analysed by Dr. Mariano Campoy-Quiles.

Interestingly, this analysis shows that the bottom of the blend layer contains more PCBM than the top, whereas the polymer amorphous fraction is higher at the top of the film. Figure 3.24 shows the volume fraction of amorphous P3HT as well as the PCBM slope as a function of annealing time. Both magnitudes drastically change during the regime A: the fraction of amorphous P3HT sharply decreases, whereas the effective slope of the PCBM vertical profile increases. Interestingly, the amorphous fraction reaches a plateau in regime B staying at an approximate fixed value thereafter. This provides further evidence that crystallisation of the polymer occurs mainly during regime A and stops after that. On the other hand, the slope of the PCBM concentration keeps changing upon vapour annealing up to 40 s, indicating that PCBM diffusion continues after the polymer chain stops crystallising. Moreover, the total film thickness keeps decreasing upon vapour printing in regimes B and C up to <5% of the initial thickness for the films studied (160–270 nm thick), which indicates that molecular reordering continues once no additional polymer crystallisation is detected (Figure 3.23b). These two facts, PCBM vertical diffusion and thickness

shrinkage, strongly supports our hypotheses above. We note that despite the as-cast thick (270 nm) films being more amorphous than thinner (170 nm) films, the final volume fraction of the amorphous component is very similar (ca. 25% less crystalline than the pristine regioregular P3HT film) and is reached in the same time scale (first 4 s). The ellipsometric analysis in terms of crystallisation is also confirmed with UV–Vis (Figure 3.22). This indicates that vapour molecules penetrate the film rapidly and regardless of the film thickness (for this thickness range), and thus vapour printing optimum conditions do not markedly depend on active layer thickness.

To summarize, in as cast films both P3HT and PCBM are well intermixed and so the CT is presumably high, whereas transport of the separated charges is poor due to the lack of paths to both electrodes (low crystallinity and phase segregation), giving as a result a low J_{sc}. Opposite free charges may find each other easily in this very well mixed blend before reaching the contacts, thus recombining to the ground state (bimolecular recombination). When P3HT crystals grow (regime A) and suitable phase segregation and morphology are generated (regime B), a good equilibrium between the CT and transport is obtained, leading to the optimal OPV performance. At longer times (regime C) both phase segregation and PCBM aggregation would be too high, worsening the morphology and transport properties. **Figure 3.25** shows a schematic representation of our interpretation of the evolution of the organic layer microstructure upon vapour printing annealing, consistent with the results above.
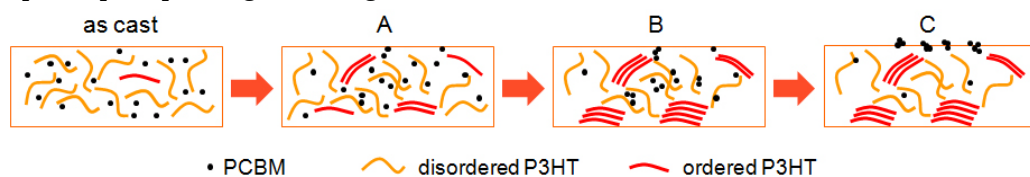
Figure 3.25. Representation of the organic layer microstructure evolution upon vapour printing annealing. A, B and C captions correspond to the above described regimes. A good intermixing (low phase segregation) of PCBM and mainly disordered P3HT (poorly crystallised) is obtained in the as cast film. In regime A P3HT crystals rapidly grow up to a maximum of crystallisation in regime B, where at the same time suitable phase segregation is obtained as well as charge transport pathways to both electrodes. At longer times both phase segregation and PCBM aggregation would continue, reducing OPV performance.

3.3.5. The importance of solvent vapour pressure

Finally, the versatility of vapour printing is tested by probing two different solvents. Toluene and 1,2,3,4-tetrahydronaphthalene (THN) are used to anneal another set of samples and fabricate devices in the same manner as described above for the CB case.

We note that the same blend solution based on CB is used to spin cast the organic layer to be able to compare and isolate the vapour printing process from the film deposition. The vapour printing solvents are chosen according to their different volatilities and the relatively good solubility of both P3HT and PCBM within them.[110] Their non-chlorinated nature may make them particularly relevant for industrial applications. According to Machui et al.,[111] the solubility of the fullerene within these solvents is high enough, whereas CB is clearly a better solvent for P3HT in comparison to toluene and THN (see **Table 3.6**). However, the vapour annealing of the active layer may occur even with modest solubility as long as the solvent can diffuse into the layer. The latter makes it possible to study the effect of vapour pressure as an independent parameter. The contribution of solubility, which may also have a strong effect on the time-scales as well as on the maximum crystallinity achievable using the vapour annealing, goes beyond the scope of this work. In fact, the relationship between solvent properties and degree of P3HT crystallisation is complex and yet not fully understood.[112]

Table 3.6. Photovoltaic performance of solar cells with different vapour printing solvents and the solubility of P3HT and PCBM within them

Solvent	V_{oc} (V)	J_{sc} (mA·cm⁻²)	FF (%)	PCE (%)	Vapour pressure (mm Hg)	Solubility[a] (mg·mL⁻¹)	
						P3HT	PCBM
THN	0.60	3.71	34.0	0.76	0.4	0.7	114.8
Toluene	0.56	6.81	40.5	1.55	28.4	0.7	15.6
CB	0.56	7.45	36.3	1.52	12.0	15.9	59.5

[a] Taken from reference [111]

At a given nitrogen flow rate, toluene saturates at higher concentrations due to its higher vapour pressure. In other words, for a given flux, nitrogen carries more toluene and many less THN molecules with respect to CB. Therefore, toluene will need less time to affect the materials, setting aside the differences in solubility. It is thus expected that the annealing time for the best performing point could be optimised by choosing an adequate solvent in terms of vapour pressure and solubility.

The J–V curves of the best performance solar cells obtained with toluene and THN are compared to that with CB in **Figure 3.26**.

Table **3.6** summarizes the solar cells parameters, the solvent vapour pressure values, and the solubility of the materials. All THN samples show a poor polymer crystallisation even at long times of exposure and their performance are almost the same as the as-cast sample. Almost no changes in the colour of the organic layer after the annealing treatment suggest that very long times or solvent containers with very large evaporating surface are needed to reach the desired morphology when working with THN. The latter indicates that low vapour pressure solvents are not the best suited for efficient vapour annealing using the present apparatus.
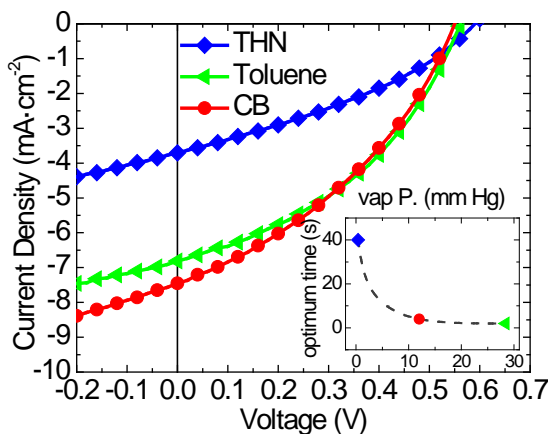
Figure 3.26. J–V characteristics of representative devices vapour printed with THN, toluene, and CB. The estimated optimal annealing time for each solvent versus vapour pressure is plotted in the inset.

On the other hand, the experiments performed using toluene show promising results, with solar cells performing similarly to those with CB. Although the data collected is a bit more dispersive compared to CB, the maximum efficiency obtained with toluene solvent is located at around 2 s of exposure, even faster than with CB. This correlates with the vapour pressure values of both solvents, being toluene (28.4 mmHg) more volatile than CB (12.0 mmHg). The inset in Figure 3.26 illustrates this correlation. The required vapour printing time for best OPV performance related to vapour pressure of the corresponding solvents shows an exponential decay tendency. It is thus demonstrated that P3HT crystallisation occurs much faster (<5 s) with vapour printing in contrast to slower methods such as thermal (5-10 min)[99] or solvent annealing (>1 min).[102]

3.4. CONCLUSIONS

In this chapter it has been discussed how processing conditions in inkjet printing can be tuned to address optimal morphology of the active layer. A special emphasis has been set on the drying process. Firstly, it has been shown how mixtures of high and low boiling point solvents can prevent macroscopic inhomogeneities on the film. Then, the processing parameters that govern the drying behaviour have been identified. Both generic (temperature of the substrate) and specific to inkjet printing (drop spacing, number of jets, pattern) parameters have been investigated. We have developed an interesting approach based on EQE maps on gradually changing samples that enable an easy identification of the optimal drying time. This position-sensitive screening allows defining a proper printing pattern.

Further optimisation directed to enhance the performance of the devices have revealed that the incorporation of a 1nm LiF interlayer is more efficient than an extra thermal annealing step after the evaporation of the Al cathode. Also, it has been shown that lower efficiencies were obtained in OPV devices with both PEDOT:PSS and P3HT:PCBM layers processed by inkjet printing (2.85%) as compared to those in which only the active layer was inkjet printed (3.54%). A worse morphology of the PEDOT:PSS layer obtained when processed by inkjet printing was proposed as explanation.

Despite that, the comparable performances obtained with OPV devices processed from spin coating (3.52%) and doctor blading (3.21%) indicate that inkjet printing is a competent alternative technique.

Concerning post-processing treatments, it has been demonstrated that vapour printing is a promising alternative for fast OPV processing. We have studied the effect of the vapour printing annealing time on the structural properties and photovoltaic performance. At early times, P3HT crystallisation governs the process, whereas at longer times, PCBM aggregation and phase segregation become predominant. We have demonstrated that optimal morphology, and thus, maximum performance are reached in very short time-scales (<5 s) compared with other annealing techniques. Vapour pressure of the annealing solvent has been found to be a key parameter, being volatile solvents the most suitable for fast vapour printing.

CHAPTER 4

Green solvents for organic solar cells

Abstract

Replacing halogenated solvents in the processing of organic solar cells by benign solvents is a required step for the commercialization of this technology, due to industrial and environmental requirements. Of course, a good solubility of the materials is essential to be properly processed. This is even more critical in bulk heterojunction systems, where two (or more) materials are processed from the same solution. Hence, determining or better predicting the solubility behaviour of a given material is of big importance.

In this chapter the potential of the Hansen Solubility Parameters (HSP) analysis for the design of green ink formulations for solution-processed active layer is demonstrated. We first use this method in a small molecule system based on a star-shaped D-π-A molecule and a fullerene derivative. We then use the predicted HSP to find alternative, green solvents, which we use for OPV fabrication. The success of this method is proven: similar performances are obtained with non-halogenated solvents in comparison to reference devices processed from halogenated solvents.

We also apply this analysis for low band gap polymers. In this case the replacement of halogenated solvents does not succeed at the same level. The lower stability of these materials is also put on evidence.

4.1. INTRODUCTION TO HANSEN SOLUBILITY PARAMETERS

4.1.1. HSP theory

The concept of solubility parameter was first introduced by Hildebrand and Scott,[113] who defined it as the square root of the energy of vaporization density:

$$\delta = \sqrt{\frac{\Delta E_v}{V_m}} \qquad [4.1]$$

where δ is the Hildebrand solubility parameter, ΔE_v is the energy of vaporization and V_m is the molar volume. The solubility parameter is an intrinsic property of the molecules and it is derived from the energy required to convert a liquid into a gas (i.e. energy of vaporization). The latter is a direct measure of the total (cohesive) energy holding the liquid's molecules together.

Hansen made an extension of this theory by splitting the Hildebrand solubility parameter into three different contributions,[114] considering that all the different types of bonds holding the liquid together are broken by evaporation. These three contributions, known as Hansen solubility parameters (HSP), are the atomic dispersive forces (δD), the molecular permanent dipole-permanent dipole (polar) interactions (δP) and the molecular hydrogen-bonding interactions (δH):

$$\delta^2 = \delta_D^2 + \delta_P^2 + \delta_H^2 \qquad [4.2]$$

When each of these contributions are set as the axis of a three dimensional "solubility" space, *aka* Hansen space, the HSP of any molecule can be therein plotted. This allows us to easily identify and compare molecules as a function of their own chemical interactions (see example in **Figure 4.1a**). Logically, the closer two molecules are in the Hansen space, the higher similarity in terms of chemical interactions they show. This is nothing more than putting numbers onto the famous aphorism "*like dissolves like*", and it is precisely what we need to find suitable solvents for a given solute.
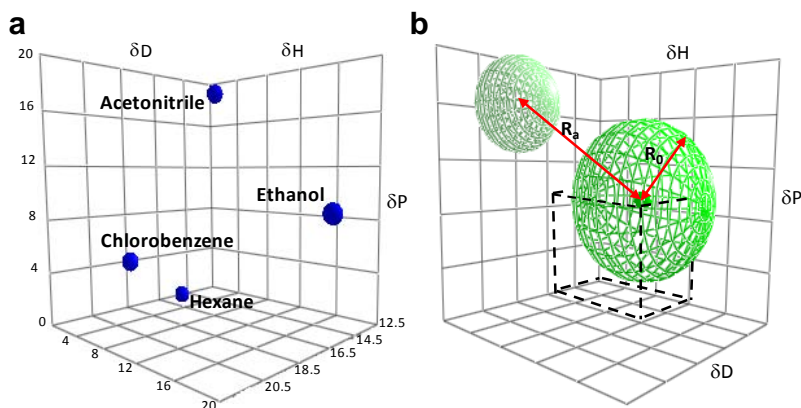
Figure 4.1. a) 3D plot of the HSP in the solubility space of four solvents with markedly different chemical interactions. δD, δP and δH are the dispersive, polar and hydrogen-bonding contributions to solubility. In contrast to hexane, a non-polar solvent, acetonitrile exhibits high polarity. In turn, dispersive and hydrogen-bonding contributions predominate in chlorobenzene and ethanol, respectively. b) R_0 is the radius of the solubility sphere and R_a is the relative distance between the HSP of two molecules.

Given a molecule, the three HSP define the centre of a sphere. Its radius (R_0) delimits the regime wherein the solubility of that molecule is above a given threshold, defined by the radius itself (see **Figure 4.1b**). Although the solubility volume of a solute is likely to have an ellipsoidal shape, it is often assumed as spheroid in order to simplify the calculations.

By setting a solubility limit of a solute, in mg·mL^{-1}, the radius of the sphere will be determined. All the solvents whose HSP are located inside this defined volume can be considered as "good" solvents, as they are supposed to show a solubility higher than that threshold, according to the theory. On the contrary, those solvents with the HSP out of the sphere will exhibit lower solubilities, thus they can be considered as "bad" solvents. This qualitative distribution of solvents as "good" or "bad" (or solvents and non-solvents) is therefore a relative classification, as it is related to the chosen solubility limit. The higher is the threshold (lower R_0 radius), the more restrictive the system is, and thus many less solvents will accomplish the solubility requirements. Appropriate choice of R_0 will be related to the solubility requirements for a given deposition method and application.

The solubility distance (R_a) is the parameter that defines the distance from the centre of the sphere of one molecule (2) to another (1) in the Hansen space (Figure 4.1). Taking into account their corresponding HSP, R_a is calculated via Equation 4.3.

$$R_a^2 = a(\delta_{D2} - \delta_{D1})^2 + b(\delta_{P2} - \delta_{P1})^2 + c(\delta_{H2} - \delta_{H1})^2 \qquad [4.3]$$

being a, b and c weighting factors. Hansen suggested to set them to a=4 and b=c=1, according to empirical approaches. These values convert the otherwise ellipsoidal body into a spheroid. The R_a distance between two molecular species is inversely proportional to their mutual solubility. Therefore, in order to see how compatible different solvents might be with a given material, we should determine their corresponding HSPs and calculate how far they are from each other.

The relative energy difference (RED) parameter is the relation between the solubility distance R_a and a selected solubility limit radius R_0,

$$RED = \frac{R_a}{R_0} \qquad [4.4]$$

This parameter is used to classify a set of solvents as "good" (solvents) or "bad" (non-solvents) for a target solute or molecule. When RED is lower than 1, the R_a distance between the solvent and the solute is lower than the set solubility radius R_0, and thus the solvent is inside the solubility sphere and can be considered as a "good" solvent. On the contrary, when RED is higher than 1, the "bad" solvent will be located outside the solubility volume defined by the R_0 radius. Note that calculated HSP of most solvents are tabulated in the literature.

4.1.2. Traditional method to determine the HSP

The traditional method to experimentally determine the HSP of a molecule consists in using a collection of 30-40 solvents randomly distributed in the Hansen space and measuring the absolute solubility of the material within them to distinguish between solvents and non-solvents (with a set solubility limit). This scoring is used by the HSPiP software[115] to numerically predict the position of the centre of the solubility sphere (i.e. the Hansen solubility parameters) of the molecule and its radius, taking into account the selected solubility limit. It is important that this collection of solvents covers a volume as big as possible in the Hansen space, in order to ensure that different chemical interactions are taken into account. As an example, the determination of the HSP of the polymer P3HT using this method was reported by Machui et al. (see **Figure 4.2**)[116]
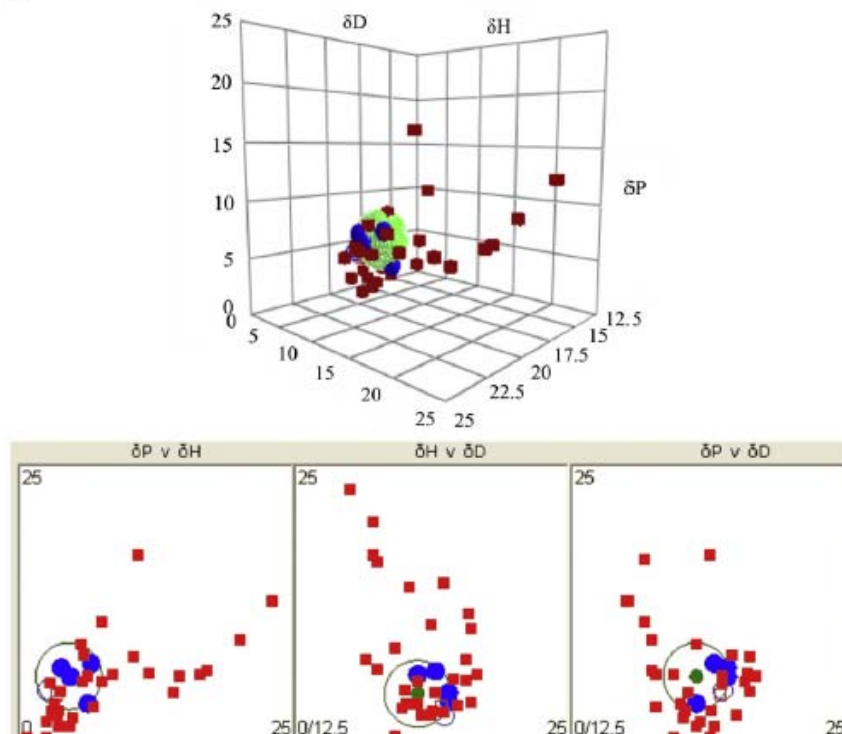
Figure 4.2. HSP diagram of P3HT using the traditional different solvents method. The blue circles are considered as solvents and the red squares are the non-solvents. Reproduced with permission from reference [116]. Copyright 2012, Elsevier B.V.

This method involves a tedious experimental determination of the absolute solubility of the solute in each of these 30-40 solvents. In contrast, the same group reported an alternative method to determine the HSP of organic semiconductors with reduced experimental effort: the binary solvent gradient method.[116]

4.1.3. Binary solvent gradient method

Machui and co-workers suggested to use mixtures of solvents and non-solvents (hence the name of binary solvent gradient method) to obtain HSP.[116] By systematically varying the solvent blend composition, it was possible to map the transition from solubility to non-solubility in different directions in the Hansen space, which resulted in faster and cheaper determination of the solubility volume with higher fit accuracy. It was found that three different solvent gradients resulted in an optimal compromise between effort and accuracy. Those three non-solvents were chosen such to represent a variation of dominantly one coordinate within the Hansen space, i.e. the hydrogen, the polar or the disperse contribution (**Figure 4.3**).
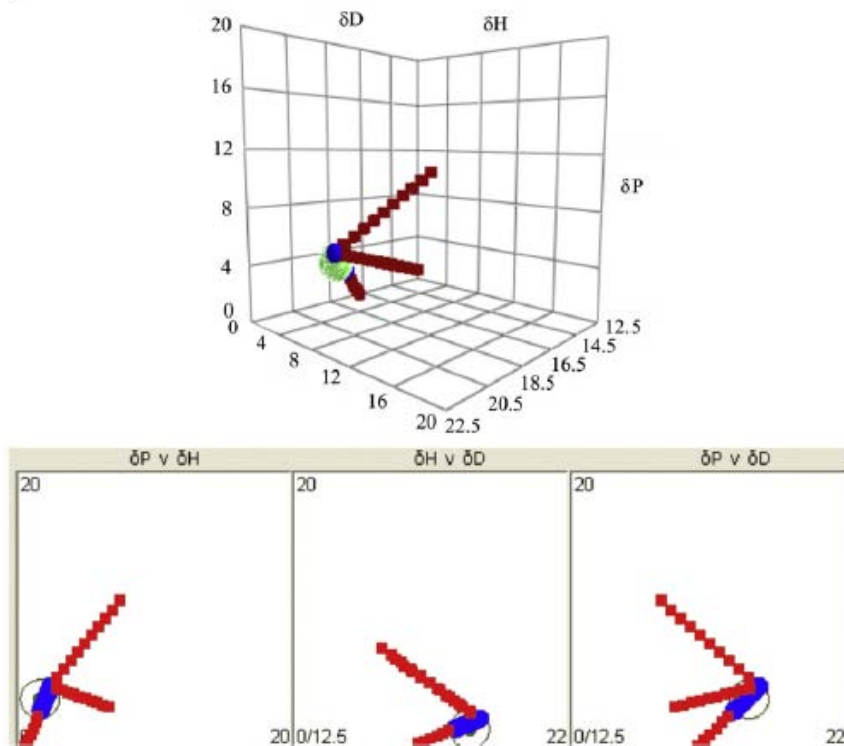
Figure 4.3. Determination of the HSP of P3HT using the binary solvent gradient method. Reproduced with permission from reference [116]. Copyright 2012, Elsevier B.V.

With this experimental data set, it is possible to recalculate the HSP setting different solubility limits (i.e. varying the solubility volume). This was performed by Machui and co-workers and slight variations in the HSP of both P3HT and PCBM molecules were found. Ideally, of course, the prediction of the HSP of a molecule should be independent on the set conditions, as this is an intrinsic property of materials. These changes are due to the limited number of experimental points used for the determination of the solubility parameters. Hence the importance of choosing adequate solvent gradients that define clearly different axis in the Hansen space. In principle, higher accuracy may be expected with higher solubility limit (more restrictive scenario). However, considering that no extra experimental work is needed, a more logical strategy might be to set the solubility limit for the determination of the HSP as the same value as for each case study of suitable solvents. For instance, we might be seeking solvents that reach at least a solubility of 7 mg·mL^{-1} for a concrete processing of a solute. In this case, we should better use this threshold to determine the HSP of that solute.

4.2. IDENTIFICATION OF GREEN SOLVENTS FOR SMALL MOLECULE ORGANIC SOLAR CELLS

4.2.1. Why small molecules?

The name of small molecule organic solar cells typically refers to the nature of the p-type (donor) material in the bulk heterojunction active layer. We must not forget, however, that the most widely used n-type (acceptor) materials in solution processed OPVs are indeed two small molecules: $PC_{60}BM$ and $PC_{70}BM$. In 1995 Hummelen and co-workers reported the synthesis of $PC_{60}BM$.[117] By attaching a phenyl and butyric acid methyl ester units, the solubility of the molecule in different organic solvents improved significantly in comparison to pristine C_{60} fullerene. Later, broader absorption capability was achieved with the C_{70} counterpart by breaking the symmetry of the C_{60} fullerene moiety.[118] The success of these fullerene derivatives is due to their high electron affinity, good charge separation ability, efficient electron transport, reduced recombination, and the relatively easy optimisation of phase separation within the donor:acceptor blend.[119] For all these reasons, including their good solubility behaviour in many organic solvents, $PC_{60}BM$ and $PC_{70}BM$ are still the best performing acceptor molecules.

On the other hand, conjugated polymers have been typically used as donor materials in solution processed BHJ layers. These semiconducting polymers often show modest solubility capability, like in the case of P3HT. The latter may be a limiting factor for an efficient replacement of halogenated solvents in OPV fabrication. In contrast to the low purity and wide molecular weight distribution of polymers,[120] organic small molecules offer some advantages such as well-defined molecular structure, higher purity and more definite molecular weight distribution without batch-to-batch variations.[121] Furthermore, as a general rule, lower molecular weight is related to higher solubility, besides the molecular moieties. As an example, the solubility of alcohols in water decreases as the molecular size of the alcohol molecule increases. Therefore, a strong motivation to move towards small molecules arises, since small molecules are more likely to be soluble in a wider variety of (green) solvents. Other aspects related to their synthesis like higher reproducibility, lower synthetic effort and thus potentially cheaper processing may also support this motivation.

The aim of this subchapter is to generalize the use of the binary solvent gradient method[116] to other materials systems in order to advance a simple general rationale for

the identification of green solvents and, in particular, those compatible with small molecule based OPV. Two materials are studied: a D-π-A star-shaped small molecule and a fullerene derivative.

4.2.2. Determination of HSP of N(Ph-2T-DCN-Et)$_3$ and PC$_{70}$BM

4.2.2.1. Description of the molecules

The synthesis and photovoltaic properties of the D-π-A star-shaped molecule tris{4-[5''-(1,1-dicyanobut-1-en-2-yl)-2,2'-bithiophen-5-yl]phenyl}amine N(Ph-2T-DCN-Et)$_3$ (**Figure 4.4**) were first reported in ref [122]. In that work, the small molecule was blended with [6,6]-phenyl-C$_{71}$-butyric acid methyl ester (PC$_{70}$BM) in chlorobenzene (CB) with the addition of 4-bromoanisole (BrAni) and used as the active layer in solar cells resulting in a 3.60% optimised power conversion efficiency (PCE). The high V_{oc} (0.96 V) therein reported is a consequence of the low bandgap of the star-shaped molecule (1.89 eV) and suitable energetic levels (-5.32 eV and -3.41 eV for HOMO and LUMO levels, respectively). Reduced steric hindrance and eliminated torsional interactions result in planar structure and high absorption.[122] The latter make this molecule attractive for OPV applications. As it can be seen in Figure 4.4, the molecular structure of the star-shaped molecule consists in an aromatic core (triphenyl amine), three bithiophene bridging units and three polar ending groups. These different moieties may have dissimilar affinity to organic solvents, resulting in several chemical interactions. Thus, a wide variety of (non-chlorinated) solvents might be suitable to dissolve the molecule.
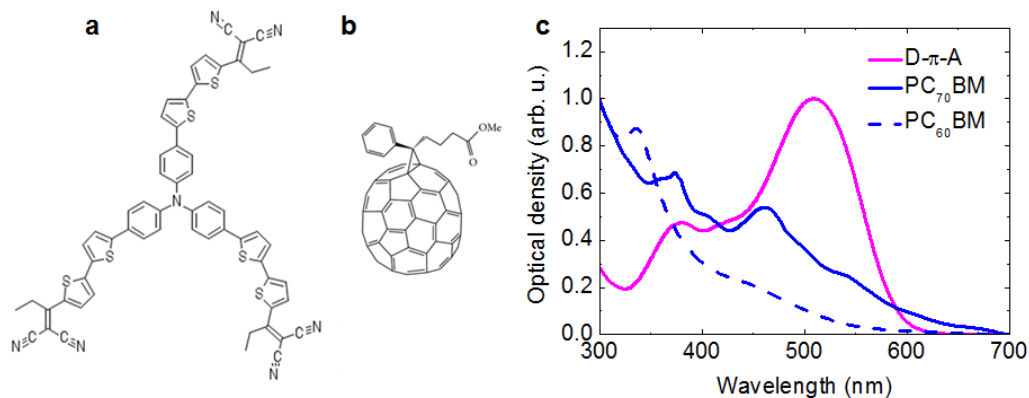
Figure 4.4. Molecular structures of a) N(Ph-2T-DCN-Et)$_3$ and b) PC$_{70}$BM with their corresponding absorption spectra (c). The spectrum of PC$_{60}$BM (dashed line) shows lower absorption than PC$_{70}$BM in the 400-650 nm range.

As said above, the broken symmetry of the C$_{70}$ moiety in PC$_{70}$BM results in a broader absorption in contrast to the C$_{60}$ based fullerene derivative (Figure 4.4c). This extended absorption in the visible range will lead to the generation of a larger amount of excited charges. On the other hand, the D-π-A molecule shows a broad absorption in the range between 350 and 600 nm, with a maxima in 509 nm.

4.2.2.2. Using the binary solvent gradient method

The binary solvent gradient method was used to determine the HSP for the investigated materials. As already mentioned, this method provides a precise determination of the HSP volume of a solute and enables the estimation of the Hansen surface with high accuracy.[116]

The first step consists of measuring the absolute solubility of the solutes in at least three different binary solvent gradients. As explained above, the choice of solvents was done by taking their different preferential HSP contributions into account, which have an obvious relationship with their specific chemical structures. For instance, propylene carbonate and cyclohexane are high polar and non-polar solvents, respectively (preferential δ$_P$ contribution), whereas the alcohol group in 2-propanol gives a higher hydrogen bonding (δ$_H$) contribution to this solvent. Acetone and DMSO were also used as bad solvents. On the contrary, chlorobenzene was the good solvent for both molecules. The absolute solubility values of N(Ph-2T-DCN-Et)$_3$ and PC$_{70}$BM in their corresponding series of solvent blends are presented in **Figure 4.5**. Exponential behaviours are expected with solubility increasing when going from the non-solvent

rich solutions to the good solvent rich solutions.[116] This is in fact what is observed for the binary mixtures studied for $PC_{70}BM$, where similar trends were obtained for the 3 tested non-solvents. The most noticeable fact is the absolute solubility value of $PC_{70}BM$ in pristine chlorobenzene (207 mg·mL^{-1}), which showed more than a threefold increase with respect to reported values for $PC_{60}BM$ (60 mg·mL^{-1})[116,123], as seen in Figure 4.5b. As observed for $PC_{60}BM$,[116] the trend with the 3 solvent blends is nearly comparable, being in both cases the binary CB/DMSO mixture the blend which gives higher solubilities.
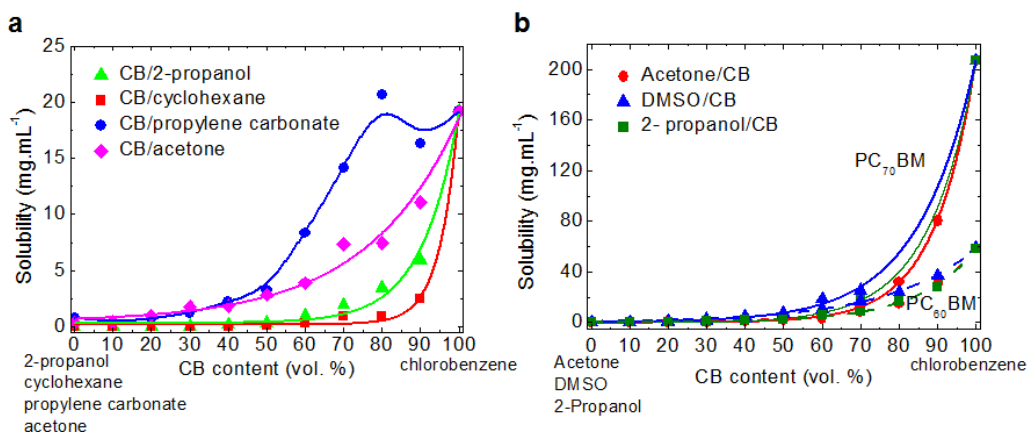
Figure 4.5. Solubility of a) N(Ph-2T-DCN-Et)$_3$ and b) $PC_{70}BM$ ($PC_{60}BM$ in dashed lines for comparison, from reference [116]) in solvent blends. The lines represent the exponential fit except for CB/propylene carbonate gradient in (a), where act as guide to the eye.

The exponential tendency is also observed for the small molecule in CB/cyclohexane, CB/2-propanol and CB/acetone solvent blends, although different trends are observed. More surprisingly, in CB/propylene carbonate mixture (Figure 4.5a), higher solubility in comparison to pristine CB was obtained with 80% vol. of CB. Although pristine propylene carbonate cannot be considered as good solvent for the material itself (a solubility of only 0.80 mg·mL^{-1} was measured), this behaviour when mixing with a good solvent such as chlorobenzene can be explained in terms of HSP reasoning, which in turn can explain the differences between the CB/2-propanol, CB/cyclohexane and CB/acetone mixtures. This will be discussed later.

These data were introduced in the HSPiP software[115] in order to predict the HSP for the materials under study. This prediction employed the standard fitting routine while the solubility space was assumed to be spherical. Following the work reported by Machui et al,[116] in order to investigate the predictions of the binary solvent gradient

blend method for the HSP for both donor and acceptor materials, four solubility thresholds were chosen: 10 mg·mL^{-1}, 5 mg·mL^{-1}, 2 mg·mL^{-1} and 0.5 mg·mL^{-1}.

As an example, the Hansen diagram for the solubility threshold of 10 mg·mL^{-1} is shown in **Figure 4.6**. Every point represents a specific blend composition related to Figure 4.5. Blue circles correspond to solvent blend compositions that show solubility values above 10 mg·mL^{-1} and thus are inside the green sphere (RED<1), which represents the solubility volume of the solute. On the other hand, red squares represent the counterpart solvent blends with lower solubility (RED>1). In the case of the star-shaped molecule higher accuracy of the volume of the sphere (i.e. R_o radius) was obtained by introducing 4 axes instead of 3 in the HSP determination.
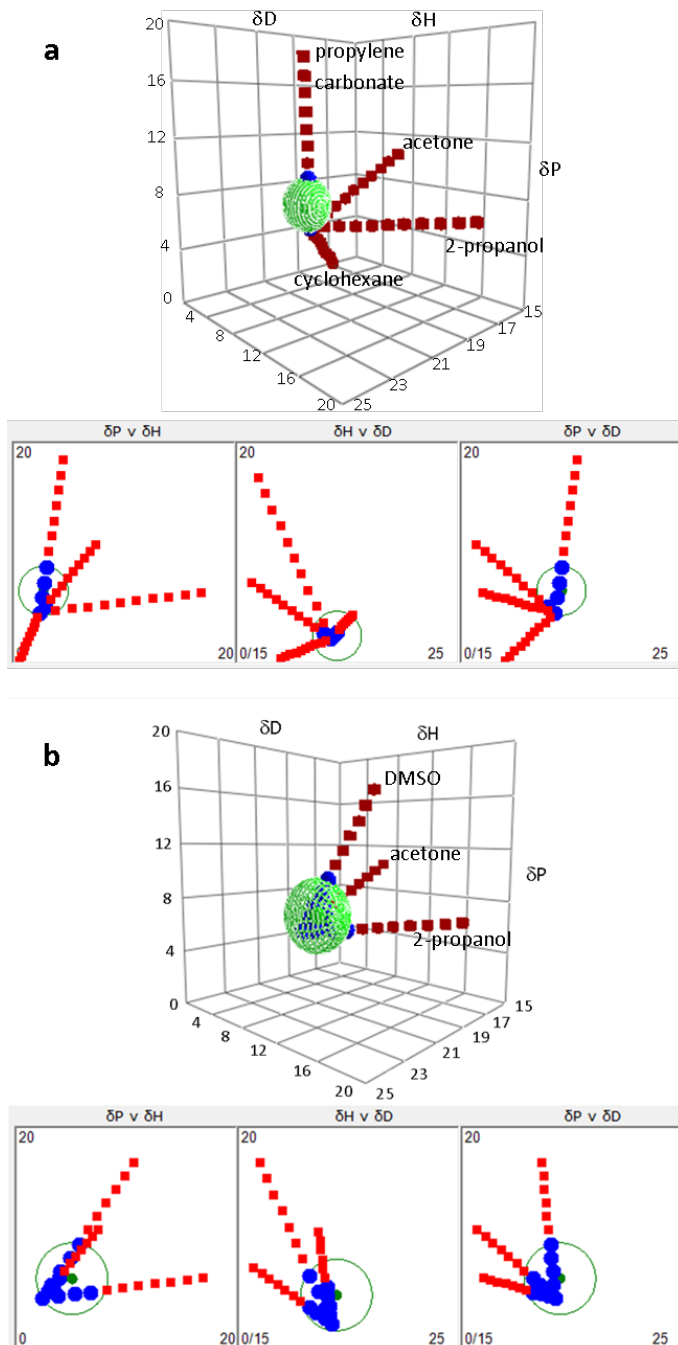
Figure 4.6. 3D and 2D HSP diagrams of a) N(Ph-2T-DCN-Et)$_3$ and b) PC$_{70}$BM with solubility limit of 10 mgmL^{-1} (green sphere). Blue circles correspond to solvents that are inside the sphere and red squares to those external (all units of HSP are in MPa$^{1/2}$).

It can be seen in Figure 4.6 how the selected solvent gradients describe clear different directions in the Hansen space. Another important fact deduced from Figure 4.6 is that pristine chlorobenzene (origin of the 4 axes) is not located very close to the centre of the N(Ph-2T-DCN-Et)$_3$ solubility sphere. Although CB was chosen as "good solvent", it was of course not yet known how "good" it was (i.e. how close to the centre of the sphere it is). Moreover, some points in the CB/propylene carbonate gradient are closer than pristine CB to the centre of the sphere (i.e. with lower R_a). This explains the unexpected higher solubility values obtained at those points (Figure 4.5a). The obtained HSP for both donor and acceptor materials are summarized in **Table 4.1**.

Table 4.1. Hansen solubility parameters for N(Ph-2T-DCN-Et)$_3$ and PC$_{70}$BM. The last two columns indicate the total number of solvent systems among the different gradients that showed solubilities above (below) the corresponding threshold and thus are inside, (outside) the sphere. The fitting resulted in 0 wrong in and 0 wrong out points.

Solute	Solubility limit (mg mL^{-1})	δ_D (MPa$^{1/2}$)	δ_P (MPa$^{1/2}$)	δ_H (MPa$^{1/2}$)	δ_{tot} (MPa$^{1/2}$)	R_0 (MPa$^{1/2}$)	In	Out
N(Ph-2T-DCN-Et)$_3$	10	19.20	6.33	2.28	20.35	2.1	5	36
	5	19.23	7.01	2.57	20.63	2.9	9	32
	2	19.05	8.19	2.74	20.91	4.5	15	26
	0.5	19.09	8.96	3.47	21.37	6.5	24	17
PC$_{70}$BM	10	19.15	6.07	4.61	20.61	3.2	11	20
	5	19.68	6.26	5.93	21.48	4.6	13	18
	2	19.82	6.60	6.82	21.98	5.6	16	15
	0.5	19.85	7.87	7.53	22.64	6.8	21	10

A high fitting accuracy was obtained in all cases and for both materials. Neither wrong in nor wrong out points were obtained. That is, points where the predicted HSP do not correlate with expected location in/out the sphere according to measured solubility. Despite being molecules totally different in terms of molecular structure (see Figure 4.4a), the HSP for N(Ph-2T-DCN-Et)$_3$ and PC$_{70}$BM do not differ very noticeably. More in detail, the disperse contribution is slightly higher for the fullerene derivative while the polar contribution (permanent dipole-permanent dipole interactions) is a bit

higher for the small molecule. Higher differences are observed in the hydrogen bonding contribution, which is twice larger in the case of $PC_{70}BM$. Finally, higher radii are obtained for $PC_{70}BM$, which indicate bigger solubility volume in the Hansen space. This could be ascribed to lower steric hindrance of the (spherical) fullerene molecule in comparison to the star-shaped molecule.

Before seeking suitable green solvents, one extra step was performed in order to counter check the accuracy of the predicted HSP values. Specifically, we wanted to know how accurate the solubility volume was for the star-shaped molecule; this is how good the predicted R_0 radius values were. To do so, a simple experiment was carried out. An extra solvent gradient was prepared, but in this case with two non-solvents: acetone and cyclohexane. As shown in **Figure 4.7a**, these two solvents are out of the sphere that defines the solubility volume for the 0.5 mg·mL^{-1} threshold, which is in accordance to the real absolute solubility values: 0.33 mg·mL^{-1} and 3.8·10^{-5} mg·mL^{-1} for acetone and cyclohexane, respectively. In fact, the whole gradient is out of the sphere. However, some of the points are closer to the outer limit of the sphere in comparison to the extreme points (i.e. pristine solvents). Thus, real absolute solubility values along the gradient should follow this tendency.

Reassuringly, the results (**Figure 4.7b**) show higher solubility values for those intermediate points in the gradient, which correlate with the predicted behaviour. Similarly to the CB/propylene carbonate (80:20) point (Figure 4.5a), it is once more demonstrated that the absolute solubility of a molecule in a mixture of solvents can surpass the values obtained with those solvents separately. Moreover, the HSP analysis is proven to give valuable information for predicting this uncommon behaviour.
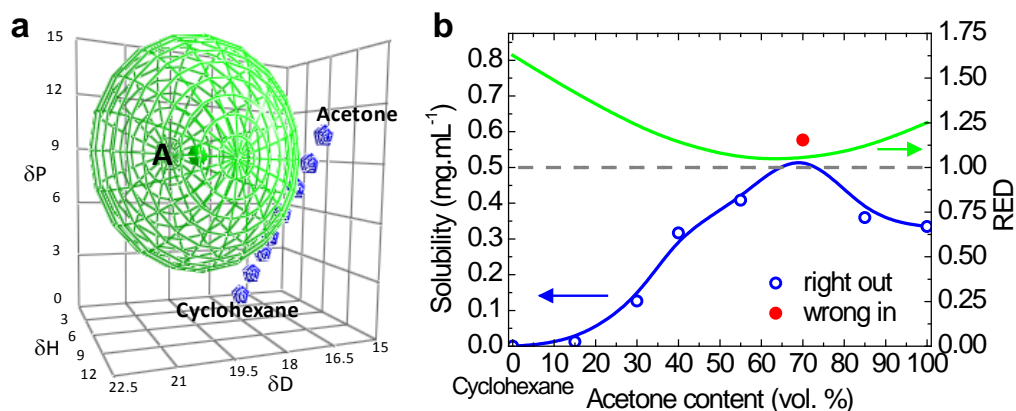
Figure 4.7. a) HSP diagram of N(Ph-2T-DCN-Et)$_3$ with the 0.5 mgmL^{-1} solubility limit (big green sphere) and the calculated acetone:cyclohexane gradient (blue spheres). b) Experimental values for solubility of N(Ph-2T-DCN-Et)$_3$ in the acetone:cyclohexane gradient (left axis) and the RED dependence on solvent composition (right axis). The blue line that connects the circles is a guide to the eye. The gray dashed line (RED=1) represents the limit of the solubility volume (green sphere in (a)).

To check how accurate the R_0 radius is, the predicted RED value for the entire gradient is compared to the measured solubilities. Since all the predicted points in this gradient are out of the sphere (RED>1), none of those points should show real values above the 0.5 mg·mL^{-1} limit. Only one (wrong) point shows slightly higher solubility; 0.58 mg·mL^{-1} was measured at the acetone:cyclohexane (70:30) mixture. This point is located, not surprisingly, where the predicted RED value (1.05, green line in Figure 4.7b) is closest to 1 (gray dashed line). Thus, despite this small deviation, it can be concluded that a good accuracy of the predicted R_0 value is obtained with the HSP analysis.

By applying this new, simple method with other non-solvent:non-solvent gradients, one could explore the accuracy of the solubility volume in other directions. This may be a relevant tool to define the real, ellipsoidal solubility volume of any molecule. However, this study would require larger material investment and experimental effort.

4.2.3. Finding suitable green solvents

The fact that both materials are close to each other in the Hansen space (see Table 4.1 and **Figure 4.8**) has a big impact in the research of suitable solvents for the N(Ph-2T-DCN-Et)$_3$:PC$_{70}$BM blend. According to the theory related to HSP, those solvents

which match the overlapping space defined by the spheres of the two materials (i.e. mutual solubility regime) would be ideal in terms of solubility.
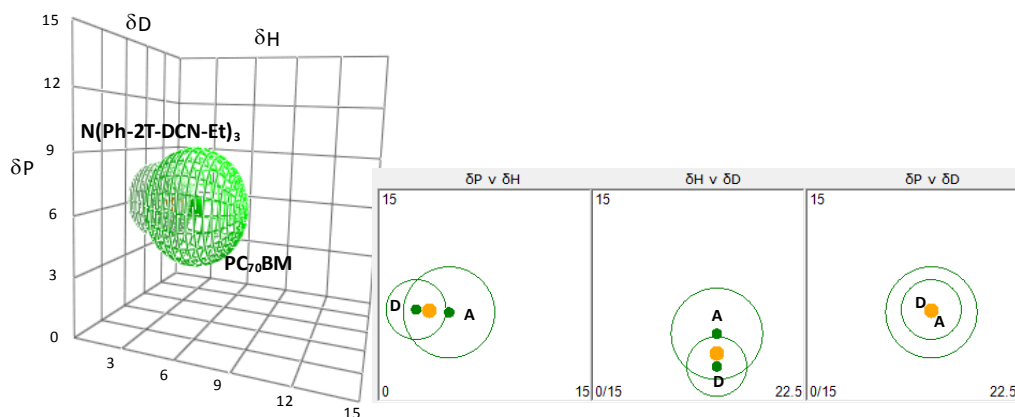
Figure 4.8. 3D and 2D HSP diagram of N(Ph-2T-DCN-Et)$_3$ (D) and PC$_{70}$BM (A). The yellow circle represents the resulting non-pondered average HSP of the blend.

A series of 50 non-halogenated solvents were selected among the entire database upon abundance, cost and/or toxicity criteria. This selection was introduced in the HSPiP software and the HSP of N(Ph-2T-DCN-Et)$_3$ and PC$_{70}$BM with the solubility limit set at 10 mgmL^{-1} were introduced as the target. A selection of 8 solvents is shown in **Figure 4.9**, while the values for a broader selection are shown in **Table 4.2**.
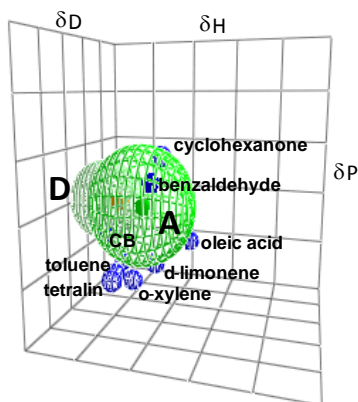
Figure 4.9. 3D plot of the distribution in Hansen space at 25°C of several non-halogenated solvents (blue circles) overlapped with the N(Ph-2T-DCN-Et)$_3$(D):PC$_{70}$BM(A) junction. Benzaldehyde is the most suitable solvent for the blend, as it fits within the junction, as reference CB does.

As it can be seen in Figure 4.9, this first approximation reveals the potential of benzaldehyde for its use as a pristine solvent, since it fits within the space defined by both N(Ph-2T-DCN-Et)$_3$ and PC$_{70}$BM spheres. The later determination of real absolute solubility of the small molecule in benzaldehyde revealed the surprisingly high value of 51.7 mg·mL^{-1}. It is important to note that benzaldehyde is closest to PC$_{70}$BM in the Hansen space, which indicates even higher solubility affinity as compared to N(Ph-2T-DCN-Et)$_3$. This can also be seen in Table 4.2 comparing the solubility distances, R$_a$. Reassuringly, the solubility of PC$_{70}$BM in benzaldehyde was found to be higher than 150 mg·mL^{-1}. However, when comparing benzaldehyde and chlorobenzene, a different correlation is observed between the solubility distance to the small molecule (3.2 MPa$^{1/2}$ and 2.1 MPa$^{1/2}$, respectively) and its real solubility in each solvent (51.7 mg·mL^{-1} and 19.2 mg·mL^{-1}, respectively). With a higher solubility in benzaldehyde, a lower distance would be expected (i.e. higher solubility affinity). These discrepancies could be derived from the assumption of a spherical shape (instead of ellipsoidal) in this simplified method. Although the latter is yet not fully understood, the high solubility in benzaldehyde of N(Ph-2T-DCN-Et)$_3$ as well as the quite similar HSP of this solvent in comparison to good solvents such as o-dichlorobenzene (DCB) and chlorobenzene suggest that benzaldehyde may be a promising candidate to replace these halogenated solvents, which are widely used in the solution processing of organic semiconductors. A solid argument for the latter is given by the low R$_a$ values between benzaldehyde and these two chlorinated solvents (2.32 MPa$^{1/2}$ and 4.60 MPa$^{1/2}$ for DCB and CB, respectively).

Table 4.2. Hansen solubility parameters of a selection of solvents. The relative distance to HSP of N(Ph-2T-DCN-Et)$_3$, PC$_{70}$BM and the junction is also shown. All units are in MPa$^{1/2}$.

Solvent	δ_D	δ_P	δ_H	R_a distance to		
				donor [a]	acceptor [a]	junction [a]
Halogenated						
chlorobenzene	19.0	4.3	2.0	2.1	3.2	2.7
o-dichlorobenzene	19.2	6.3	3.3	1.0	1.3	1.1
chloroform	17.8	3.1	5.7	5.5	4.3	4.7
p-bromoanisole	19.8	7.7	7.0	5.1	3.1	4.5
Non-halogenated						
toluene	18.0	1.4	2.0	5.5	5.9	5.5
o-xylene	17.8	1.0	3.1	6.1	6.0	5.9
tetrahydronaphthalene	19.6	2.0	2.9	4.5	4.5	5.0
mesitylene	18.0	0.6	0.6	6.4	7.2	6.7
cyclohexane	16.8	0.0	0.2	8.2	8.9	8.2
dimethyl sulfoxide	18.4	16.4	10.2	12.9	11.8	12.1
d-Limonene	17.2	1.8	4.3	6.1	5.9	5.8
β-pinene	16.9	1.6	1.8	6.6	6.9	6.6
Green solvents [b]						
acetone	15.5	10.4	7.0	9.7	8.9	8.4
2-propanol	15.8	6.1	16.4	15.7	13.6	14.4
benzaldehyde	19.4	7.4	5.3	3.2	1.5	2.7
cyclohexanone	17.8	8.4	5.1	4.5	3.7	3.2
oleic acid	16.0	2.8	6.2	8.3	7.4	7.3
propylene carbonate	20.0	18.0	4.1	11.9	12.0	11.7

[a]Calculated with the HSP obtained with the 10 mg·mL^{-1} threshold.
[b]Not containing risk phrases R50/59, relative to harmfulness to environment (EU Dangerous Substances Directive (67/548/EEC))

The second step involved the study of mixtures of 2 non-halogenated solvents. The goal is to get closer to the junction in the Hansen space. To achieve this objective one has to think about 2 solvents located at different positions in the Hansen space in a way that the resulting line that connects the two points crosses the N(Ph-2T-DCN-Et)$_3$:PC$_{70}$BM junction space as close as possible to its centre. This resulting line corresponds to the gradient of composition between these 2 solvents (**Figure 4.10a**).

Apart from this, it is also important to take other properties into account such as the miscibility between each other and their boiling point. The latter has a high impact on the drying kinetics of the wet film, which in turn may have a strong influence on the morphology of the active layer. As discussed in chapter 3, controlled drying kinetics is especially important in slow drying processes such as inkjet printing.

The simulation performed with the HSPiP software revealed the potentiality of the solvent mixture comprised by benzaldehyde and mesitylene (1,3,5-trimethylbenzene). Figure 4.10a shows the location of the 2 solvents in the Hansen space as well as some points in the gradient of the solvent composition. It is therein observed how the linking line between the two solvents gets closest to the junction at some point between the two solvents. This means that, according to Hansen theory, at that solvent composition the solubility of both materials will be higher. An illustrative way to represent this is shown in **Figure 4.10b**, where the solubility distance R_a is plotted as a function of the solvent composition.
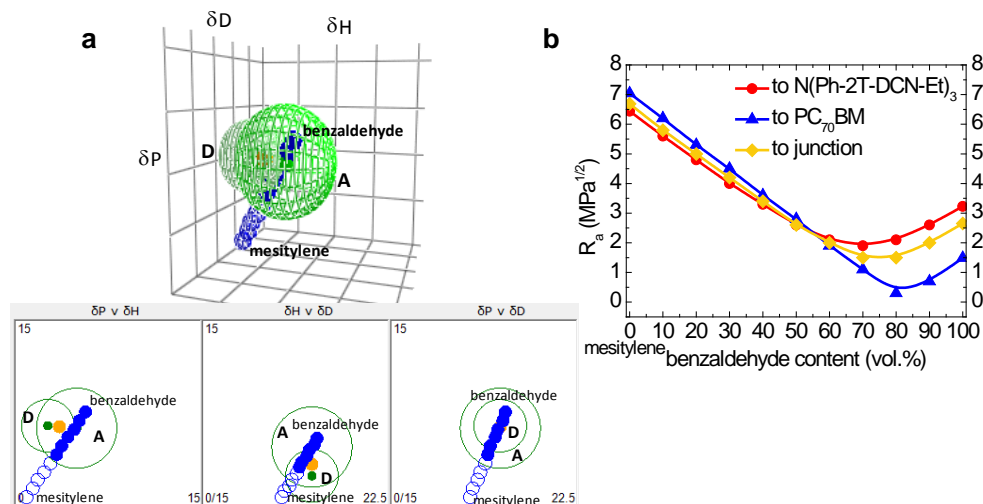
Figure 4.10. a) 2D and 3D plots of the distribution in Hansen space at 25°C of several benzaldehyde and mesitylene solvent mixtures overlapped with the N(Ph-2T-DCN-Et)$_3$(D):PC$_{70}$BM(A) junction. The blue circles between the two solvents correspond to representative solvent compositions of the gradient. It is seen how some points of the gradient are closer to the junction (yellow circle) in comparison to pristine solvents. b) Relative distance in Hansen space (R$_a$) as a function of benzaldehyde content in the benzaldehyde:mesitylene solvent mixture.

In accordance to this, a minimum R$_a$ distance to both N(Ph-2T-DCN-Et)$_3$ and PC$_{70}$BM as well as to the junction between them is seen in Figure 4.10b and with a 70-80% of benzaldehyde content.

In the following section the benzaldehyde:mesitylene (80:20) mixture and pristine benzaldehyde are used for the fabrication of OPV devices and the relationship between solubility and photovoltaic performance is discussed.

4.2.4. OPV fabrication with green solvents

In order to assess the suitability of the proposed green solvent systems, reference devices were fabricated with chlorobenzene and mixtures of chlorobenzene with 2% of 4-bromoanisole additive, as described in reference [122]. The structure of the devices was glass/ITO/PEDOT:PSS/N(Ph-2T-DCN-Et)$_3$:PC$_{70}$BM/Ca/Ag. In this section, we performed some changes respect to the general recipe (chapter 2) for OPV fabrication, as described below. First, laser patterned ITO-coated glass substrates[124] were used as back contact. Secondly, PEDOT:PSS (Clevios P VP Al4083 from Heraeus) was diluted in 2-propanol (1:3 volume ratio) before being doctor bladed, using general

conditions described in chapter 2. The active layer was then deposited by doctor blading a 2 wt% blend solution of N(Ph-2T-DCN-Et)$_3$ and PC$_{70}$BM (1:2 wt ratio) in the solvent system. The 12 mm·s^{-1} of blade speed, 60 μL of solution and 400 μm of gap resulted in a thickness of 80–90 nm for the active layer. Then, the samples were transferred into a nitrogen-filled glovebox where Ca (15 nm)/Ag (85 nm) electrodes were thermally evaporated at 3×10^{-6} mbar through a shadow mask, defining an active area of 10.4 mm^2. Finally, the devices were encapsulated with a glass cap using an ultraviolet curing epoxy resin (ELC 2500) and 2.5 min exposure to UV radiation. Noteworthy, the temperature of the doctor blade equipment stage was adjusted for each solvent system according to their different vapour pressures in order to achieve similar drying times (< 5s). Therefore, solutions based on chlorobenzene with 0% and 2% of 4-bromoanisole additive were coated at 65°C, as described in reference [122], whereas those based on benzaldehyde and benzaldehyde:mesitylene (80:20) were coated at 80°C.

The statistic spreading of the main performance parameters extracted from at least 15 solar cells for each solvent system are depicted in **Figure 4.11**. Reassuringly, the green solvent formulations result in a similar good performance as the corresponding chlorinated solvents, with practically negligible differences in all performance parameters. There might be a tendency for improvement in PCE but it is not statistically significant. These comparable performances obtained with green solvents and halogenated formulations correlate with the theoretical solubility analysis previously described. Thus, the applicability of the Hansen theory in the design of green formulations is proved. Moreover, it is demonstrated that halogenated solvents can be successfully replaced without losing efficiency by properly studying the solubility characteristics of the materials and adjusting the drying conditions. We note that the here reported values for the reference CB cells are as high as those reported in the literature.[122]
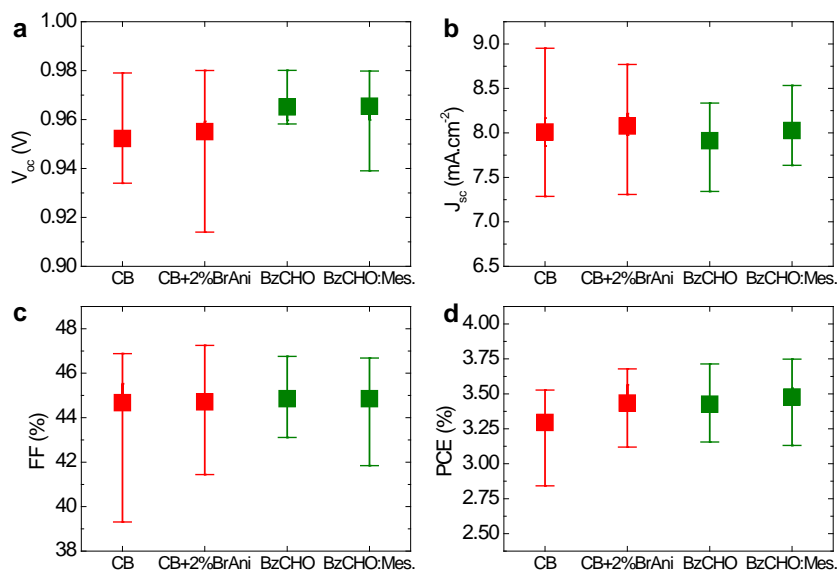
Figure 4.11. OPV performance parameters of devices based on chlorobenzene (CB), chlorobenzene with 2% of p-bromoanisole (CB+2% BrAni), benzaldehyde (BzCHO) and benzaldehyde:mestiylene (80:20) system (BzCHO:Mes.). a) V_{oc}, b) J_{sc}, c) FF and d) PCE.

The resulting J-V curves from the best performing devices for each solvent system are plotted in **Figure 4.12**, and the corresponding parameters are summarized in **Table 4.3**. As far as we know, these are the best PCE values obtained via green solvents processing reported up to now.
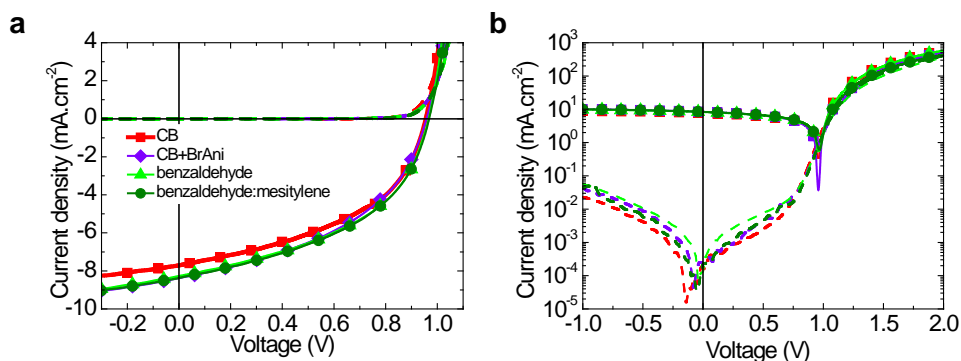
Figure 4.12. J-V curves of best performing devices based on chlorobenzene (CB), chlorobenzene with 2% of p-bromoanisole (CB+BrAni), benzaldehyde and benzaldehyde:mesitylene (80:20) under AM 1.5G 100 mW cm^{-2} illumination (solid lines) and in dark conditions (dashed lines). a) linear and b) logarithmic scales.

It is clearly visible how the J-V curves are practically overlapped, besides small differences with the sample processed from chlorobenzene, which showed lower efficiency. This very similar performance, in particular the J_{sc} and FF values, suggest that an approximately comparable morphology is maintained throughout the film in all the samples, regardless of the type of solvent system used. The almost overlapping absorption and external quantum efficiency spectra (**Figure 4.13** a and b, respectively) of devices fabricated with the different solvents supports this hypothesis. This is further confirmed by atomic force microscopy images (**Figure 4.14**), which indicate that the surface topology of the films fabricated with the four solvent systems (CB, CB+2%BrAni, benzaldehyde and benzaldehyde:mesitylene) are very similar and consist of a fine mixing of the two components coupled to a low surface roughness (RMS <1 nm in all cases).

Table 4.3. OPV performance parameters of best performing devices based on different solvent systems.

Solvent system	V_{oc} (V)	J_{sc} [a] (mA cm^{-2})	J_{sc} [b]	FF (%)	PCE [a] (%)	PCE [b]
chlorobenzene	0.96	7.71	7.56	46.11	3.41	3.34
chlorobenzene + 2% BrAni	0.96	8.32	7.95	45.22	3.61	3.45
benzaldehyde	0.96	8.27	8.06	46.75	3.71	3.62
benzaldehyde:mesitylene 80:20	0.96	8.37	8.35	46.68	3.75	3.74

[a]Measured under AM1.5G 100 mW cm^{-2} illumination.
[b]Calculated from EQE spectra.
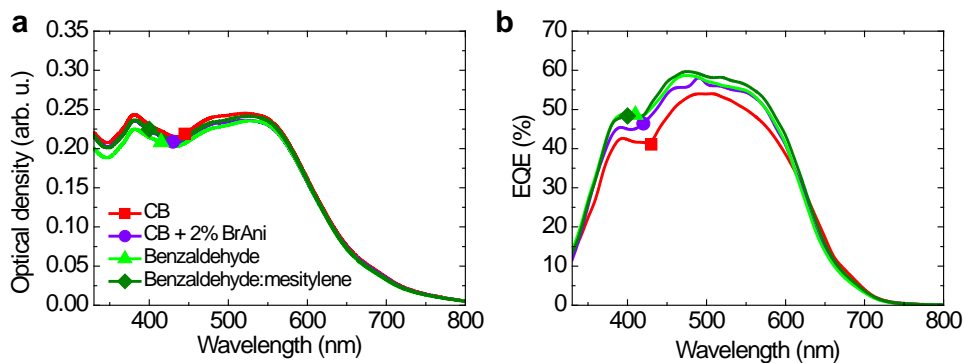
Figure 4.13. a) Optical density and b) EQE spectra of best performing devices based on chlorobenzene (CB), chlorobenzene with 2% of p-bromoanisole, benzaldehyde and benzaldehyde:mesitylene (80:20) mixture.
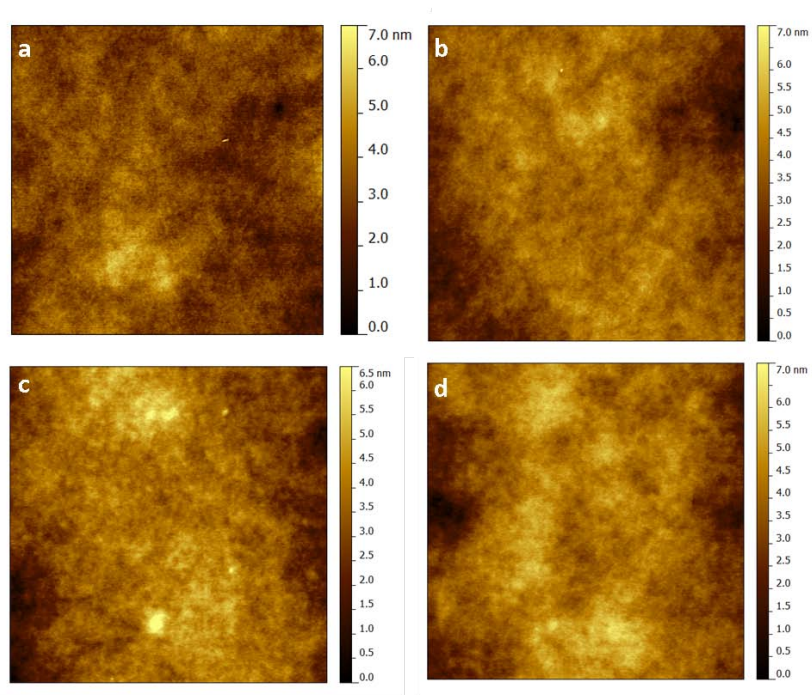
Figure 4.14. Contact mode AFM surface scans (5 x 5 μm²) of N(Ph-2T-DCN-Et)₃:PC₇₀BM films deposited on glass from a) chlorobenzene (RMS = 0.72 nm), b) chlorobenzene + 2% vol. BrAni (RMS = 0.87 nm), c) benzaldehyde (RMS = 0.91 nm) and d) benzaldehyde:mesitylene (80:20) (RMS = 0.97 nm).

On the other hand, pristine benzaldehyde already shows a high solubility for both components, offering the possibility to reach similar device performance compared to

halogenated solvent systems. By introducing a second solvent, mesitylene, with the simulated optimum blend composition, the PCE only improves slightly. The effect of the additional increase in solubility seems not to have a major effect in device performance in this case. In other words, our experiments suggest that there is a minimum solubility required for the ink to be processable and lead to good performance, while further increases in solubility may not be expected to result in major benefits. Therefore, any additional mixing that keeps the solubility above the minimum can be employed to assist the drying kinetics of the specific deposition technique employed. However, under a strict environmental point of view, pristine benzaldehyde is greener than the mixture with mesitylene, and thus we would propose using only one solvent when possible.

4.3. ALTERNATIVE SOLVENTS FOR LOW BAND GAP POLYMERS

4.3.1. Why polymers?

As explained in chapter 1, the great progress made in OPV research has been always intimately linked to the development of conjugated polymers. Their low-cos potential encourage further research. The main advances have been accomplished thanks to polymer engineering, including lowering the band gap and also combining donor and acceptor units. The former may increase the V_{oc} while the latter may result in better charge transport, which results in higher J_{sc}. The priority has been, therefore, to enhance OPV performance.

Another important aspect that polymer engineering should cover is their solution processability. The structural properties of a polymer govern its degree of solubility. In particular, the degree of polymerization, the chain length of the aliphatic groups, the polarity of the substituents, backbone rigidity, polymer regioregularity, and intermolecular interactions may affect the solubility behaviour of the polymer.[125] Finally, long-term stability of polymers is desirable as well.

In summary, the properties that conjugated polymers should fulfil are (1) good solubility, (2) high molecular weight, (3) HOMO level around –5.4 eV, (4) LUMO level around –3.9 eV, (5) high hole mobility, (6) optimal morphology, and (7) long-term stability.[34]

4.3.2. Study of solubility

The objective of this whole section is to find and use alternative (green) solvents for the processing of low band gap polymers. As in the previous section, the first step consists in studying the solubility behaviour of the molecules that need to be dissolved. Herein, two low band gap polymers are studied, namely PCDTBT and PTB7 (see Figure 1.16). These commercially available materials exhibit some of the highest reported PCE values (see Table 1.2 in chapter 1)

Many conjugated polymers include side chains that promote solubility. Lower solubility values are however expected in comparison to small molecules due to entropic reasons. Moreover, molecular engineering applied to conjugated polymers has not considered so far solubility in green solvents, unfortunately. The latter can become a critical drawback for the upscalability of polymer solar cells. Even so, the motivation to turn towards green solvents is kept in this section, in the same manner as in previous section.

The first challenge we have to face is related to the determination of HSP. The Binary solvent gradient method requires a minimum estimated amount of material of ~300 mg. Taking into account the high price of these low band gap polymers, this quantity is unrealistic for the solubility study. Instead, we propose an alternative method.

What determines the HSP of a molecule is the contribution of their different chemical interactions. Therefore, two molecules with similar HSP are likely to show comparable chemical behaviour and parallel solubility. Consequently, using the HSP of known good (halogenated) solvents for the polymers, one can search other solvents (mixtures) that match as close as possible those HSP[126] (see **Figure 4.15**). Chlorobenzene (CB) plus the addition of 1,8-diiodooctane (DIO) have been often used for processing PTB7,[127] while o-dichlorobenzene (DCB) is the solvent of choice for spin coated PCDTBT.[128]

Looking at the huge solvent database provided in the HSPiP software[115] and keeping the green criteria, we found that benzaldehyde has similar HSP compared to DCB while the benzaldehyde:mesitylene (1:1) mixture is nearly in the middle between CB and DIO. Tetrahydrofuran (THF) was also considered as it can relatively dissolve PCDTBT.[40] By mixing THF with mesitylene, the distance to DCB in the Hansen space is maintained while, most importantly, the vapour pressure of the solution is

decreased. This is of vital importance for accomplishing specific ink requirements in certain deposition techniques such as inkjet printing.
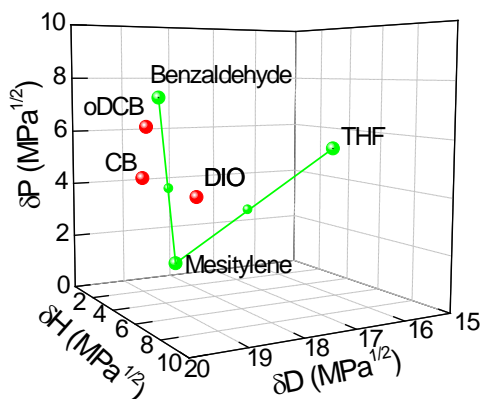
Figure 4.15. Hansen solubility parameters of halogenated (red circles) and non-halogenated solvents (green circles). The smaller circles located on straight lines correspond to the studied mixtures.

Based on these findings, the real absolute solubility of the two polymers in different solvent systems was determined by UV-Vis characterization of saturated solutions, in the same manner as in the previous section. **Table 4.4** shows that the predicted solvent mixtures with non-halogenated solvents present reasonably good solubility for the two polymers. In the case of PCDTBT, a solubility of 14.4 mg·mL^{-1} was measured for the tetrahydrofuran:mesitylene (1:1) mixture, compared to 25.3 mg·mL^{-1} obtained with 1,2-dichlorobenzene. These values are high enough for solution processing the ~70 nm active layer, taking into account that the donor to acceptor ratio is 1:4 and the blend concentrations needed are 30, 25 and 8 mg·mL^{-1} for spin coating , doctor blade and inkjet printing, respectively, in these particular solution systems. The low value obtained with pristine benzaldehyde (0.8 mg·mL^{-1}) was a bit surprising, given that this solvent is quite close to DCB in the solubility space, as indicated by the R_a distance (2.32 MPa$^{1/2}$). This suggests that the HSP of the polymer may be located further from benzaldehyde. In turn, the measured solubility is much larger with THF:mesitylene mixture, although the R_a distance to DCB (R_a = 4.85 MPa$^{1/2}$) shows a twofold increase with respect to pristine benzaldehyde. These unexpected values are a consequence of using the chlorinated solvents as the target rather than the HSP of the polymer. Also the solubility volume could differ from spheroid shape. In the case of PTB7, we found

it to be more soluble in both chlorinated and non-chlorinated solvent systems. Strictly in terms of solubility, these results show that HSP analysis is of valuable, qualitative help for finding alternative solvents also in the case of low band gap polymers. Of course it would have been more accurate to work with the HSP of the polymers, but we currently discard this option due to its high cost.

Table 4.4. Determined absolute solubility of low band gap polymers at room temperature in different solvent systems and R_a distance from non-halogentaed to reference chlorinated solvents.

Solute	Solvent	Solubility (25ºC) $mg \cdot mL^{-1}$	R_a to chlorinated solvent $MPa^{1/2}$
PCDTBT	DCB	25.3	–
	Benzaldehyde	0.8	2.32
	Benzaldehyde:mesitylene (3:2)	11.8	1.79
	THF:mesitylene (1:1)	14.4	4.85
PTB7	CB	124.2	–
	Benzaldehyde:mesitylene (1:1)	39.6	1.20

The absorption spectra of solutions prepared with halogenated and non-halogenated solvent systems are shown in **Figure 4.16**. In agreement with the solubility determination, there is a strong overlap in the absorption of both materials dissolved in halogenated and green solvents.
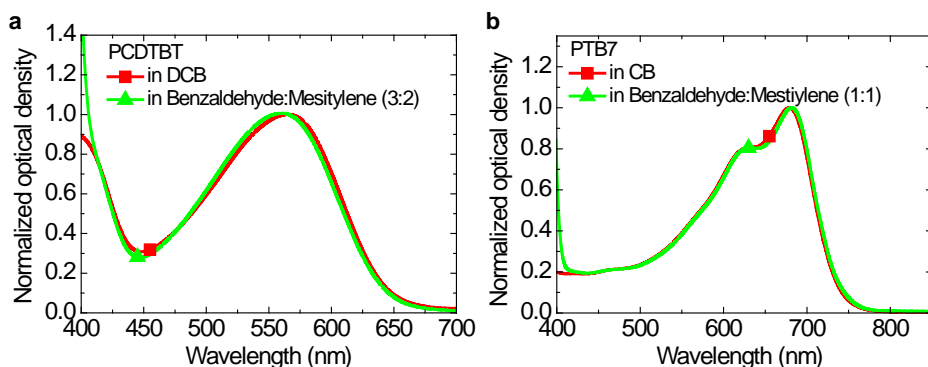
Figure 4.16. Optical density spectra of a) PCDTBT and b) PTB7 dissolved in halogenated (red line) and non-halogenated (green line) solvents for diluted solutions with 2-7 µg/mL concentration.

However, in order to consider a halogen-free solution to be successful for active layer processing, other issues besides solubility are needed as well. Particularly important in bulk heterojunction systems with donor:acceptor blends is an adequate combination of drying kinetics and selective solubility of each material, which will eventually lead to optimal layer morphology and OPV performance. This can require laborious procedures, especially when the system becomes more complicated as it does with mixtures of solvents.

4.3.3. OPV fabrication with non-halogenated solvents

The non-halogenated solvent mixtures that showed higher solubility (Table 4.4) were tested for OPV fabrication. Since working under ambient conditions is also another key factor for low-cost processing of OPVs, both PEDOT:PSS and active layer were prepared in air conditions. In this section the photovoltaic performance is compared to reference reported results with devices prepared in inert conditions. The use of different processing techniques is also discussed. The complete structure of the devices was ITO/PEDOT:PSS/polymer:PC$_{70}$BM/LiF/Al.

4.3.3.1. PTB7 based devices

For the preparation of devices made by spin coating, the recipe used by Liang and co-workers was followed.[127] Although higher efficiencies have been reported with this polymer, the choice of this reference is due to the similarity with our standard device configuration and processing conditions. However, the exception of working under ambient conditions, instead of using nitrogen filled glovebox for the active layer

deposition, resulted to be critical. As seen in **Figure 4.17** and **Table 4.5**, the performance of the devices made under air conditions is noticeably lower in comparison to reference device: a simultaneous decrease in V_{oc}, J_{sc} and FF is observed. Considering that the same materials and recipe were employed, we can ascribe this to a negative effect of working under ambient conditions.
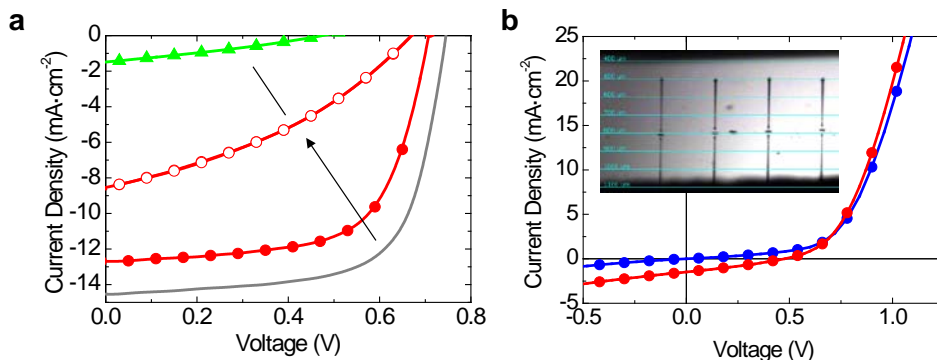
Figure 4.17. J-V curves of PTB7:PC$_{70}$BM based devices processed in air conditions by a) spin coating and b) inkjet printing. The grey, solid curve in (a) corresponds to the reference device processed in nitrogen atmosphere (reproduced from reference [127]); devices prepared in air conditions from CB:DIO with short (< 3 min, filled circles) and long (~30 min, empty circles) exposure to air and from the benzaldehyde:mesitylene mixture (green triangles) show gradual degradation of efficiency. Inkjet printing devices showed poorer performance, although a good jettability was achieved (inset in (b) shows a caption of drop ejection). A bad rectification is obtained in curves in both dark (blue) and illuminated (red) conditions. Some of the spin coated devices were prepared by Dr. Marco Stella.

What is relevant is that the time of exposure to air during wet processing has a big impact on the performance of the device. While quite high efficiency was obtained (PCE = 5.86%) with minimized air exposure (<30 s after spin coating), the PCE dropped down to 2.12% when the sample was kept for a longer time under exposure to air (>15 min). In agreement to this, the sample processed by ikjet printing, which implies longer processing time (about 6 min) and was not rapidly transferred to the glovebox, shows a very low efficiency (PCE = 0.21%, Figure 4.17b). Therefore, it can be concluded that PTB7 is highly sensitive to ambient conditions. This is in agreement with Soon and co-workers, who found that PTB7 has an efficient singlet oxygen production from triplet excitons.[129] This is a highly damaging specie, which hinders polymer photostability. This is a big inconvenience for the upscalability of OPVs using this polymer.

Table 4.5. Performance parameters of OPV devices based on the PTB7:PC$_{70}$BM blend.

Processing technique	Solvent	V_{oc} V	J_{sc} mA·cm^{-2}	FF %	PCE %
Spin coating	CB:DIO*	0.74	14.5	69	7.4
	CB:DIO[a]	0.71	12.69	65	5.86
	CB:DIO[b]	0.67	8.54	37	2.12
	Benzaldehyde: mesitylene (1:1)	0.48	1.50	29	0.21
Inkjet printing	CB:DIO	0.48	1.45	30	0.21

*From reference [127]
[a]with shorter exposure to air
[b]with longer exposure to air

On the other hand, the use of benzaldehyde:mesitylene (1:1) solvent mixture resulted in a dramatic decrease in photovoltaic performance (PCE = 0.21%), despite providing high solubility. In spin coating process the drying time was of the same order as for halogenated solvents. This is the proof that solubility is not the unique requirement for efficient solution processing of the active layer, with fine tuned microstructure being equally important. In fact, the use of DIO additive has been demonstrated to facilitate a more uniform morphology, otherwise unaffordable with pristine CB. In this case, the additive modifies the miscibility between the components, resulting in a dramatic decrease in domain size.[130] Therefore, the proposed green formulation may not be adequate in terms of selective solubility to address optimal morphology.

4.3.3.2. PCDTBT based devices

In the same manner as before, a recipe with normal structured OPV device was followed for the fabrication of PCDTBT based solar cells.[128] In contrast to PTB7, higher stability was observed this time. The time of exposure to air was found to be not as critical as for PTB7. However, the 4.61% of PCE is again lower compared to the reference device prepared in controlled atmosphere conditions (**Figure 4.18**). Moreover, the usage of green solvents resulted in lower efficiency.
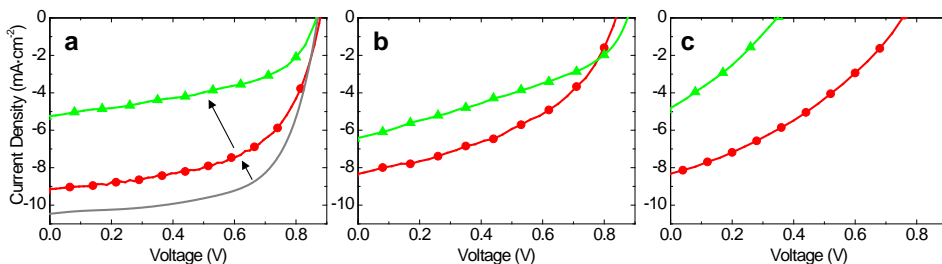
Figure 4.18. J-V curves of PCDTBT:PC$_{70}$BM based devices processed in air conditions by a) spin coating and b) doctor blade coating and c) inkjet printing. The grey, solid curve in (a) corresponds to the reference device processed in nitrogen atmosphere (reproduced from reference [128]).

In spite of this, further tests with PCDTBT were performed using alternative deposition techniques such as doctor blade and inkjet printing, as they stand closer to large-scale processing. The coating parameters were adjusted in order to reach similar active layer thicknesses (~70 nm). However, the results (Figure 4.18) show that poorer performances are obtained with these techniques. We ascribe this to a non optimised layer morphology derived from different drying kinetics. We would like to note that basic optimisation was carried out for processing the PCDTBT:PC$_{70}$BM (1:4) blend. Spin coated active layers were processed at 600 rpm for 90 s from solutions with 30 mg/mL concentration. In the case of doctor blade coating, substrate temperature was set to 30 ºC and 50 ºC, blade speed was 10 mm/s and 80 mm/s, 200 µm and 400 µm gap were used and 30 µL and 50 µL of 28 mg/mL and 24 mg/mL solutions were disposed for halogenated and non-halogenated solvent systems. For inkjet printing, the conditions differed significantly between halogenated and green solvents: 3 jets were used to print at 25 µm and 20 µm of drop spacing, substrate temperature was set to 45 ºC and 25 ºC, firing voltage was set to 37 V and 12 V to reach 4.1 m/s and 4.6 m/s of drop ejection speed and the waveform of the piezoelectric actuator was adapted to ink properties. In all cases an annealing step (15 min at 75 ºC) was performed afterwards, in inert atmosphere.

The biggest difference in comparison to PTB7 devices is that in this case the V$_{oc}$ is more or less maintained at the expected value (V$_{oc}$ = 0.88 V), even with the green solvent system, when using spin coating and doctor blade (see also **Table 4.6**). Primarily with these two techniques, both the J$_{sc}$ and the FF are responsible of lowering the performance of solar cell devices, which directly points to the active layer: according to the results, this fall can be attributed partly to active layer degradation

(comparing reference devices to air processing with chlorinated solvents). When unsuitable drying kinetics results in too large phase separation, the V_{oc} is also negatively affected due to worse series and/or parallel resistance. The devices processed by inkjet printing clearly exemplify this.

Table 4.6. Performance parameters of OPV devices based on the PCDTBT:PC$_{70}$BM blend

Processing technique	Solvent	V_{oc} V	J_{sc} mA·cm^{-2}	FF %	PCE %
Spin coating	DCB*	0.88	10.47	65	6.03
	DCB	0.88	9.19	57	4.61
	THF:mesitylene (1:1)	0.86	5.25	49	2.23
Doctor blade	DCB	0.84	8.35	44	3.09
	THF:mesitylene (1:1)	0.87	6.42	38	2.11
Inkjet printing	DCB	0.75	8.28	36	2.22
	THF:mesitylene (1:1)	0.35	4.81	30	0.50

*from reference [128]

On the other hand, similar J_{sc} values are obtained with DCB processed by the three techniques. As said above, the processing conditions were adjusted in order to achieve the same active layer thickness (~70 nm). Even though similar charge collection is obtained, the performance is penalized by the poorer morphology obtained with doctor blade and more markedly with inkjet printing, as deduced from the gradual decrease in FF: 57%, 44% and 36% for spin coating, doctor blade and inkjet printing, respectively.

This brief set of experiments evidence three aspects that conjugated polymer engineering need to address. Firstly, high stability is required for polymers being attractive for industrial production. They should be stable in air and in the whole fabrication process, including solution preparation, coating step, drying process and in the dried film. Secondly, the polymers should be soluble in non-toxic solvents. Thirdly, this minimum solubility is not enough to ensure that optimal active layer morphology is obtained; further and specific optimisation is needed, in relation to the coating technique and the materials used.

Regarding this last point, a careful HSP analysis could give insights into the suitability of alternative solvent systems in terms of selective solubility of donor and acceptor materials. It thus would be interesting to determine the HSP of the polymers and

studying the relations (i.e. R_a distances) to $PC_{70}BM$ and to mixtures of green solvents. Moreover, the variation of the composition of solvent blends upon drying due to differences in vapour pressure can be analysed with the HSPiP software. The latter might be very useful to somehow predict eventual, vertical phase separation.

4.4. CONCLUSIONS

In this chapter a big emphasis on the importance to move towards green solvents has been set. We have shown how the Hansen solubility parameters analysis can offer valuable information about the suitability of solvents for each particular solute; either if it is a small molecule or a polymer.

In particular, we have used the binary solvent gradient method to determine the HSP of two different materials: the small molecule, star-shaped N(Ph-2T-DCN-Et)$_3$ and the fullerene derivative $PC_{70}BM$. A counter check tool has been proposed in this work to study the accuracy of the predicted radius of the solubility sphere. This method consists in studying a binary solvent gradient between two non-solvents strategically located in the Hansen space with respect to the molecule under study. For the star-shaped molecule this method proved quite good accuracy of the predicted radius.

The HSPs of both materials have then been used to predict suitable green formulations in terms of solubility for the solution processing of active layers. We first have focused on pristine solvents and have found benzaldehyde to be the most suitable solvent. Then, we have developed inks that included mixtures of two solvents (benzaldehyde:mesitylene (80:20)) in order to obtain a system with the closest solubility to the junction between the donor and acceptor solubility spheres (according to the R_a distance in the Hansen space). Finally, solar cells have been fabricated using these green formulations, resulting in similar power conversion efficiencies with both benzaldehyde (3.62%) and benzaldehyde:mesitylene mixture (3.74%) comparable to halogenated solvent systems (3.45%).

In a second step, we have applied the HSP analysis to find alternative solvents for two efficient low band gap polymers: PCDTBT and PTB7. Unfortunately, the HSP of these polymers have not been determined due to the high cost. Instead, an approximation has been performed, based on finding solvent systems in the Hansen space that are located closely to halogenated solvents like CB or DCB, commonly used

for these materials. As a result, solubilities of 14.4 mg·mL^{-1} (for PCDTBT) and 39.6 mg·mL^{-1} (for PTB7) have been determined using two non-halogenated solvent systems.

Finally, these non-halogenated formulations have been employed in the fabrication of OPV devices under ambient conditions, which is another important objective for the industrial viability of polymer solar cells. We have shown how these two critical parameters can affect the performance of OPVs. A clear decrease in PCE has been obtained when processing in air conditions. The latter has been found to be especially critical for PTB7, which is highly unstable. Despite the good solubility achieved with non-halogenated solvents, poorer efficiencies have been obtained in all cases in comparison to halogenated counterparts. It has been concluded that other important aspects such as selective solubility or appropriate drying kinetics have to be taken into account during optimisation in order to achieve suitable blend morphology. On the other side, it is evident that the transfer towards both halogen-free and large-scale processing is not trivial.

CHAPTER 5

ITO-free electrodes

Abstract

The excellent properties of indium tin oxide (ITO), in terms of transparency and conductivity, are the reason why this material is widely used as a transparent electrode in organic photovoltaics and in many other applications. However, it has been identified as a major contributor to the cost of an OPV module, due to the high energy needed for the sputtering and patterning processes as well as to the low abundance of the indium element. Additionally, reported troubles such as cracking or delamination and conductivity losses advise against its use in flexible devices. Therefore, finding alternative transparent conductors is a major necessity.

In this chapter we study one possible alternative: metallic grids in combination with a transparent polymer conductor. In particular, we show how embedding such structures within the substrate leads to a smoother surface compared to traditional protruding grids, which in turn improves the topology of successive layers. The latter results in an enhancement of solar cell efficiency, mostly due to enhanced fill factor and reduced shunting. The whole optimisation process is presented, including the design, estimation of losses, fabrication and embedding of the grids using reverse nanoimprinting transfer. Finally, the fabrication of ITO-free OPV devices experimentally confirms the predictions. The suitability of such structures is therefore demonstrated.

5.1. CURRENT ALTERNATIVES TO ITO. STATE OF THE ART

Many efforts are currently being carried out in seeking adequate substitutes to ITO electrode. The goal is to find a cost-effective material with high conductivity, transparency and flexibility. Several ITO-replacement transparent conductors have been reported up to now. Angmo et al. classified the alternatives in four different groups: i) highly conductive polymers, ii) metals, iii) combinations of polymer and metal, and iv) carbon based conductors.[131] Other interesting reports compare these transparent conductors revealing their strengths and weaknesses, evidencing the increasing interest that this topic has attracted in the last few years.[132,133] However, more data and experimental work is still needed to determine whether a unique alternative or a combination of some of them will be predominant in the near future.

In the field of OPVs, remarkable results have been obtained with these alternative electrodes. From the first group, the most widely used transparent semiconductor polymer is the poly(3,4-ethylenedioxythiophene), doped with poly(styrenesulfonate) (PEDOT:PSS)[134,135] or deposited from vapour phase.[136] The second group (metals) can be subdivided into metal nanowires (NWs)[137,138] and ultrathin metal layers.[139–141] A combination of polymer and metal structures is also proposed, typically in the form of grids covered by a PEDOT:PSS layer.[142,143] Finally, some examples of carbon nanotubes (CNTs)[144,145] and graphene[146,147] films are also present in recent literature. Comprehensive review works on this field can be found elsewhere.[131] A non-exhaustive selection of representative results obtained with these different electrode alternatives is shown in **Table 5.1**. In order to make a fair comparison, this literature data collection is taken from normal structured OPV devices with identical active layer materials: anode/(PEDOT:PSS)/P3HT:PCBM/cathode.

Table 5.1. Alternatives to ITO. Representative electrodes and performance results in standard OPV device: structure: anode/(PEDOT:PSS)/P3HT:PCBM/cathode. ρ: sheet resistance; T: transmittance; V_{oc}: open circuit voltage; J_{sc}: short circuit current density; FF: fill factor; PCE: power conversion efficiency.

	Material	ρ (Ω/sq)	T (%)	Flexibility[a]	Area (cm²)	V_{oc} (V)	J_{sc} (mA·cm⁻²)	FF (%)	PCE (%)	$\dfrac{PCE_{ITO-free}}{PCE_{ITO}}$	Ref.
Metal oxide	ITO[b]	8-12	84	Low	0.15	0.63	9.5	68	0.95-5	-	134-147
Polymer	PEDOT:PSS	67	80	High	0.09	0.59	9.29	65	3.56	0.86	135
Metal	Metal NWs	12	85	High	0.07	0.42	2.8	25	0.3	0.07	137
	Ultrathin metal layers	NA	~50	Medium	0.09	0.58	7.12	61	2.52	0.72	140
		5	~30	Medium	35.5	6.8	5.8	40.3	0.44	NA	141
Metal + PEDOT:PSS	Metal NWs	12	85	High	0.07	0.62	10.4	65	4.2	1	136
	Metal grid	1	~70	Medium	4	0.54	6.25	57.1	1.93	2.03	142
		1	75	Medium	121.5	4.76	5.45	55.6	1.05	NA	143
Others	CNTs	60	~70	High	0.1	0.58	11.5	48	3.1	0.86	145
	Graphene	610	87	High	NA	0.60	9.03	48	2.6	0.68	146

[a] Qualitative comparison of the flexibility of the material itself, taking into account the results presented in the references cited

[b] Sheet resistance and transparency values shown here are taken from reference[148]

In all cases an inverse correlation between conductivity and transparency is observed. Thus, a compromise is required to reach the highest OPV performance. From the data presented in Table 5.1, one can see that PEDOT:PSS as well as its combination with metal NWs and CNTs are at this moment the materials performing most closely to ITO in terms of efficiency. However, when each structure is compared to its relative ITO reference ($PCE_{ITO-free}/PCE_{ITO}$ column) an interesting observation emerges: the combination of metal and PEDOT:PSS is a very successful ITO replacement, even doubling efficiency for large active areas. On the other hand, graphene still has too high sheet resistance, whereas transparency is the limiting factor for ultrathin metal layers. Moreover, all alternative systems exhibit higher flexibility compared to ITO. High flexibility is obtained with polymeric or nanostructured-based films, while metallic layers or grids exhibit moderate flexibility. Finally, a big difference is observed between the areas of tested devices.

So far, metal grids have led to the largest OPV cell area with still reasonably good performances. Not surprisingly, they show the lowest sheet resistance (1 Ω/sq), which indicates that conductivity becomes a crucial factor for large area OPV applications.[147] Therefore, metal grids may be a good choice for large-scale OPVs when very high flexibility is not required. It is indicative that the first built OPV-based solar park uses such structures in both electrodes.[149] Major advantages such as significant reduction of material consumption and the possibility of recycling the metallic grid at the end of the module lifetime,[150] strongly motivate further research in these type of electrodes. Additionally, OPV technology (and printed electronics in general) is expected to become soon more competitive with less expensive materials such as copper. Indeed, nanoparticle copper inks have been demonstrated[151] and the first commercial inks are already available.[152]

5.2. METALLIC GRIDS

Different approaches for grid deposition have been successfully demonstrated in OPVs, including screen printing,[142] inkjet printing,[153] lithography[154] and thermal evaporation.[155] Even semi-transparent organic solar cells have been reported using metallic grids as both anode and cathode.[156]

Metal grids must be accompanied by a layer of a transparent conducting material such as PEDOT:PSS in order to allow transport of charges photogenerated in between the

grid lines towards the current collecting grid electrode. It should be noted that the reported low values of sheet resistance in this structure correspond to the bulk metal surface instead of the combined grid/PEDOT:PSS layer, since macroscopic transport measurement will be dominated by the high conductivity of the metal.

In order to get both high conductivity and transmittance with such structures, a compromise should be found between resistive losses and shadowing losses. The resistance of the Ag grid/PEDOT:PSS electrode should be kept as low as possible while at the same time the Ag grid surface coverage should be as small as possible to enable maximum solar light incidence in the active layer. Multiple grid configurations can be designed depending on several parameters, namely the sheet resistance of the PEDOT:PSS layer and both the bulk resistance and the 3D geometry of the Ag lines.

5.2.1. Why embedding?

A typical problem in metallic grid architectures lies in the difficulty to over-coat homogeneously these grid lines with thin layers of PEDOT:PSS and active layer, which leads to short circuits or current leakage in the best case. Additionally, in order to fully over-coat metallic grids, subsequent PEDOT:PSS layer is often generously thickened, resulting in losses in transparency. As an example, **Figure 5.1** shows a simulation of how the transmission of glass/PEDOT:PSS varies with the thickness of the polymer (simulated ellipsometric measurement).
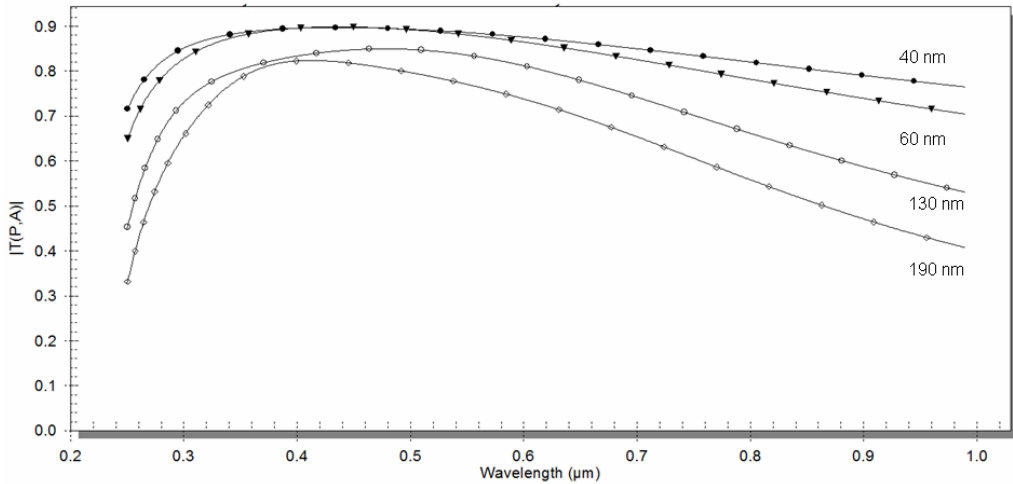
Figure 5.1. Simulated transmission of glass/PEDOT:PSS substrates for different PEDOT:PSS layer thickness. These data were determined by Dr. Mariano Campoy-Quiles.

One solution is to deposit the PEDOT:PSS layer by rotary screen printing and in registry to the metallic grid structure.[156] In this approach the PEDOT:PSS pattern is the negative image of the grid structure, thus thin PEDOT:PSS films can be employed with reduced risk of shorts. An alternative solution may be to embed these grids within the substrate,[142] which may allow to deposit PEDOT:PSS on a flattened surface, while keeping optimal PEDOT:PSS layer thickness. Cross sectional schematic views of normal structured OPV devices are shown in **Figure 5.2**.
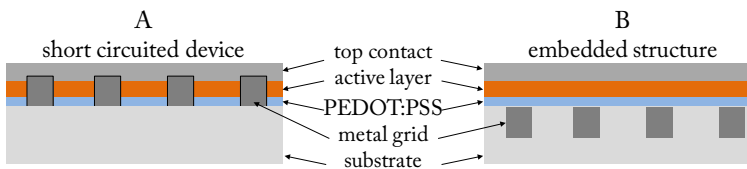
Figure 5.2. Schematic cross sectional view of OPV devices with metallic grids as the front contact. Short circuit may occur when the lines are raised from the substrate (a). One solution is to bury the current collecting lines into the substrate (b).

In this work the embedding of these structures was performed by Reverse nanoimprinting transfer, which will be described in section 5.2.4.

5.2.2. Design and modelling of grid patterns

Two geometries were investigated: honeycomb and linear geometry. The former design has an important advantage against linear geometry: eventual line breaks have less impact in overall current collection, as charges can be redirected through alternative

paths along the grid. However, as it will be discussed later, linear geometry can be more adequate for the techniques used in this work to prepare the grids.

Figure 5.3 shows the unit cell and the parameters involved in the calculation of losses for honeycomb and linear geometry.
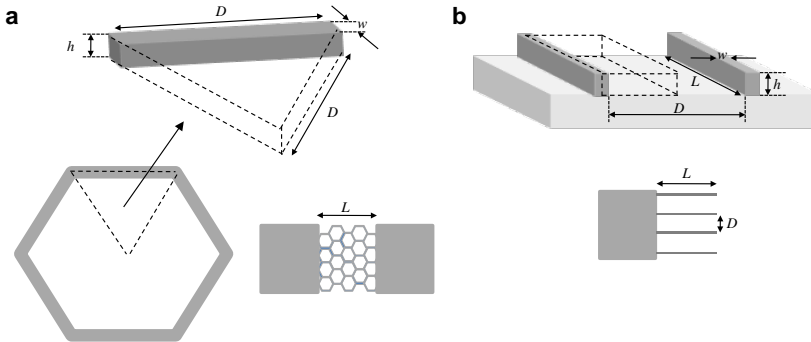
Figure 5.3. Scheme of the unit cell (dashed lines) and the dimensional parameters for a) honeycomb and b) linear geometry. Length (L), width (w) and height (h) of the Ag line are fixed in the calculations whereas the distance between lines, i.e., pitch (D), is varied. The sheet resistance of PEDOT:PSS (ρ_{sh}) and the bulk resistivity of Ag (ρ_M) are also input values in the calculation. Note that the scheme is not at scale; w is in the μm range while h is in the nm range.

To estimate shadowing and resistive losses of the Ag grid/PEDOT:PSS electrode, a numerical model described in literature[157] was adapted to this specific material system and modified to include the linear geometry, i.e., parallel lines, of the silver grid. The input parameters involved in these calculations are experimentally measured: the sheet resistance of PEDOT:PSS ($\rho_{sh} \sim 800$ Ω/sq), the bulk resistivity of Ag ($\rho_M \sim 3 \cdot 10^{-7}$ Ω·m), and the dimensions of the Ag lines, which depend on the coating technique: a) in evaporation through lithographic mask, the height (h) was set to 50, 100 or 150 nm and the width (w) ranged from 2 to 10 μm; b) in inkjet printing the height was set to 130 or 250 nm and the width was at constant 100 μm. In both cases the length (L) was fixed in the pattern at 5 mm. The only parameter we varied was the pitch (D). A typical OPV performance has to be taken into account as well. A voltage (V_{mpp}) and current density (J_{mpp}) at the maximum power point of 0.48 V and of 7 mA·cm^{-2}, respectively, were considered taking as a reference the 3.5% efficient organic solar cell presented by Hoth *et al*. with inkjet printed active layer,[71] since the solar cells fabricated in this work were realised in a similar manner. Further calculations made with the OPV results obtained in this work (see section 5.3) revealed negligible changes in the optimal pitch.

The resulting individual contributions to losses in current collection[157] for honeycomb and linear geometry are shown in **Table 5.2**.

Table 5.2. Individual contributions to losses for honeycomb and linear geometry.

Type of losses	Honeycomb	Linear
Shadowing	$1 - \dfrac{2\left(D - \frac{w}{\sqrt{3}}\right)\left(\frac{\sqrt{3}D - w}{2}\right)}{\sqrt{3}D^2}$	$\dfrac{w}{w + D}$
Sheet resistance of PEDOT:PSS	$\dfrac{J_{mpp}}{V_{mpp}} \dfrac{3\left(D - \frac{w}{\sqrt{3}}\right)^4}{8D^2} \rho_{sh}$	$\dfrac{J_{mpp}}{V_{mpp}} \dfrac{(w + D)^2}{12} \rho_{sh}$
Bulk metal resistance	$\dfrac{J_{mpp}}{V_{mpp}} \dfrac{64DL^4}{9\sqrt{3}hw} \rho_{M}$	$\dfrac{J_{mpp}}{V_{mpp}} \dfrac{(w + D)L^2}{3hw} \rho_{M}$

Resistive losses from interface contact between Ag lines and PEDOT:PSS were not considered in this work, as they might be negligible in comparison to the sheet resistance of PEDOT:PSS.

Figure 5.4 shows the estimated contribution to losses against the pitch in the two geometries, where it is clearly visible how shadowing governs in the regime with small separation between lines and the resistive losses become dominant at larger pitch, mostly because of the sheet resistance of PEDOT:PSS. This tendency is in accordance to other works that employed a similar modelling approach.[158]

Interesting aspects related to the chosen geometry can be observed. First, the range of pitch where the total losses are minimized is broader in the case of linear geometry (note that the scale in x axis in Figure 5.4 a and b is different). Minimum losses ± 3% are located between 720 μm and 2480 μm for linear geometry, whereas the corresponding range in honeycomb structure is noticeably lower (180 to 1110 μm). The contribution to losses of both shadowing and sheet resistance is more marked at the extremes in honeycomb structure. Moreover, as shown in the insets, linear geometry permits to choose a wider variety of optimum pitch by changing the line width. This fact is of big importance for two reasons: 1) lower line density can be employed in linear geometry by widening the lines, which means reduced use of metal,

and 2) this lower line density will facilitate the imprinting transfer and also will reduce the risk of microshunts, as will be discussed later in the text.
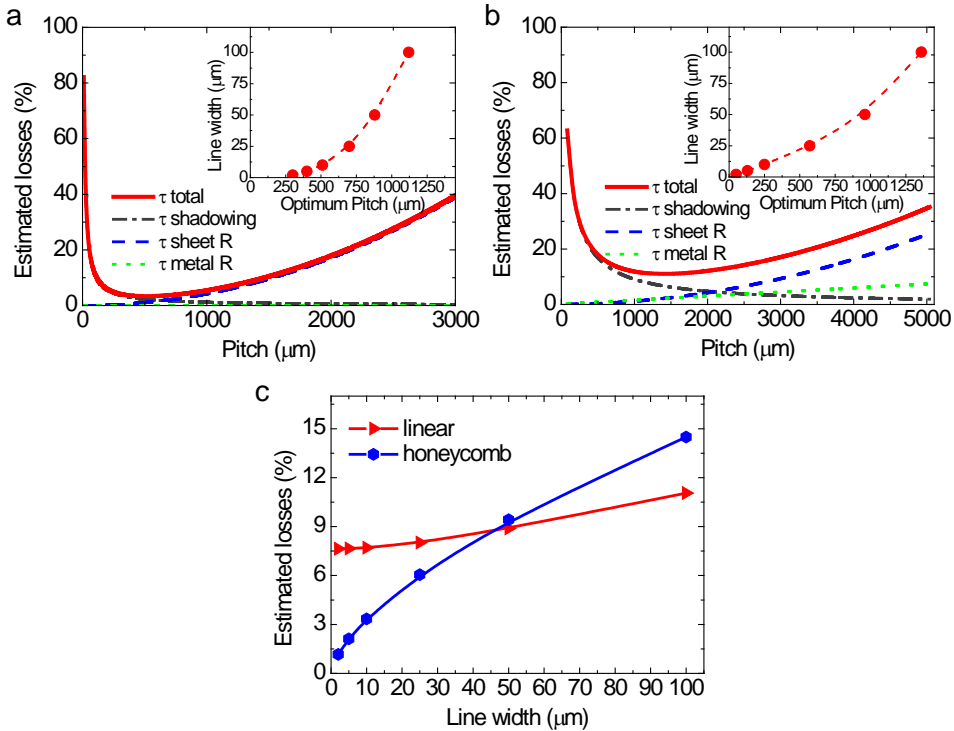
Figure 5.4. Examples of calculated contribution of shadowing and resistive losses as a function of the pitch in a) honeycomb (w = 10 μm, h = 100 nm) and b) linear (w = 100 μm, h = 250 nm) geometry. Insets show the influence of line width on the optimum pitch. c) Calculated total losses with optimum pitch for different line widths.

On the other hand, honeycomb structure offers the possibility to reduce the total losses below 2% when very thin lines are employed (see Figure 5.4c), in contrast to the minimum 7.6% achievable by using linear geometry. Indeed, two regimes are seen. Honeycomb geometry achieves lower total losses with line widths below 50 μm, while linear geometry would be more adequate from there on. The very low losses attributable to very thin lines may encourage the use of honeycomb structure.

5.2.3. Fabrication of Ag grids

The desired geometry of a current-collecting grid has to accomplish an optimal balance between transparency and conductivity. The former can be achieved by reducing the line width as much as possible as well as by increasing the pitch. On the other hand,

higher conductivity is obtained with higher line density, that is, with a smaller pitch. Alternatively, the conductivity can be increased by increasing the metal lines thickness, as described elsewhere.[159] However, too thick lines may cause current leakage and shorts unless they are embedded in the substrate, as explained previously.

In this work two different techniques were employed to fabricate the Ag grid structures. The first chosen method was evaporation through a mask (prepared by UV lithography), which can lead to narrow lines,[159] in the order of 1-2 μm width. This would minimize losses due to shadowing, as discussed above. Alternatively, inkjet printing Ag grids might be more favourable in terms of cost and scalability, despite resolution of lines being worse (~50-100 μm).

5.2.3.1. Evaporation through lithographic mask[B]

In the field of OPVs there are very few examples of metallic grid electrodes prepared by lithography. Kang and co-workers reported the fabrication of such structures by nanoimprint lithography (NIL).[159] Another interesting approach was presented by Tvingstedt and co-workers, where a cheaper, soft lithographic method was employed.[158] In both works very narrow lines were obtained. As said above, this may be interesting to reduce shadowing losses while keeping short distances between lines to maintain high conductivity. The fabrication process of grid structures by evaporation through UV lithographic mask used in this work is shown in **Figure 5.5**. A positive tone photoresist (S1818 from MicroChem) was spin coated at 5000 rpm for 60 s on top of sacrificial glass substrate, which was afterwards pre-baked at 115 °C for 60 s. Then, the Süss MA1006 UV mask aligner was used to fix the chromium mask and UV light exposure was therein applied for 7 s with MF319 machinery from Shipley. Metal evaporation was carried out by an electron beam evaporation system from AJA International (8kV). Finally, lift off was performed by immersing the sample in acetone and vigorously shaking.

[B] UV lithography and evaporation processes were partially performed by Dr. Nikolaos Kehagias. The design and characterisation of grid samples was partially performed by Dr. Paul Lacharmoise
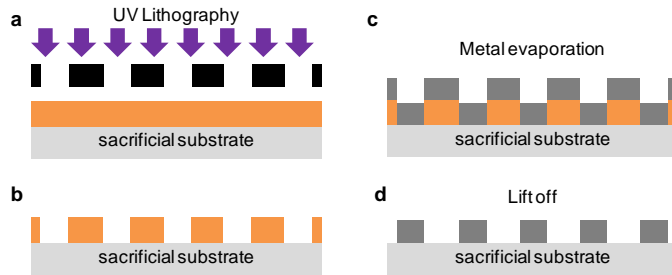
Figure 5.5. Preparation of grid samples. a) UV lithographic attack is performed on the surface of a curing resin through a chromium mask. b) The not cured areas correspond to the negative image of the grid pattern. c) Thermal evaporation of silver leads to a uniform layer with controlled thickness. d) The remaining resin is removed with acetone (lift off), which results in the final grid structure.

A wide set of grid samples were prepared in order to make conductivity characterisation. First, the honeycomb structure was chosen (**Figure 5.6a)**. The influence of line width (defined by the UV mask) and height (defined during thermal evaporation) on the grid resistance was studied. A clear dependence of grid resistance on both line parameters is shown in Figure 5.6b. According to these results, a minimum line height of 100 nm is necessary for this grid configuration to obtain low resistances. Also, line widths below 10 μm resulted in unacceptable values of grid resistance (≥ 50 Ω).
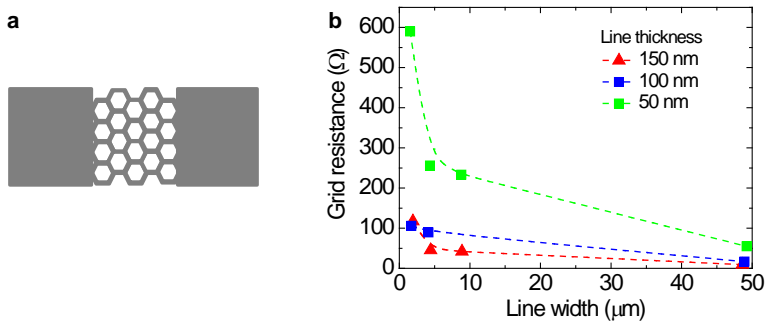
Figure 5.6. a) Pattern with "honeycomb" structure to perform resistance measurements. b) Correlation between grid resistance and line width, for three different line thicknesses. These data were measured by Dr. Paul Lacharmoise.

Further optimisation of grids was performed, including tests with linear configuration. However, several troubles in the fabrication of the grids were repetitively found, regardless from their geometry. As **Figure 5.7** shows, problems included breaks and damage within the lines as well as problems to remove the resin in the lift off process.

The latter was more pronounced in designs with high line density, which can be ascribed to the difficulty for acetone to infiltrate between adjacent lines. Also a not optimised UV exposure time could partially result in these failures.
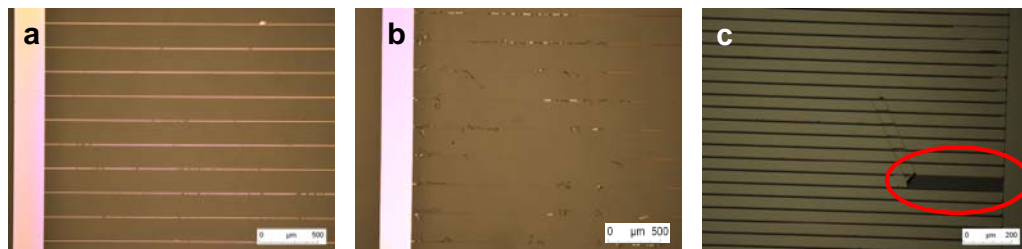
Figure 5.7. Troubles with lift off: a) many discontinuities in conducting lines, b) destruction of Ag lines during lift off in ultrasonic bath and c) impossibility to make the lift off with short distance between lines. The red circle points a small area that was lifted off.

Enlargement of the pitch and/or widening the lines would presumably overcome these features. However, both solutions would drive the grid geometries to a scenario where inkjet printing is more competitive.

5.2.3.2. Inkjet printing

Inkjet printing may be an interesting and cost effective technique for grid fabrication due to its compatibility with R2R processes and its mask-less nature. Some examples of inkjet printed current-collecting grids have been presented in the field of OPVs.[153,160] In all cases a thick PEDOT:PSS layer was deposited on the grids to cover them entirely, ideally with a thicker layer than the printed line height[65] with the consequence of a significant loss in transparency (see Figure 5.1). The latter is what we pretend to overcome by embedding the grids.

In order to know the key parameters for grid modelling and construction, two simple steps were followed. First, the resolution of the Fujifilm Dimatix DMP-2831 inkjet printer with the nanoparticle-based silver ink (SunTronic EMD 5603 from Sunchemical) was determined by performing a drop test. The latter consists in printing several lines with different drop spacing each one, in multiples of the minimum 5 μm (**Figure 5.8a,b**). The objective of this test is to find at which drop spacing the narrowest, thinnest and yet continuous lines are accessible. In a first stage, this limit was found at a drop space of 40 μm and using two jets, which resulted in lines of 100 μm width and 250 nm height. Further optimisation was achieved by performing a 10 min O_2 plasma treatment on the glass substrates prior to printing, which enhanced

significantly the wettability of the Ag ink. The latter allowed increasing the drop spacing up to 50 μm as well as using only one jet. As a result, the height of the Ag lines was reduced to 130 nm maintaining the 100 μm width, as shown using profilometry in Figure 5.8c. To the best of our knowledge, these are the thinnest metallic structures obtained by inkjet printing so far. With these two configurations (lines of 250 and 130 nm height) complete anode structures were fabricated using the pattern shown in Figure 5.8d. The latter consists of a central pad that connects all the current collecting lines. In a first stage the central pad and the lines were printed in consecutive layers. It was afterwards observed that this could result in contact resistance (see Figure 5.8e). Therefore, it was concluded that the grid structures should be printed in one single step.

A second test was performed to determine the conductivity (ρ = 3·10^{-7} Ω·m) along a single printed line (of 250 nm height) with the dimensions used in the final structure. This was achieved by printing the pattern shown inFigure 5.8f.

It has to be noted that honeycomb geometry was not employed for the grid patterns in inkjet printing. The reason is that the narrowest lines accessible are those parallel to the displacement of the print head, a condition not feasible for a honeycomb structure. Therefore, as minimum shadowing losses are mandatory for this application, we concluded that the linear geometry may be the best design for this particular printing technique.
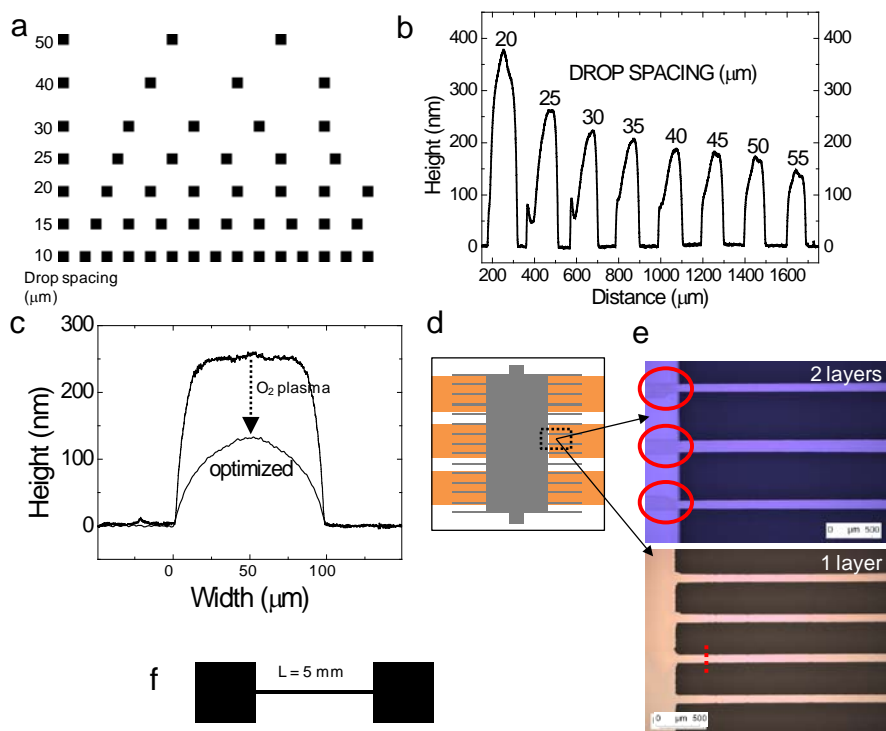
Figure 5.8. a) scheme of the pattern for the drop test, with increasing drop spacing in steps of 5 µm. b) Cross section profiles of inkjet printed silver lines using 2 jets and the drop test pattern; c) an optimised process enabled the reduction of the line height from 250 nm to 130 nm, while its width remained at constant 100 µm. d) Schematic front view of the inkjet printed Ag grid structures, comprising 6 OPV devices (coloured areas). e) Optical micrographs of printed structures. The connection between lines and central pad (indicated by circles) may be a source of series resistance if the structure is printed sequentially in two layers (top). This can be corrected by printing the whole structure in one unique layer (bottom). The dotted line points the area measured by profilometry in (c). f) Pattern used for the determination of conductivity in one printed Ag line.

5.2.4. Reverse nanoimprinting transfer[c]

For embedding the grid structures a simple, cost-effective method was used. It basically consists of transferring the grid from a sacrificial substrate to another substrate by using a photo-curable resin (see **Figure 5.9**). The grid structure is immersed in the resin, which is then covered by the new substrate and subsequently cured. Adequate surface pre-treatment and/or the use of adhesion promoters facilitate mechanical separation of

---

[c] The reverse nanoimprinting transfer process of all the samples was performed by Dr. Nikolaos Kehagias (ICN2)

the two substrates, being the grid structure hosted in the new substrate. Additionally, this method is potentially compatible with roll-to-roll processing, since no critical processes for flexible substrates are employed. In this work, however, rigid glass sacrificial substrates were used to prepare the grids as well as for the subsequent embedding. First trials with flexible substrates resulted in substrate bending due to different thermal expansion coefficients of silver, resin and substrate. The exposure time to UV light, which causes local heating, is therefore a critical parameter. To avoid substrate bending, faster curing and controlled amount of resin should be used. Ongoing work in this direction is currently being carried out.
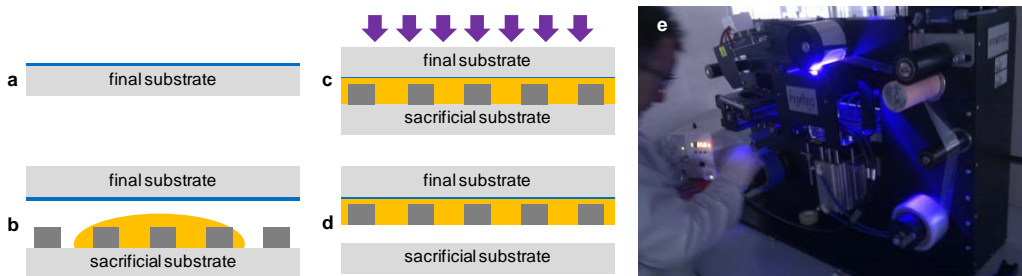
Figure 5.9. Reverse nanoimprinting transfer to embed Ag grids. (a) An adhesion promoter (Ormoprime08) is coated on a pre-treated (final) substrate. (b) A UV curing resin is drop casted on the sacrificial glass/Ag grid structure. (c) The two substrates are assembled and pressure and UV light exposure are applied subsequently. (d) Finally, the two substrates are mechanically separated, leading to the desired embedded Ag grid structure. (e) First trials of transferring this method to flexible, continuous substrates (courtesy of Dr. Nikolaos Kehagias).

The Ag grids were embedded within the substrate by reverse nanoimprinting transfer as follows (see Figure 5.9): 2.5 x 2.5 cm^2 glass substrates were cleaned by O$_2$ plasma at 400 W for 30s. Ormoprime08 (from Microresist Technology GmbH) was spin coated on top of cleaned glass substrates to increase the surface adhesion of the printable resin (Ormocomp). Without this adhesion layer an unacceptable large number of grid transfer errors was observed (see **Figure 5.10**). A drop of Ormocomp was dispensed on the pre-patterned glass substrates which contained the metal grid structures. The two substrates were then brought into contact while a pressure of 2 bars was applied for 1 min. The assembly was exposed to ultraviolet light for 10 s. After separation of the two substrates the Ag grid structures were embedded within the Ormocomp material and transferred to the pre-treated glass substrate.
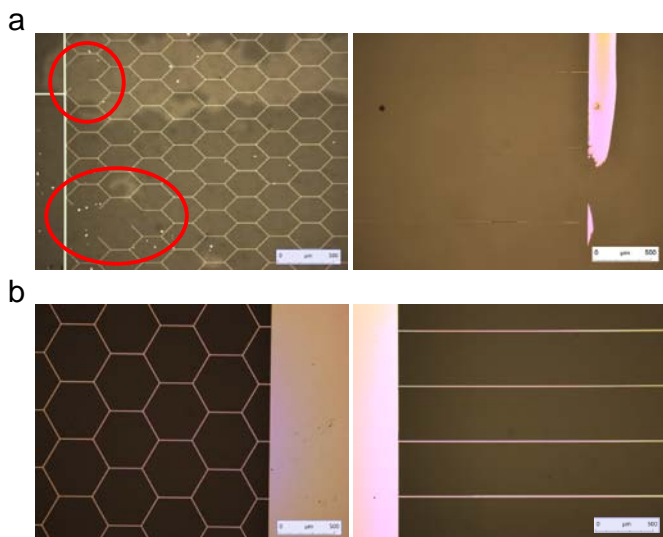
Figure 5.10. a) Defects after reverse nanoimprinting transfer were observed especially when narrow Ag lines (<10 μm) were prepared by evaporation through lithographic mask, and irrespective from the pattern. b) This was corrected by optimising the transfer conditions, including the use of a surface adhesion promoter. All these pictures correspond to samples with grids prepared by UV lithography.

It has to be noted that even after adjusting the conditions for best transfer process, random defects were observed in many samples with grids prepared by evaporation through lithographic mask. Most of those defects, as said above, were derived from a deficient lift off. In contrast, all the samples prepared by inkjet printing were successfully transferred, which can be ascribed to both larger pitch and width of Ag lines. According to the calculated contribution to losses, 1360 μm of pitch and 100 μm of line width are optimum when using inkjet printing. This contrasts with the optimum 200 μm of pitch and 10 μm of line width for evaporated grids.

After the embedding step, only 20 nm from the original 250 nm of inkjet printed Ag lines protruded from the surface (**Figure 5.11a**), which means 92% embedding. This approach offers significant advantages. First, it enables to overcoat the Ag grid with an optimal film thickness of PEDOT:PSS layer. Second, as said before, thick Ag lines guarantee high conductivity (resistive losses in the metal are minimized). Moreover, the smoothening of the surface facilitates a much more homogenous active layer deposition. The latter, together with the lowering of current leakage, are responsible for the improvement in fill factor observed in the J-V curves in OPV devices, as it will be shown in section 5.3.

Concerning transparency, Figure 5.11b shows the measured transmittance of these structures for various pitches comparing it to the ITO/glass case. This characterisation was performed with a Varian Cary 5000 UV-Vis-NIR spectrophotometer using a 25 mm^2 mask (equivalent to the active area of the OPV devices). As the separation between lines increases, a higher transmittance is obtained. The expected optimal region shows transmittances of around 80%, almost equivalent to the glass/ITO structure, with the advantage of showing a more flattened response in the visible region.
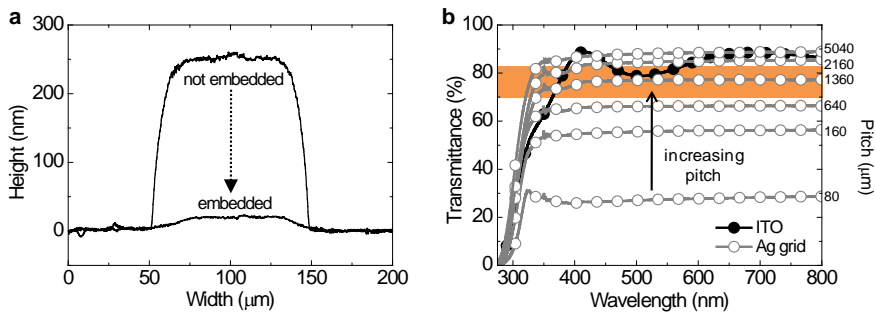
Figure 5.11. Characterisation of inkjet printed lines. a) Cross section profiles before (250 nm height) and after (20 nm height) embedding. b) Transmittance through embedded Ag grids with different line separation compared to ITO on glass. A 25 mm^2 mask (equivalent to the active area of the OPV devices) was employed for the measurement. The coloured area indicates the predicted optimum line separation in terms of losses.

5.2.5. Inkjet printing vs. Evaporation through lithographic mask

In summary, in this section we have demonstrated how grid structures can be prepared by UV lithography and by inkjet printing. Although narrower lines can be achieved with the former, some troubles related to the lift off process could not be solved. This resulted in a random and uncontrollable disparity of grid quality. As the solution would be to increase pitch and line width, inkjet printing becomes more favourable in this new grid geometry, as deduced from Figure 5.4. In these conditions, high grid quality fabrication and transfer were achieved by using inkjet printing.

Moreover, other relevant aspects make inkjet printing interesting for grid fabrication. It is sensibly cheaper than UV lithography, as the whole grid fabrication takes place in ambient conditions and at room temperature. Also, expensive masks are no further needed: digital modifications in pattern designs are straightforward. Finally, this is a solution-based process, thus highly compatible with roll-to-roll lines.

Also, the motivation for embedding the grid electrodes has been exposed. In the following section it is shown how this approach can contribute in an effective improvement in solar cell devices.

5.3. INKJET PRINTED ORGANIC SOLAR CELLS WITH EMBEDDED AG GRIDS

In order to assess the effect of embedding the grids in OPV devices, two different configurations of Ag lines were tested. First, as the height of the line is not the limiting factor for the embedded electrodes, inkjet printing conditions that led to 250 nm thick lines were used. Second, covered-only electrodes were also fabricated by using the configuration that resulted in lines of 130 nm height. Finally, reference devices with ITO anode were also fabricated. The structures of these devices are schemed in **Figure 5.12**.
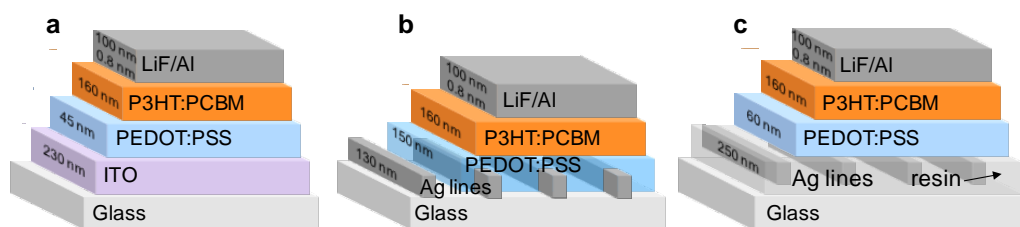
Figure 5.12. Schematic cross sectional view of OPV devices (not in scale) with a) ITO and with b) covered-only and c) embedded silver grid lines as the front contact.

The solar cells were fabricated by doctor blade coating the PEDOT:PSS, inkjet printing the P3HT:PCBM layer and evaporating LiF and Al cathode, following the general recipes described in chapter 2. The blade speed was increased up to 10 mm/s for doctor blading PEDOT:PSS on top of ITO-free, covered-only anode in order to obtain a thicker layer to cover the Ag lines fully (see Figure 5.12). The resulting layers were 45 nm, 60 nm and 150 nm thick in ITO-based, ITO-free embedded and ITO-free covered-only devices, respectively. Attempts to reduce the PEDOT:PSS layer further for the ITO-free only covered devices with the aim of minimizing transparency losses resulted in frequent shortcut devices. The rest of the solar cell stack was identical in the three structures and was built using the design shown in Figure 5.8d.

5.3.1. The influence of the distance between lines

With the intention of finding optimum performance conditions and simultaneously validating the predictions made in the modelling of estimated losses, a series of grid samples were prepared. Seven representative patterns were chosen, ranging from very low to very large pitch, which result in high shadowing and resistive losses, respectively (see **Figure 5.13**). According to the calculations, the sum of the different contributions to losses is below 15% in the range between 650 µm and 2650 µm of pitch. The highest OPV performance is, therefore, expected to be achievable using grids whose pitches are in that range.
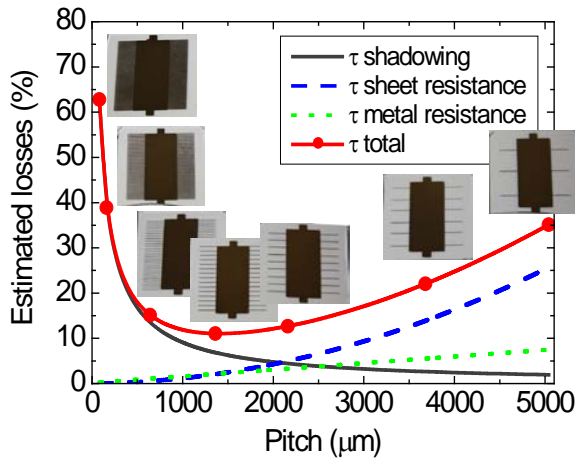
Figure 5.13. The series of prepared grid substrates for OPV devices overlapped with the estimation of losses.

A summary of the relevant parameters of this set of grids is presented in **Table 5.3**. It can be therein observed that the transmission in the predicted optimum range is between 65% and 85% (see also Figure 5.11b).

Table 5.3. Properties of the series of substrates with embedded Ag grids.

Pitch (µm)	80	160	640	1360	2160	3680	5040	Glass/ Ormocomp
Surface coverage (%)	62.5	38.5	13.5	6.8	4.4	2.6	1.9	0
Estimated total losses (%)	62.8	38.9	15.1	11.1	12.7	22.0	35.1	100
Transmittance at 550 nm (%)	27.5	55.9	66.3	77.1	84.7	87.9	88.2	90.5

The influence of the pitch in the OPV performance was studied. Only the series of embedded Ag grids were considered in this case. When the photovoltaic characteristics of these selected devices are plotted as a function of the separation between lines, a high correlation with the estimated losses is observed (**Figure 5.14**). The dependence of PCE on the pitch is a curve with high mirror symmetry with respect to the curve of estimated losses. These results demonstrate that there is a good correlation between predictions and experimental results, thus the adapted model for estimating losses of Ag grids appears to be validated.
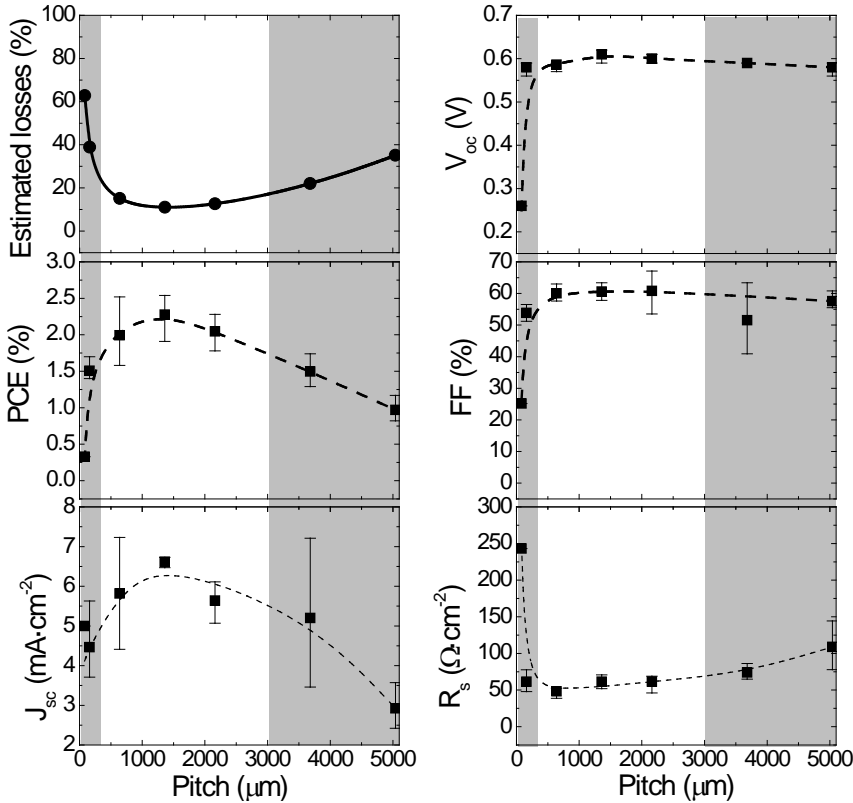
Figure 5.14. Dependence of OPV performance parameters on the pitch compared to predicted losses. Greyed areas indicate the regimes where shadowing (left) is too high and resistive losses (right) limit the current extraction.

Further examination of Figure 5.14 shows how the photogenerated current (J_{sc}) is limited by the shadowing effect for too small line separation. A maximum is reached after that at a pitch of 1360 µm, and then J_{sc} diminishes again at a slower rate at larger pitch where charge extraction is reduced by resistive losses. On the other hand, V_{oc} and FF show similar trends: (a) low values are obtained at high density of grid lines due to poor rectification, presumably derived from inadequate morphology and/or higher current leakage; and (b) the crowding of lines increases the probability of microshunts, probably due to an eventual, faulty embedding. Then, a maximum is rapidly reached (pitch ≥ 160 µm) followed by a plateau from there on. Finally, the series resistance (R_s) follows a similar tendency as the estimated losses. This is in good agreement with the work of Tvingstedt *et al.* where they conclude that the cell series resistance becomes large when the Ag grid is too closely or too widely spaced.[158] As discussed before, the resistive losses govern at large pitch (Figure 5.4), mostly due to PEDOT:PSS. It is thus

obvious that this layer is the main responsible for the increasing of the series resistance. On the other hand, the origin of the high R_s with low line separation is less intuitive. As suggested above, we ascribe this to a poorer coverage of the grid lines. Even with an embedded structure, a higher line concentration (pitch < 160 µm) entails a higher risk of differences in line height or topography. This may lead to microshunts (lower parallel resistance) and/or poorer contact between metallic lines and PEDOT:PSS (higher series resistance). In this specific case, the contact resistance in this interface, which has been omitted in the estimation of losses, might not be negligible.

5.3.2. Enhanced fill factor with embedded electrodes

Organic solar cells with the three designs depicted in Figure 5.12 were fabricated with the optimised grid geometry. Besides the anode and the PEDOT:PSS layer thickness, the rest of the structure was constructed identically in order to enable comparison, i.e. 160 nm thick inkjet printed P3HT:PCBM and evaporated LiF (0.8 nm)/Al (100 nm) cathode. The current density-voltage (J-V) characteristics of the optimised devices (**Figure 5.15**) unquestionably show relevant improvement from covered-only to embedded Ag grid structures in all cell parameters (see also **Table 5.4**).
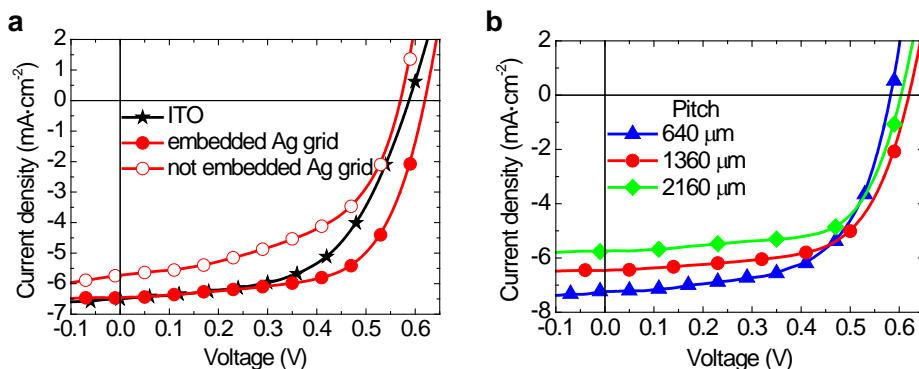
Figure 5.15. J-V curves of optimised organic solar cells build on a) different anode structures b) embedded silver grids with different pitch within the optimal range.

Table 5.4. Photovoltaic characteristics of the organic solar cells based on different anodes (Figure 5.15a).

Anode	V_{oc} (V)	J_{sc} (mA·cm^{-2})	FF (%)	PCE (%)	R_s (Ω·cm^{-2})	R_p (Ω·cm^{-2})
ITO	0.59	6.50	57	2.15	20.0	1734
Embedded Ag grid	0.62	6.46	63	2.54	11.5	3425
Covered-only Ag grid	0.57	5.71	52	1.70	14.2	463

The lower values of (mainly) short-circuit current, fill factor and parallel resistance obtained with the only-covered anode evidence that current leakage is strong, as expected. We note that part of the J_{sc} drop can be related to ca. 8% decrease in transmission through PEDOT:PSS when increasing its thickness from 60 nm to 130 nm. The 52% of FF is likewise in the same order of similar devices described in literature.[153] On the contrary, the J-V curve of the embedded structure shows a much better rectification: low series resistance, high parallel resistance and high FF. This is a result of a flattened interface between Ag grid and PEDOT:PSS.[161] As far as we know, this is the highest reported value for FF in ITO-free devices containing Ag grids processed in air conditions (note that the cathode was evaporated in vacuum). In turn, the J_{sc} is almost the same as for the ITO-based device, which indicates that the grid structure has the same current collecting capability as ITO. However, the PCE values are lower than expected (PCE = 3-3.5%, as in chapter 3). It can be concluded that J_{sc} is the main responsible for that, considering that good rectification and open circuit voltages (V_{oc}) are obtained. Consequently, other factors besides the anode may be behind this, such as active material degradation (independent on the fabrication process). Even so, the PCE$_{ITO-free}$/PCE$_{ITO}$ ratio for the embedded structure is higher than 1, which is also in accordance with what is exposed in the introduction of this chapter (see Table 5.1).

Table 5.5. Photovoltaic characteristics of the "hero" devices based on embedded silver grids with different pitch within the optimal range.

Pitch	V_{oc}	J_{sc}	FF	PCE	R_s	R_p
(μm)	(V)	(mA·cm^{-2})	(%)	(%)	(Ω·cm^{-2})	(Ω·cm^{-2})
640	0.58	7.23	60	2.52	9.8	636
1360	0.62	6.46	63	2.54	11.5	3425
2160	0.60	5.76	67	2.28	11.7	6977

The highest FF obtained in the studied series of devices was 67%, corresponding to the grid with a pitch of 2160 μm. The fact that high FF were obtained with large pitches may support our hypothesis. Larger pitch means less density of Ag lines, which in turn reduces the risk of microshunts due to differences in the height of (protruded) lines. The subsequent coverage of those lines with the PEDOT:PSS layer might be more effective at larger pitches. As a result, a noticeable enhancement in parallel resistance is obtained, which is the responsible for the improvement in FF. These results drive to an interesting conclusion. It seems clear that the density of current collecting lines is determinant in photovoltaic performance, not only due to its contribution to shadowing and resistive losses, but also because of its influence on the topology of successive layers. The latter cannot be predicted in the model, as it is strictly related to a technological aspect of the fabrication process. These model-to-experiment deviations have to be taken into account.

5.4. CONCLUSIONS

We have shown the entire process of optimisation of current collecting Ag grids for ITO replacement in organic solar cells. First, we have adapted a model to estimate shadowing and resistive losses in both honeycomb and linear geometry. Similar trends are predicted in the two cases: shadowing governs with short distance between lines whereas resistive losses limit current extraction when the pitch is too high. According to our calculations and input values, honeycomb structure is more favourable with narrow lines (width below 50 μm) while linear geometry is more adequate at wider values.

Secondly, two different techniques have been used to build the grid structures. Evaporation through UV lithographic mask led to much narrower lines (down to 2 μm) in comparison to inkjet printing (100 μm). However, lift off has been identified as a critical step in UV lithography process when working with narrow lines (width < 10 μm). Random defects, including broken lines, could not be avoided. On the contrary, it has been demonstrated that inkjet printing is more robust for this application. Other advantages such as ambient processing, R2R compatibility and the lack of need of expensive masks are solid arguments for this technology. Moreover, the optimisation of the printing processing conditions has allowed reaching the thinnest possible Ag lines (130 nm).

Then, we demonstrated the reverse nanoimprinting transfer as an easy, low-cost and potentially R2R-compatible technique to embed Ag grid structures. The transfer of inkjet printed structures resulted to be much more efficient in comparison to those prepared by UV lithography. An embedding of more than 90% within the substrate was obtained. Higher homogeneity in subsequent layers of OPV devices was achieved using this improved anode interface while the risk of current leakage was significantly reduced. This resulted in the enhancement of the fill factor (FF > 60%) of the solar cell devices. This ITO-free structure has similar current collecting capability as ITO. Finally, the influence of the distance between grid lines was successfully correlated with the photovoltaic performance of the devices, thus validating the model used for the Ag grid optimisation.

BIBLIOGRAPHY

1. J. Schindler and W. Zittel, Crude Oil - The Supply Outlook, (2008).

2. BP Statistical Review of World Energy, (2013).

3. WWF, Climate Change: Why we need to take action Now, (2006).

4. IPCC, Fifth Assessment Report of the Intergovernmental Panel on Climate Change, (2013).

5. J. Rifkin, *The Third Industrial Revolution* (Palgrave MacMillan, 2011).

6. Red Eléctrica Española, www.ree.es

7. A. Urbina, Solar electricity in a changing environment: The case of Spain, *Renew. Energy* **68** (2014) 264–269.

8. F. C. Krebs, *Polymeric Solar Cells. Materials, Design, Manufacture* (DEStech Publications, Inc., 2010).

9. W. Shockley and H. J. Queisser, Detailed Balance Limit of Efficiency of p-n Junction Solar Cells, *J. Appl. Phys.* **32** (1961) 510.

10. Sharp, http://sharp-world.com/corporate/news/130424.html.

11. A. Yella, H.-W. Lee, H. N. Tsao, C. Yi, A. K. Chandiran, M. K. Nazeeruddin, E. W.-G. Diau, C.-Y. Yeh, S. M. Zakeeruddin and M. Grätzel, Porphyrin-sensitized solar cells with cobalt (II/III)-based redox electrolyte exceed 12 percent efficiency, *Science* **334** (2011) 629–34.

12. Heliatek, http://www.heliatek.com/wp-content/uploads/2013/01/130116_PR_Heliatek_achieves_record_cell_effiency_for_OPV.pdf.

13. J. Nelson, *The physics of solar cells* (Imperial College Press, London, 2003).

14. J. Frenkel, On the transformation of light into heat in solids, *Phys. Rev.* **37** (1931) 17–44.

15. S. Karg, W. Riess, V. Dyakonov and M. Schwoerer, Electrical and optical characterization of poly (phenylene-vinylene) light emitting diodes, *Synth. Met.* **54** (1993) 427–433.

16. C. W. Tang, Two-layer organic photovoltaic cell, *Appl. Phys. Lett.* **48** (1986) 183–185.

17. S. R. Scully and M. D. McGehee, Effects of optical interference and energy transfer on exciton diffusion length measurements in organic semiconductors, *J. Appl. Phys.* **100** (2006) 034907.

18. N. S. Sariciftci, L. Smilowitz, A. J. Heeger and F. Wudl, Photoinduced Electron-Transfer From A Conducting Polymer To Buckminsterfullerene, *Science* **258** (1992) 1474–1476.

19. G. Yu, J. Gao, J. C. Hummelen, F. Wudl and A. J. Heeger, Polymer Photovoltaic Cells: Enhanced Efficiencies via a Network of Internal Heterojunctions, *Science* **270** (1995) 1789–1791.

20. B. Kannan, K. Castelino and A. Majumdar, Design of Nanostructured Heterojunction Polymer Photovoltaic Devices, *Nano Lett.* **3** (2003) 1729–1733.

21. R. A. J. Janssen and J. Nelson, Factors limiting device efficiency in organic photovoltaics., *Adv. Mater.* **25** (2013) 1847–58.

22. M. P. de Jong, L. J. van IJzendoorn and M. J. A. de Voigt, Stability of the interface between indium-tin-oxide and poly(3,4-ethylenedioxythiophene)/poly(styrenesulfonate) in polymer light-emitting diodes, *Appl. Phys. Lett.* **77** (2000) 2255–2257.

| | Bibliography

23. A. Martínez-Otero, X. Elias, R. Betancur and J. Martorell, High-Performance Polymer Solar Cells Using an Optically Enhanced Architecture, *Adv. Opt. Mater.* **1** (2013) 37–42.

24. C. J. Brabec, S. Gowrisanker, J. J. M. Halls, D. Laird, S. Jia and S. P. Williams, Polymer-fullerene bulk-heterojunction solar cells., *Adv. Mater.* **22** (2010) 3839–56.

25. V. D. Mihailetchi, P. W. M. Blom, J. C. Hummelen and M. T. Rispens, Cathode dependence of the open-circuit voltage of polymer:fullerene bulk heterojunction solar cells, *J. Appl. Phys.* **94** (2003) 6849.

26. J. J. M. Halls, J. Cornil, D. A. dos Santos, R. Silbey, D.-H. Hwang, A. B. Holmes, J. L. Brédas and R. H. Friend, Charge- and energy-transfer processes at polymer/polymer interfaces: A joint experimental and theoretical study, *Phys. Rev. B* **60** (1999) 5721–5727.

27. R. Kroon, M. Lenes, J. C. Hummelen, P. W. M. Blom and B. De Boer, Small bandgap polymers for organic solar cells (polymer material development in the last 5 years), *Polym. Rev.* **48** (2008) 531–582.

28. E. Bundgaard and F. Krebs, Low band gap polymers for organic photovoltaics, *Sol. Energy Mater. Sol. Cells* **91** (2007) 954–985.

29. M. C. Scharber, D. Mühlbacher, M. Koppe, P. Denk, C. Waldauf, A. J. Heeger and C. J. Brabec, Design Rules for Donors in Bulk-Heterojunction Solar Cells—Towards 10 % Energy-Conversion Efficiency, *Adv. Mater.* **18** (2006) 789–794.

30. M. C. Scharber and N. S. Sariciftci, Efficiency of bulk-heterojunction organic solar cells., *Prog. Polym. Sci.* **38** (2013) 1929–1940.

31. C. J. Brabec, S. E. Shaheen, C. Winder, N. S. Sariciftci and P. Denk, Effect of LiF/metal electrodes on the performance of plastic solar cells, *Appl. Phys. Lett.* **80** (2002) 1288–1290.

32. W. L. Ma, C. Y. Yang, X. Gong, K. Lee and A. J. Heeger, Thermally stable, efficient polymer solar cells with nanoscale control of the interpenetrating network morphology, *Adv. Funct. Mater.* **15** (2005) 1617–1622.

33. B. C. Thompson and J. M. J. Fréchet, Polymer-fullerene composite solar cells., *Angew. Chem. Int. Ed. Engl.* **47** (2008) 58–77.

34. H. Zhou, L. Yang and W. You, Rational Design of High Performance Conjugated Polymers for Organic Solar Cells, *Macromolecules* **45** (2012) 607–632.

35. S. E. Shaheen, C. J. Brabec, S. N. Sariciftci, F. Padinger, T. Fromherz and J. C. Hummelen, 2.5% Efficient Organic Plastic Solar Cells, *Appl. Phys. Lett.* **78** (2001) 841–843.

36. O. Inganäs, F. Zhang and M. R. Andersson, Alternating polyfluorenes collect solar light in polymer photovoltaics., *Acc. Chem. Res.* **42** (2009) 1731–1739.

37. C. M. Björström Svanström, J. Rysz, A. Bernasik, A. Budkowski, F. Zhang, O. Inganäs, M. R. Andersson, K. O. Magnusson, J. J. Benson-Smith, J. Nelson and E. Moons, Device Performance of APFO-3/PCBM Solar Cells with Controlled Morphology, *Adv. Mater.* **21** (2009) 4398–4403.

38. D. Mühlbacher, M. C. Scharber, M. Morana, Z. Zhu, D. Waller, R. Gaudiana and C. J. Brabec, High Photovoltaic Performance of a Low-Bandgap Polymer, *Adv. Mater.* **18** (2006) 2884–2889.

39. J. Peet, J. Y. Kim, N. E. Coates, W. L. Ma, D. Moses, A. J. Heeger and G. C. Bazan, Efficiency enhancement in low-bandgap polymer solar cells by processing with alkane dithiols., *Nat. Mater.* **6** (2007) 497–500.

40. N. Blouin, a Michaud and M. Leclerc, A low-bandgap poly(2,7-carbazole) derivative for use in high-performance solar cells, *Adv. Mater.* **19** (2007) 2295–2300.

41. J. S. Moon, J. Jo and A. J. Heeger, Nanomorphology of PCDTBT:PC70BM Bulk Heterojunction Solar Cells, *Adv. Energy Mater.* **2** (2012) 304–308.

42. K. H. Hendriks, G. H. L. Heintges, V. S. Gevaerts, M. M. Wienk and R. A. J. Janssen, High-Molecular-Weight Regular Alternating Diketopyrrolopyrrole-based Terpolymers for Efficient Organic Solar Cells, *Angew. Chemie Int. Ed.* **52** (2013) 8341–8344.

43. H. J. Son, W. Wang, T. Xu, Y. Liang, Y. Wu, G. Li and L. Yu, Synthesis of Fluorinated Polythienothiophene- co -benzodithiophenes and Effect of Fluorination on the Photovoltaic Properties, *J. Am. Chem. Soc.* **133** (2011) 1885–1894.

44. Z. He, C. Zhong, X. Huang, W.-Y. Wong, H. Wu, L. Chen, S. Su and Y. Cao, Simultaneous Enhancement of Open-Circuit Voltage, Short-Circuit Current Density, and Fill Factor in Polymer Solar Cells, *Adv. Mater.* **23** (2011) 4636–4643.

45. F. C. Krebs, Fabrication and processing of polymer solar cells: A review of printing and coating techniques, *Sol. Energy Mater. Sol. Cells* **93** (2009) 394–412.

46. L. Wengeler, M. Schmitt, K. Peters, P. Scharfer and W. Schabel, Comparison of large scale coating techniques for organic and hybrid films in polymer based solar cells, *Chem. Eng. Process. Process Intensif.* **68** (2013) 38–44.

47. M. Singh, H. M. Haverinen, P. Dhagat and G. E. Jabbour, Inkjet printing-process and its applications., *Adv. Mater.* **22** (2010) 673–85.

48. www.ceradrop.fr.

49. E. Tekin, P. J. Smith and U. S. Schubert, Inkjet printing as a deposition and patterning tool for polymers and inorganic particles, *Soft Matter* **4** (2008) 703–713.

50. B. Derby, Inkjet Printing of Functional and Structural Materials: Fluid Property Requirements, Feature Stability, and Resolution, *Annu. Rev. Mater. Res.* **40** (2010) 395–414.

51. J. Kim, J.-S. Kim, S.-W. Kwak, J.-S. Yu, Y. Jang, J. Jo, T.-M. Lee and I. Kim, Effects of the Al cathode evaporation rate on the performance of organic solar cells, *Appl. Phys. Lett.* **101** (2012) 213304.

52. Y. Galagan and R. Andriessen, Organic Photovoltaics : Technologies and Manufacturing, in *Third Gener. Photovoltaics*, ed. Vasilis Fthenakis (InTech, 2012), pp. 61–90.

53. Fujifilm Dimatix Inc., www.fujifilmusa.com.

54. X. Liu, S. Huettner, Z. Rong, M. Sommer and R. H. Friend, Solvent additive control of morphology and crystallisation in semiconducting polymer blends., *Adv. Mater.* **24** (2012) 669–674.

55. C. Scharsich, R. H. Lohwasser, M. Sommer, U. Asawapirom, U. Scherf, M. Thelakkat, D. Neher and A. Köhler, Control of aggregate formation in poly(3-hexylthiophene) by solvent, molecular weight, and synthetic method, *J. Polym. Sci. Part B Polym. Phys.* **50** (2012) 442–453.

56. E. Wang, J. Bergqvist, K. Vandewal, Z. Ma, L. Hou, A. Lundin, S. Himmelberger, A. Salleo, C. Müller, O. Inganäs, F. Zhang and M. R. Andersson, Conformational Disorder Enhances Solubility and Photovoltaic Performance of a Thiophene-Quinoxaline Copolymer, *Adv. Energy Mater.* **3** (2013) 806–814.

57. S. Malik, T. Jana and A. K. Nandi, Thermoreversible Gelation of Regioregular Poly(3-hexylthiophene) in Xylene, *Macromolecules* **34** (2001) 275–282.

58. T. Erb, U. Zhokhavets, G. Gobsch, S. Raleva, B. Stühn, P. Schilinsky, C. Waldauf and C. J. Brabec, Correlation Between Structural and Optical Properties of Composite Polymer/Fullerene Films for Organic Solar Cells, *Adv. Funct. Mater.* **15** (2005) 1193–1196.

59. J. Clark, J.-F. Chang, F. C. Spano, R. H. Friend and C. Silva, Determining exciton bandwidth and film microstructure in polythiophene films using linear absorption spectroscopy, *Appl. Phys. Lett.* **94** (2009) 163306.

60. W. C. Tsoi, D. T. James, J. S. Kim, P. G. Nicholson, C. E. Murphy, D. D. C. Bradley, J. Nelson and J.-S. Kim, The nature of in-plane skeleton Raman modes of P3HT and their correlation to the degree of molecular order in P3HT:PCBM blend thin films., *J. Am. Chem. Soc.* **133** (2011) 9834–9843.

61. K. Tvingstedt, K. Vandewal, F. Zhang and O. Inganäs, On the Dissociation Efficiency of Charge Transfer Excitons and Frenkel Excitons in Organic Solar Cells : A Luminescence Quenching Study, *J. Phys. Chem. C* **114** (2010) 21824–21832.

62. M. Campoy-Quiles, M. I. Alonso, D. D. C. Bradley and L. J. Richter, Advanced Ellipsometric Characterization of Conjugated Polymer Films, *Adv. Funct. Mater.* **24**, (2014) 2116–2134.

63. H.-K. Kim, I.-K. You, J. B. Koo and S.-H. Kim, Organic solar cells fabricated on inkjet-printed indium tin oxide electrodes, *Surf. Coatings Technol.* **211** (2012) 33–36.

64. Y. Galagan, R. Andriessen, E. Rubingh, N. Grossiord, P. W. M. Blom, S. C. Veenstra, W. J. H. Verhees and J. M. Kroon, Toward fully printed Organic Photovoltaics : Processing and Stability, *Lope-C* (2010) 88–91.

65. M. Neophytou, F. Hermerschmidt, A. Savva, E. Georgiou and S. A. Choulis, Highly efficient indium tin oxide-free organic photovoltaics using inkjet-printed silver nanoparticle current collecting grids, *Appl. Phys. Lett.* **101** (2012) 193302.

66. Y. Galagan, E. W. C. Coenen, S. Sabik, H. H. Gorter, M. Barink, S. C. Veenstra, J. M. Kroon, R. Andriessen and P. W. M. Blom, Evaluation of ink-jet printed current collecting grids and busbars for ITO-free organic solar cells, *Sol. Energy Mater. Sol. Cells* **104** (2012) 32–38.

67. K. X. Steirer, J. J. Berry, M. O. Reese, M. F. A. M. van Hest, A. Miedaner, M. W. Liberatore, R. T. Collins and D. S. Ginley, Ultrasonically sprayed and inkjet printed thin film electrodes for organic solar cells, *Thin Solid Films* **517** (2009) 2781–2786.

68. S. H. Eom, S. Senthilarasu, P. Uthirakumar, S. C. Yoon, J. Lim, C. Lee, H. S. Lim, J. Lee and S.-H. Lee, Polymer solar cells based on inkjet-printed PEDOT:PSS layer, *Org. Electron.* **10** (2009) 536–542.

69. T. Aernouts, T. Aleksandrov, C. Girotto, J. Genoe and J. Poortmans, Polymer based organic solar cells using ink-jet printed active layers, *Appl. Phys. Lett.* **92** (2008) 033306.

70. C. N. Hoth, S. A. Choulis, P. Schilinsky and C. J. Brabec, High Photovoltaic Performance of Inkjet Printed Polymer:Fullerene Blends, *Adv. Mater.* **19** (2007) 3973–3978.

71. C. N. Hoth, P. Schilinsky, S. A. Choulis and C. J. Brabec, Printing Highly Efficient Organic Solar Cells, *Nano Lett.* **8** (2008) 2806–2813.

72. C. N. Hoth, S. A. Choulis, P. Schilinsky and C. J. Brabec, On the effect of poly(3-hexylthiophene) regioregularity on inkjet printed organic solar cells, *J. Mater. Chem.* **19** (2009) 5398.

73. M. Neophytou, W. Cambarau, F. Hermerschmidt, C. Waldauf, C. Christodoulou, R. Pacios and S. A. Choulis, Inkjet-printed polymer–fullerene blends for organic electronic applications, *Microelectron. Eng.* **95** (2012) 102–106.

74. S. H. Eom, H. Park, S. H. Mujawar, S. C. Yoon, S.-S. Kim, S.-I. Na, S.-J. Kang, D. Khim, D.-Y. Kim and S.-H. Lee, High efficiency polymer solar cells via sequential inkjet-printing of PEDOT:PSS and P3HT:PCBM inks with additives, *Org. Electron.* **11** (2010) 1516–1522.

75. A. Lange, M. Wegener, C. Boeffel, B. Fischer, A. Wedel and D. Neher, A new approach to the solvent system for inkjet-printed P3HT:PCBM solar cells and its use in devices with printed passive and active layers, *Sol. Energy Mater. Sol. Cells* **94** (2010) 1816–1821.

76. A. Teichler, R. Eckardt, S. Hoeppener, C. Friebe, J. Perelaer, A. Senes, M. Morana, C. J. Brabec and U. S. Schubert, Combinatorial Screening of Polymer:Fullerene Blends for Organic Solar Cells by Inkjet Printing, *Adv. Energy Mater.* **1** (2011) 105–114.

77. D. Angmo, J. Sweelssen, R. Andriessen, Y. Galagan and F. C. Krebs, Inkjet Printing of Back Electrodes for Inverted Polymer Solar Cells, *Adv. Energy Mater.* **3** (2013) 1230–1237.

78. www.solliance.eu. [Accessed: 11-Dec-2013].

79. D. Angmo, T. T. Larsen-Olsen, M. Jørgensen, R. R. Søndergaard and F. C. Krebs, Roll-to-Roll Inkjet Printing and Photonic Sintering of Electrodes for ITO Free Polymer Solar Cell Modules and Facile Product Integration, *Adv. Energy Mater.* **3** (2013) 172–175.

80. R. D. Deegan, O. Bakajin, T. F. Dupont, G. Huber, S. R. Nagel and T. A. Witten, Capillary flow as the cause of ring stains from dried liquid drops, *Nature* **389** (1997) 827–829.

81. R. D. Deegan, Pattern formation in drying drops, *Phys. Rev. E* **61** (2000) 475–485.

82. B.-J. de Gans and U. S. Schubert, Inkjet printing of well-defined polymer dots and arrays., *Langmuir* **20** (2004) 7789–7793.

83. D. Chirvase, J. Parisi, J. C. Hummelen and V. Dyakonov, Influence of nanomorphology on the photovoltaic action of polymer–fullerene composites, *Nanotechnology* **15** (2004) 1317–1323.

84. B. Schmidt-Hansberg, H. Do, a. Colsmann, U. Lemmer and W. Schabel, Drying of thin film polymer solar cells, *Eur. Phys. J. Spec. Top.* **166** (2009) 49–53.

85. Y. Yao, J. Hou, Z. Xu, G. Li and Y. Yang, Effects of Solvent Mixtures on the Nanoscale Phase Separation in Polymer Solar Cells, *Adv. Funct. Mater.* **18** (2008) 1783–1789.

86. J. Perelaer, PhD Thesis (2009).

87. M. Campoy-Quiles, Y. Kanai, A. El-Basaty, H. Sakai and H. Murata, Ternary mixing: A simple method to tailor the morphology of organic solar cells, *Org. Electron.* **10** (2009) 1120–1132.

88. A. Teichler, J. Perelaer and U. S. Schubert, Inkjet printing of organic electronics – comparison of deposition techniques and state-of-the-art developments, *J. Mater. Chem. C* **1** (2013) 1910.

89. J. Nelson, J. Kirkpatrick and P. Ravirajan, Factors limiting the efficiency of molecular photovoltaic devices, *Phys. Rev. B* **69** (2004) 035337.

90. A. Kumar, S. Sista and Y. Yang, Dipole induced anomalous S-shape I-V curves in polymer solar cells, *J. Appl. Phys.* **105** (2009) 094512.

91. A. Wagenpfahl, D. Rauh, M. Binder, C. Deibel and V. Dyakonov, S-shaped current-voltage characteristics of organic solar devices, *Phys. Rev. B* **82** (2010) 115306.

92. D. Carsten and D. Vladimir, Polymer–fullerene bulk heterojunction solar cells, *Reports Prog. Phys.* **73** (2010) 96401.

93. C. S. Lee, J. X. Tang, Y. C. Zhou and S.-T. Lee, Interface dipole at metal-organic interfaces: Contribution of metal induced interface states, *Appl. Phys. Lett.* **94** (2009) 113304.

94. D. Gupta, M. Bag and K. S. Narayan, Correlating reduced fill factor in polymer solar cells to contact effects, *Appl. Phys. Lett.* **92** (2008) 093301.

95. G. del Pozo, B. Romero and B. Arredondo, Evolution with annealing of solar cell parameters modeling the S-shape of the current–voltage characteristic, *Sol. Energy Mater. Sol. Cells* **104** (2012) 81–86.

96. M. R. Lilliedal, A. J. Medford, M. V. Madsen, K. Norrman and F. C. Krebs, The effect of post-processing treatments on inflection points in current–voltage curves of roll-to-roll processed polymer photovoltaics, *Sol. Energy Mater. Sol. Cells* **94** (2010) 2018–2031.

97. M. Vogel, S. Doka, C. Breyer, M. C. Lux-Steiner and K. Fostiropoulos, On the function of a bathocuproine buffer layer in organic photovoltaic cells, *Appl. Phys. Lett.* **89** (2006) 163501.

98. C. Waldauf, M. C. Scharber, P. Schilinsky, J. A. Hauch and C. J. Brabec, Physics of organic bulk heterojunction devices for photovoltaic applications, *J. Appl. Phys.* **99** (2006) 104503.

99. F. Padinger, R. S. Rittberger and N. S. Sariciftci, Effects of Postproduction Treatment on Plastic Solar Cells, *Adv. Funct. Mater.* **13** (2003) 85–88.

100. V. D. Mihailetchi, H. X. Xie, B. de Boer, L. J. A. Koster and P. W. M. Blom, Charge Transport and Photocurrent Generation in Poly(3-hexylthiophene): Methanofullerene Bulk-Heterojunction Solar Cells, *Adv. Funct. Mater.* **16** (2006) 699–708.

101. G. Li, V. Shrotriya, J. Huang, Y. Yao, T. Moriarty, K. Emery and Y. Yang, High-efficiency solution processable polymer photovoltaic cells by self-organisation of polymer blends, *Nat. Mater.* **4** (2005) 864–868.

102. G. Li, Y. Yao, H. Yang, V. Shrotriya, G. Yang and Y. Yang, "Solvent Annealing" Effect in Polymer Solar Cells Based on Poly(3-hexylthiophene) and Methanofullerenes, *Adv. Funct. Mater.* **17** (2007) 1636–1644.

103. D. Nassyrov, C. Müller, A. Roigé, I. Burgués-Ceballos, O. Ossó, D. B. Amabilino, M. Garriga, M. I. Alonso, A. R. Goñi and M. Campoy-Quiles, Vapour printing : patterning of the optical and electrical properties of organic semiconductors in one simple step, *J. Mater. Chem.* **22** (2012) 4519–4526.

104. M. Campoy-Quiles, T. Ferenczi, T. Agostinelli, P. G. Etchegoin, Y. Kim, T. D. Anthopoulos, P. N. Stavrinou, D. D. C. Bradley and J. Nelson, Morphology evolution via self-organization and lateral and vertical diffusion in polymer:fullerene solar cell blends., *Nat. Mater.* **7** (2008) 158–164.

105. W. C. Tsoi, S. J. Spencer, L. Yang, A. M. Ballantyne, P. G. Nicholson, A. Turnbull, A. G. Shard, C. E. Murphy, D. D. C. Bradley, J. Nelson and J.-S. Kim, Effect of Crystallisation on the Electronic Energy Levels and Thin Film Morphology of P3HT:PCBM Blends, *Macromolecules* **44** (2011) 2944–2952.

106. D. E. Motaung, G. F. Malgas, C. J. Arendse, S. E. Mavundla, C. J. Oliphant and D. Knoesen, Thermal-induced changes on the properties of spin-coated P3HT: C60 thin films for solar cell applications, *Sol. Energy Mater. Sol. Cells* **93** (2009) 1674–1680.

107. T. Agostinelli, S. Lilliu, J. G. Labram, M. Campoy-Quiles, M. Hampton, E. Pires, J. Rawle, O. Bikondoa, D. D. C. Bradley, T. D. Anthopoulos, J. Nelson and J. E. Macdonald, Real-Time Investigation of Crystallisation and Phase-Segregation Dynamics in P3HT:PCBM Solar Cells During Thermal Annealing, *Adv. Funct. Mater.* **21** (2011) 1701–1708.

108. S. van Bavel, E. Sourty, G. de With, K. Frolic and J. Loos, Relation between Photoactive Layer Thickness, 3D Morphology, and Device Performance in P3HT/PCBM Bulk-Heterojunction Solar Cells, *Macromolecules* **42** (2009) 7396–7403.

109. S. T. Turner, P. Pingel, R. Steyrleuthner, E. J. W. Crossland, S. Ludwigs and D. Neher, Quantitative analysis of bulk heterojunction films using linear absorption spectroscopy and solar cell performance, *Adv. Funct. Mater.* **21** (2011) 4640–4652.

110. M. T. Dang, G. Wantz, H. Bejbouji, M. Urien, O. J. Dautel, L. Vignau and L. Hirsch, Polymeric solar cells based on P3HT:PCBM: Role of the casting solvent, *Sol. Energy Mater. Sol. Cells* **95** (2011) 3408–3418.

111. F. Machui, S. Langner, X. Zhu, S. Abbott and C. J. Brabec, Determination of the P3HT:PCBM solubility parameters via a binary solvent gradient method: Impact of solubility on the photovoltaic performance, *Sol. Energy Mater. Sol. Cells* **100** (2012) 138–146.

112. M. Campoy-Quiles, V. Randon, M. M. Mróz, M. Jarzaguet, M. Garriga and J. Cabanillas-González, Continuous lateral gradients in film morphology for position sensitive detection and organic solar cell optimisation, *Org. Photonics Photovoltaics* **1** (2013) 11–23.

113. J. H. Hildebrand and R. L. Scott, The Entropy of Solution of Nonelectrolytes, *J. Chem. Phys.* **20** (1952) 1520.

114. C. M. Hansen, *Hansen solubility parameters. A user's handbook*, 2nd ed. (2007).

115. S. Abbott, C. M. Hansen and H. Yamamoto, Hansen Solubility Parameters in Practice, (software) Version 3.1.17, Available at: www.hansen-solubility.com.

116. F. Machui, S. Abbott, D. Waller, M. Koppe and C. J. Brabec, Determination of Solubility Parameters for Organic Semiconductor Formulations, *Macromol. Chem. Phys.* **212** (2011) 2159–2165.

117. J. C. Hummelen, B. W. Knight, F. LePeq, F. Wudl, J. Yao and C. L. Wilkins, Preparation and Characterization of Fulleroid and Methanofullerene Derivatives, *J. Org. Chem.* **60** (1995) 532–538.

Bibliography

118. M. M. Wienk, J. M. Kroon, W. J. H. Verhees, J. Knol, J. C. Hummelen, P. A. van Hal and R. A. J. Janssen, Efficient Methano[70]fullerene/MDMO-PPV Bulk Heterojunction Photovoltaic Cells, *Angew. Chemie Int. Ed.* **115** (2003) 3493–3497.

119. A. Mishra and P. Bäuerle, Small molecule organic semiconductors on the move: promises for future solar energy technology., *Angew. Chem. Int. Ed. Engl.* **51** (2012) 2020–67.

120. M. Koppe, C. J. Brabec, S. Heiml, A. Schausberger, W. Duffy, M. Heeney and I. McCulloch, Influence of Molecular Weight Distribution on the Gelation of P3HT and Its Impact on the Photovoltaic Performance, *Macromolecules* **42** (2009) 4661–4666.

121. Y. Lin, Y. Li and X. Zhan, Small molecule semiconductors for high-efficiency organic photovoltaics, *Chem. Soc. Rev.* **41** (2012) 4245.

122. J. Min, Y. N. Luponosov, T. Ameri, A. Elschner, S. M. Peregudova, D. Baran, T. Heumüller, N. Li, F. Machui, S. Ponomarenko and C. J. Brabec, A solution-processable star-shaped molecule for high-performance organic solar cells via alkyl chain engineering and solvent additive, *Org. Electron.* **14** (2013) 219–229.

123. P. Troshin, H. Hoppe, J. Renz, M. Egginger, J. Mayorova, a E. Goryochev, a Peregudov, R. Lyubovskaya, G. Gobsch, N. S. Sariciftci and V. Razumov, Material Solubility-Photovoltaic Performance Relationship in the Design of Novel Fullerene Derivatives for Bulk Heterojunction Solar Cells, *Adv. Funct. Mater.* **19** (2009) 779–788.

124. P. Kubis, N. Li, T. Stubhan, F. Machui, G. J. Matt, M. M. Voigt and C. J. Brabec, Patterning of organic photovoltaic modules by ultrafast laser, *Prog. Photovoltaics Res. Appl.* (2013) DOI: 10.1002/pip.2421.

125. Y.-J. Cheng, S.-H. Yang and C.-S. Hsu, Synthesis of conjugated polymers for organic solar cell applications, *Chem. Rev.* **109** (2009) 5868–923.

126. C.-D. Park, T. A. Fleetham, J. Li and B. D. Vogt, High performance bulk-heterojunction organic solar cells fabricated with non-halogenated solvent processing, *Org. Electron.* **12** (2011) 1465–1470.

127. Y. Liang, Z. Xu, J. Xia, S.-T. Tsai, Y. Wu, G. Li, C. Ray and L. Yu, For the bright future-bulk heterojunction polymer solar cells with power conversion efficiency of 7.4%, *Adv. Mater.* **22** (2010) E135–E138.

128. G. Fang, J. Liu, Y. Fu, B. Meng, B. Zhang, Z. Xie and L. Wang, Improving the nanoscale morphology and processibility for PCDTBT-based polymer solar cells via solvent mixtures, *Org. Electron.* **13** (2012) 2733–2740.

129. Y. W. Soon, H. Cho, J. Low, H. Bronstein, I. McCulloch and J. R. Durrant, Correlating triplet yield, singlet oxygen generation and photochemical stability in polymer/fullerene blend films, *Chem. Commun.* **49** (2013) 1291–1293.

130. B. A. Collins, Z. Li, J. R. Tumbleston, E. Gann, C. R. Mcneill and H. Ade, Absolute Measurement of Domain Composition and Nanoscale Size Distribution Explains Performance in PTB7:PC71BM Solar Cells, *Adv. Energy Mater.* **3** (2013) 65–74.

131. D. Angmo and F. C. Krebs, Flexible ITO-free polymer solar cells, *J. Appl. Polym. Sci.* **129** (2013) 1–14.

132. A. Kumar and C. Zhou, The race to replace tin-doped indium oxide: which material will win?, *ACS Nano* **4** (2010) 11–14.

133. C. J. M. Emmott, A. Urbina and J. Nelson, Environmental and economic assessment of ITO-free electrodes for organic solar cells, *Sol. Energy Mater. Sol. Cells* **97** (2012) 14–21.

134. T. Aernouts, P. Vanlaeke, W. Geens, J. Poortmans, P. Heremans, S. Borghs, R. Mertens, R. Andriessen and L. Leenders, Printable anodes for flexible organic solar cell modules, *Thin Solid Films* **451-452** (2004) 22–25.

135. Y. Xia, K. Sun and J. Ouyang, Solution-processed metallic conducting polymer films as transparent electrode of optoelectronic devices, *Adv. Mater.* **24** (2012) 2436–2440.

136. X. Wang, T. Ishwara, W. Gong, M. Campoy-Quiles, J. Nelson and D. D. C. Bradley, High-Performance Metal-Free Solar Cells Using Stamp Transfer Printed Vapor Phase Polymerized Poly(3,4-Ethylenedioxythiophene) Top Anodes, *Adv. Funct. Mater.* **22** (2012) 1454–1460.

137. W. Gaynor, G. F. Burkhard, M. D. McGehee and P. Peumans, Smooth nanowire/polymer composite transparent electrodes, *Adv. Mater.* **23** (2011) 2905–10.

138. J. Ajuria, I. Ugarte, W. Cambarau, I. Etxebarria, R. Tena-Zaera and R. Pacios, Insights on the working principles of flexible and efficient ITO-free organic solar cells based on solution processed Ag nanowire electrodes, *Sol. Energy Mater. Sol. Cells* **102** (2012) 148–152.

139. J. Meiss, M. K. Riede and K. Leo, Towards efficient tin-doped indium oxide (ITO)-free inverted organic solar cells using metal cathodes, *Appl. Phys. Lett.* **94** (2009) 013303.

140. J. Ajuria, I. Etxebarria, W. Cambarau, U. Muñecas, R. Tena-Zaera, J. C. Jimeno and R. Pacios, Inverted ITO-free organic solar cells based on p and n semiconducting oxides. New designs for integration in tandem cells, top or bottom detecting devices, and photovoltaic windows, *Energy Environ. Sci.* **4** (2011) 453.

141. D. Angmo, M. Hösel and F. C. Krebs, All solution processing of ITO-free organic solar cell modules directly on barrier foil, *Sol. Energy Mater. Sol. Cells* **107** (2012) 329–336.

142. Y. Galagan, J.-E. J.M. Rubingh, R. Andriessen, C.-C. Fan, P. W.M. Blom, S. C. Veenstra and J. M. Kroon, ITO-free flexible organic solar cells with printed current collecting grids, *Sol. Energy Mater. Sol. Cells* **95** (2011) 1339–1343.

143. D. Angmo, S. A. Gevorgyan, T. T. Larsen-Olsen, R. Søndergaard, M. Hösel, M. Jørgensen, R. Gupta, G. U. Kulkarni and F. C. Krebs, Scalability and stability of very thin, roll-to-roll processed, large area, indium-tin-oxide free polymer solar cell modules, *Org. Electron.* **14** (2013) 984–994.

144. A. Du Pasquier, H. E. Unalan, A. Kanwal, S. Miller and M. Chhowalla, Conducting and transparent single-wall carbon nanotube electrodes for polymer-fullerene solar cells, *Appl. Phys. Lett.* **87** (2005) 203511.

145. R. C. Tenent, T. M. Barnes, J. D. Bergeson, A. J. Ferguson, B. To, L. M. Gedvilas, M. J. Heben and J. L. Blackburn, Ultrasmooth, Large-Area, High-Uniformity, Conductive Transparent Single-Walled-Carbon-Nanotube Films for Photovoltaics Produced by Ultrasonic Spraying, *Adv. Mater.* **21** (2009) 3210–3216.

146. M. Choe, B. H. Lee, G. Jo, J. Park, W. Park, S. Lee, W.-K. Hong, M.-J. Seong, Y. H. Kahng and K. Lee, Efficient bulk-heterojunction photovoltaic cells with transparent multi-layer graphene electrodes, *Org. Electron.* **11** (2010) 1864–1869.

147. J. D. Servaites, S. Yeganeh, T. J. Marks and M. A. Ratner, Efficiency Enhancement in Organic Photovoltaic Cells: Consequences of Optimising Series Resistance, *Adv. Funct. Mater.* **20** (2010) 97–104.

148. www.sigmaaldrich.com.

149. F. C. Krebs, N. Espinosa, M. Hösel, R. R. Søndergaard and M. Jørgensen, 25th Anniversary Article: Rise to Power - OPV-Based Solar Parks, *Adv. Mater.* **26** (2014) 29–39.

150. T. T. Larsen-Olsen, R. R. Søndergaard, K. Norrman, M. Jørgensen and F. C. Krebs, All printed transparent electrodes through an electrical switching mechanism: A convincing alternative to indium-tin-oxide, silver and vacuum, *Energy Environ. Sci.* **5** (2012) 9467–9471.

151. J. S. Kang, H. S. Kim, J. Ryu, H. Thomas Hahn, S. Jang and J. W. Joung, Inkjet printed electronics using copper nanoparticle ink, *J. Mater. Sci. Mater. Electron.* **21** (2010) 1213–1220.

152. Novacentrix, www.novacentrix.com.

153. Y. Galagan, E. W. C. Coenen, S. Sabik, H. H. Gorter, M. Barink, S. C. Veenstra, J. M. Kroon, R. Andriessen and P. W. M. Blom, Evaluation of ink-jet printed current collecting grids and busbars for ITO-free organic solar cells, *Sol. Energy Mater. Sol. Cells* **104** (2012) 32–38.

154. M.-G. Kang, M.-S. Kim, J. Kim and L. J. Guo, Organic Solar Cells Using Nanoimprinted Transparent Metal Electrodes, *Adv. Mater.* **20** (2008) 4408–4413.

155. M. Glatthaar, M. Niggemann, B. Zimmermann, P. Lewer, M. Riede, a. Hinsch and J. Luther, Organic solar cells using inverted layer sequence, *Thin Solid Films* **491** (2005) 298–300.

156. T. R. Andersen, H. F. Dam, B. Andreasen, M. Hösel, M. V. Madsen, S. A. Gevorgyan, R. R. Søndergaard, M. Jørgensen and F. C. Krebs, A rational method for developing and testing stable flexible indium- and vacuum-free multilayer tandem polymer solar cells comprising up to twelve roll processed layers, *Sol. Energy Mater. Sol. Cells* **120** (2014) 735–743.

157. A. Cheknane, B. Benyoucef, J.-P. Charles, R. Zerdoum and M. Trari, Minimization of the effect of the collecting grid in a solar cell based silicon, *Sol. Energy Mater. Sol. Cells* **87** (2005) 557–565.

158. K. Tvingstedt and O. Inganäs, Electrode Grids for ITO Free Organic Photovoltaic Devices, *Adv. Mater.* **19** (2007) 2893–2897.

159. M.-G. Kang, M.-S. Kim, J. Kim and L. J. Guo, Organic Solar Cells Using Nanoimprinted Transparent Metal Electrodes, *Adv. Mater.* **20** (2008) 4408–4413.

160. M. Neophytou, E. Georgiou, M. M. Fyrillas and S. A. Choulis, Two step sintering process and metal grid design optimisation for highly efficient ITO free organic photovoltaics, *Sol. Energy Mater. Sol. Cells* **122** (2014) 1–7.

161. J.-S. Yu, I. Kim, J.-S. Kim, J. Jo, T. T. Larsen-Olsen, R. R. Søndergaard, M. Hösel, D. Angmo, M. Jørgensen and F. C. Krebs, Silver front electrode grids for ITO-free all printed polymer solar cells with embedded and raised topographies, prepared by thermal imprint, flexographic and inkjet roll-to-roll processes, *Nanoscale* **4** (2012) 6032–6040.

LIST OF ABBREVIATIONS

AFM	Atomic Force Microscopy
AM 1.5G	Air Mass 1.5 Global
BHJ	Bulk heterojunction
BrAni	4-bromoanisole
CB	Chlorobenzene / Conduction band
CIGS	$CuIn(Ga)Se_2$
CS	Charge separation
CT	Charge transfer
δ	Hildebrand solubility parameter
δ_D	Dispersive forces interactions
δ_P	Permanent dipole-permanent dipole interactions
δ_H	Hydrogen-bonding interactions
DB	Doctor blade
DCB	o-dichlorobenzene
DIO	1,8-diiodooctane
DMSO	Dimethyl sulfoxide
D-π-A	Donor- π-Acceptor
DSSCs	Dye Sensitised Solar Cells
E_g	Energy band gap
EQE	External quantum efficiency
FF	Fill factor
HOMO	Highest occupied molecular orbital
HSP	Hansen solubility parameters
IJP	Inkjet printing
IPCE	Incident photon-to-electron conversion efficiency
I_{ph}	Photocurrent
I_{sc}	Short circuit current
IQE	Internal quantum efficiency
ITO	Indium tin oxide
J_0	Saturation current density
J_{mpp}	Current density at maximum power point
J_{sc}	Short circuit current density
LUMO	Lowest unoccupied molecular orbital
n	Ideality factor

N(Ph-2T-DCN-Et)$_3$	tris{4-[5''-(1,1-dicyanobut-1-en-2-yl)-2,2'-bithiophen-5-yl]phenyl}amine
NIR	Near infra-red
NREL	National renewable energy laboratory
OD	Optical density
OPV	Organic photovoltaics
P3HT	Poly(3-hexylthiophene-2,5-diyl)
PCBM / PC$_{60}$BM	[6,6]-phenyl-C$_{61}$-butyric acid methyl ester
PC$_{70}$BM	[6,6]-phenyl-C$_{71}$-butyric acid methyl ester
PCDTBT	Poly[N-9'-heptadecanyl-2,7-carbazole-alt-5,5-(4',7'-di-2-thienyl-2',1',3'-benzothiadiazole)]
PCE	Power conversion efficiency
PEDOT:PSS	Poly(3,4-ethylenedioxythiophene):poly(styrenesulfonate)
PL	Photoluminescence
PTB7	Thieno[3,4-b]thiophene/benzodithiophene
QE	Quantum efficiency
ρ_M	Metal resistivity
ρ_{sh}	Sheet resistivity
R$_0$	Solubility radius
R2R	Roll-to-roll
R$_a$	Relative solubility distance
RE	Renewable energies
RED	Relative energy difference
RMS	Root mean square
R$_p$	Parallel resistance
R$_s$	Series resistance
SC	Spin coating
THF	Tetrahydrofuran
THN	1,2,3,4-tetrahydronaphthalene
UV	Ultraviolet
UV-Vis	Ultraviolet-visible
VASE	Variable angle spectroscopic ellipsometry
VB	Valence band
V$_{mpp}$	Voltage at maximum power point
V$_{oc}$	Open circuit voltage
W	Free exciton bandwidth

LIST OF FIGURES

Figure 3.1. Schematic representation of the drying process of a wet film (cross section view) with (a-c) one solvent and (d-f) a mixture of a high boiling point, low surface tension solvent and a low boiling point, high surface tension solvent. When the process starts (a) and (d) the liquid evaporates faster at the edges due to the higher surface to volume ratio (green arrows). This provokes an increase of the local concentration of the solution at the edges. To compensate this gradient of concentration the solvent migrates to the edges (blue arrows in b and e), lugging the dissolved material with him. With one solvent this leads to the coffee ring (c). With the described mixture of solvents, the faster

evaporation of liquid at the edges leads also to a gradient of surface tension due to the different evaporation rates of the two solvents. To compensate this new gradient, the low surface tension solvent flows from the edges to the centre of the drop (red arrows in e), resulting in uniform thickness of the dried film (f). 49

LIST OF TABLES

LIST OF PUBLICATIONS

• D. Nassyrov, C. Müller, A. Roigé, <u>I. Burgués-Ceballos</u>, O. Ossó, D. Amabilino, M. Garriga, I. Alonso, A. Goñi and M. Campoy-Quiles, Vapour printing: Patterning of the optical and electrical properties of organic semiconductors in one simple step. *J. Mater. Chem.*, **22** (2012) 4519-4526.

• <u>I. Burgués-Ceballos</u>, M. Campoy-Quiles, L. Francesch and P. D. Lacharmoise, Fast annealing and patterning of polymer solar cells by means of vapor printing, *J. Polym. Sci., Part B: Polym. Phys.*, **50** (2012) 1245–1252.

• <u>I. Burgués-Ceballos</u>, F. Machui, J. Min, T. Ameri, M. M. Voigt, Y. N. Luponosov, S. A. Ponomarenko, P. D. Lacharmoise, M. Campoy-Quiles and C. J. Brabec, Solubility based identification of green solvents for small molecule organic solar cells, *Adv. Funct. Mater.*, **24** (2014) 1449-1457.

• <u>I. Burgués-Ceballos</u>, N. Kehagias, C. M. Sotomayor-Torres, M. Campoy-Quiles and P. D. Lacharmoise, Embedded inkjet printed silver grids for ITO-free organic solar cells with high fill factor, *Sol. Energy Mater. Sol. Cells*, (2014) DOI:10.1016/j.solmat.2014.03.024.

• <u>I. Burgués-Ceballos</u>, M. Stella, P. D. Lacharmoise and E. Martínez-Ferrero, Towards industrialization of polymer solar cells: materials processing for up-scaling, *in preparation*.

• <u>I. Burgués-Ceballos</u>, M. Stella, P. D. Lacharmoise and M. Campoy-Quiles, Highly efficient polymer solar cells. Really?, *in preparation*.

CONFERENCE CONTRIBUTIONS

• 9th-13th May 2011: **E-MRS Spring Meeting**, Nice (France)
Poster
Title: On the role of solvents in the morphology of inkjet printed organic solar cells

• 15th June 2011: **Japan-Spain Symposium on Nanostructured OPVs**, Bellaterra (Spain)
Presentation
Title: Organic solar cells made by inkjet printing

• 3rd-4th April 2012: **Printed Electronics Europe**, Berlin (Germany)
Poster
Title: Fast annealing and patterning of polymer solar cells by means of vapour printing

• 25th-27th June 2012: **The 8th International Conference on Organic Electronics**, Tarragona (Spain)
Poster
Title: Fast annealing and patterning of polymer solar cells by means of vapour printing

• 2nd-5th June 2013: **Next Generation Organic Photovoltaics**, Groningen, (The Netherlands)
Presentation
Title: Solubility based identification of green solvents for small molecule organic solar cells

This thesis deals with three key issues that organic photovoltaics (OPV) technology has to face in order to achieve a reliable lab-to-fab transfer. First, approaches for large-scale processing and post-processing are needed, ideally with reduced cost. Another aspect that has been poorly attended is related to the solvents used for OPV processing, specifically for active layer deposition. Typically halogenated solvents are employed, being some of them banned for industrial applications. Their replacement by green formulations is therefore a major need. Also, the replacement of indium-tin-oxide electrode is essential to obtain high conductivity at low cost.

In this work a broad investigation in inkjet printing is presented. A new method to determine appropriate printing patterns for active layer deposition has been developed. Moreover, an alternative post-processing treatment called vapour printing is demonstrated for OPV devices. In order to find suitable green solvent systems, a method based on solubility has been extended in this thesis for small molecule based devices. Finally, efficient, ITO-free devices based on metallic grids are demonstrated.